DISSERTATIONES
PHYSICAE
UNIVERSITATIS
TARTUENSIS
120

INDREK SÜNTER

Design and characterisation of subsystems and software for ESTCube-1 nanosatellite

DISSERTATIONES PHYSICAE UNIVERSITATIS TARTUENSIS
120

DISSERTATIONES PHYSICAE UNIVERSITATIS TARTUENSIS
120

INDREK SÜNTER

Design and characterisation of subsystems and software for ESTCube-1 nanosatellite

UNIVERSITY OF TARTU
Press

This study was carried out at Tartu Observatory, the University of Tartu and in the framework of Estonian Student Satellite Programme.

The dissertation was submitted on 5 June 2019 in partial fulfilment of the requirements for the degree of Doctor of Philosophy in physics, and allowed for defence by the Council of the Institute of Physics, University of Tartu.

Supervisor: Prof. Mart Noorma,
University of Tartu,
Estonia

Opponents: Prof. Linas Bukauskas,
Vilnius University,
Lithuania

Rauno Gordon, Ph.D.
Tallinn University of Technology,
Estonia

Defense: 22 August 2019, University of Tartu, Estonia

This work has been partially supported by Graduate School of Functional materials and technologies receiving funding from the European Regional Development Fund in University of Tartu, Estonia.

ISSN 1406-0647
ISBN 978-9949-03-087-3 (print)
ISBN 978-9949-03-088-0 (electronic)

University of Tartu Press
www.tyk.ee

Contents

List of original publications

This thesis is based on the following publications:

[**I**] S. Lätt, A. Slavinskis, E. Ilbis, U. Kvell, K. Voormansik, E. Kulu, M. Pajusalu, H. Kuuste, **I. Sünter** *et al.*, "ESTCube nanosatellite for electric solar wind sail in-orbit technology demonstration," *Proc. Estonian Acad. Sci.*, vol. 63(2S), pp. 200–209, May 2014. [Online]. Available: https://doi.org/10.3176/proc.2014.2S.01

[**II**] K. Laizāns, **I. Sünter**, K. Zālīte, H. Kuuste, M. Valgur, K. Tarbe, V. Allik *et al.*, "The design of fault tolerant command and data handling subsystem for ESTCube-1," *Proc. Estonian Acad. Sci.*, vol. 63(2S), pp. 222–231, May 2014. [Online]. Available: https://doi.org/10.3176/proc.2014.2S.03

[**III**] © 2015 IEEE. Reprinted, with permission, from:
A. Slavinskis, M. Pajusalu, H. Kuuste, E. Ilbis, T. Eenmäe, **I. Sünter**, K. Laizāns *et al.*, "ESTCube-1 in-orbit experience and lessons learned," *IEEE Aerosp. Electron. Syst. Mag.*, vol. 30, no. 8, pp. 12–22, Oct. 2015. [Online]. Available: https://doi.org/10.1109/MAES.2015.150034

[**IV**] © 2016 IEEE. Reprinted, with permission, from:
I. Sünter, A. Slavinskis, U. Kvell, A. Vahter, H. Kuuste, M. Noorma, J. Kütt *et al.*, "Firmware updating systems for nanosatellites," *IEEE Aerosp. Electron. Syst. Mag.*, vol. 31, no. 5, pp. 36–44, May 2016. [Online]. Available: https://doi.org/10.1109/MAES.2016.150162

Other related publications:

1. A. Slavinskis, U. Kvell, E. Kulu, **I. Sünter**, H. Kuuste, S. Lätt, K. Voormansik, and M. Noorma, "High spin rate magnetic controller for nanosatellites," *Acta Astronaut.*, vol. 95, pp. 218–226, Feb. 2014. [Online]. Available: https://doi.org/10.1016/j.actaastro.2013.11.014

2. A. Slavinskis, E. Kulu, J. Viru, R. Valner, H. Ehrpais, T. Uiboupin, M. Järve, E. Soolo, J. Envall, T. Scheffler, **I. Sünter** *et al.*, "Attitude determination and control for centrifugal tether deployment on ESTCube-1 nanosatellite," *Proc. Estonian Acad. Sci.*, vol. 63(2S), pp. 242–249, May 2014. [Online]. Available: https://doi.org/10.3176/proc.2014.2S.05

3. H. Kuuste, T. Eenmäe, V. Allik, A. Agu, R. Vendt, I. Ansko, K. Laizāns, **I. Sünter**, S. Lätt, and M. Noorma, "Imaging system for nanosatellite proximity operations," *Proc. Estonian Acad. Sci.*, vol. 63(2S), pp. 250–257, May 2014. [Online]. Available: https://doi.org/10.3176/proc.2014.2S.06

4. A. Slavinskis, H. Ehrpais, H. Kuuste, **I. Sünter**, J. Viru, E. Kulu, J. Kütt, and M. Noorma, "Flight results of ESTCube-1 attitude determination system," *J. Aerosp. Eng.*, vol. 29, no. 1, p. 04015014:1-7, Apr. 2015. [Online]. Available: https://doi.org/10.1061/(ASCE)AS.1943-5525.0000504

5. H. Ehrpais, **I. Sünter**, E. Ilbis, J. Dalbins, I. Iakubivskyi, E. Kulu, I. Ploom, P. Janhunen, J. Kuusk, J. Šate, R. Trops, and A. Slavinskis, "ESTCube-2 mission and satellite design," in *Proceedings of Small Satellites, Systems & Services Symposium (4S)*. ESA Publications Division, Jun. 2016, pp. 1–7, Mission Analysis, CS03-3-305.

6. **I. Sünter**, H. Kuuste, J. Kütt, E. Ilbis, A. Agu, I. Iakubivskyi, S. Chopra, T. Ani *et al.*, "Dual-camera payload for ESEO," in *Proceedings of Small Satellites, Systems & Services Symposium (4S)*. ESA Publications Division, Jun. 2016, pp. 1–10, Academic Projects, S13-4-145.

7. **I. Sünter**, H. Kuuste, A. Slavinskis, A. Agu, E. Ilbis, G. Olentšenko, I. Iakubivskyi *et al.*, "Design and testing of a dual-camera payload for ESEO," in *Proceedings of International Astronautical Congress*. IAF, Sep. 2016, pp. 1–10, Small Earth Observation Missions, IAC–16–B4.4.3,x31978.

8. I. Iakubivskyi, H. Ehrpais, J. Dalbins, E. Oro, E. Kulu, J. Kütt, P. Janhunen, A. Slavinskis, E. Ilbis, I. Ploom, **I. Sünter** *et al.*, "ESTCube-2 mission analysis: plasma brake experiment for deorbiting," in *Proceedings of International Astronautical Congress*. IAF, Sep. 2016, pp. 1–10, 45th Student Conference, IAC-16,E2,4,4,x33190.

9. H. Ehrpais, J. Kütt, **I. Sünter**, E. Kulu, A. Slavinskis, and M. Noorma, "Nanosatellite spin-up using magnetic actuators: ESTCube-1 flight results," *Acta Astronaut.*, vol. 128, pp. 210–216, Nov. 2016. [Online]. Available: https://doi.org/10.1016/j.actaastro.2016.07.032

10. I. Iakubivskyi, H. Ehrpais, H. Kuuste, **I. Sünter**, E. Ilbis, M.-L. Aru, E. Oro *et al.*, "ESTCube-2 plasma brake payload for effective deorbiting," in *Proc. 7th European Conference on Space Debris*, Apr. 2017, Debris Mitigation: Design Solutions.

11. A. Slavinskis, P. Janhunen, P. Toivanen, K. Muinonen, A. Penttilä, M. Granvik, T. Kohout, M. Gritsevich, M. Pajusalu, **I. Sünter** *et al.*, "Nanospacecraft fleet for multi-asteroid touring with electric solar wind sails," in *2018 IEEE Aerospace Conference*. IEEE, Mar. 2018, pp. 1–20. [Online]. Available: https://doi.org/10.1109/AERO.2018.8396670

12. **I. Sünter**, H. Kuuste, and J. Kütt, "Optical characterisation of the ESEO optical payload," in *Proceedings of the 2nd Symposium on Space Educational Activities*, L. Bacsardi and K. Kovacs, Eds., vol. 2. Budapest University of Technology and Economics, Apr. 2018, pp. 123–126.

13. I. Iakubivskyi, P. Janhunen, J. Praks, V. Allik, K. Bussov, B. Clayhills, J. Dalbins, T. Eenmäe, H. Ehrpais, J. Envall, ... **I. Sünter** *et al.*, "Coulomb Drag Propulsion experiments of ESTCube-2 and FORESAIL-1," in *Tethers in Space Proceedings*, May 2019, submitted.

Author's contribution

The articles on which this thesis is based are the result of collective work and contain important contributions from all co-authors. During the time when all publications of this thesis were prepared, the author was a part of the ESTCube-1 core team as well as leading the command and data handling system and supervising students and trainees.

The author's contribution to the publications referred to by their Roman numerals is listed as follows:

[I] As a member of the ESTCube-1 core team, the author contributed to the development of the mission concept, mission design, definition of scientific objectives and requirements for the satellite platform as well as to the development of electronics and software for the spacecraft. The author defined the mechanical, electrical and software specifications for satellite bus integration as well as performed electrical integration testing of the spacecraft subsystems. The author contributed in the characterisation of magnetometers and the residual magnetic field in the spacecraft. In addition to hardware integration, the author performed the software integration and optimized the timing of attitude determination and control operations. To validate the attitude determination and control algorithms on the on-board computer, the author used Hardware In Loop (HIL) testing. The author helped to set up the hardware and software for remote ground-testing and verification of spacecraft functionality as well as supervised the design, implementation and testing of the spacecraft Internal Communications Protocol (ICP) and ICPTerminal. Based on the more general spacecraft requirements, the author derived requirements, designed, implemented and tested the Universal Asynchronous Receiver-Transmitter (UART), Inter-Integrated Circuit (I^2C), Serial Peripheral Interface (SPI) software drivers, error handling, file system and command scheduler for the on-board computer and camera. Similarly, the author derived requirements, designed, implemented and tested the spacecraft mission logic and software drivers for controlling the payload.

[II] Based on the spacecraft platform requirements, the author derived requirements, designed, assembled and tested the first electronics prototype of the ESTCube-1 Command and Data Handling System (CDHS). The author supervised the design and testing of the follow-up versions of CDHS hardware. In addition to developing the CDHS prototype hardware, the author designed, implemented and tested its software drivers (UART, I^2C, SPI), error handling, file systems and command scheduler.

For the article, the author wrote the software design section as well as harmonised the other sections.

[**III**] The author assisted in the pre-flight validation of attitude determination sensors and in-orbit validation of the on-board computer. The author performed the in-orbit characterisation of the payload high voltage supply and electron emitter as well as assisted the residual magnetic field measurements and in-orbit calibration of magnetometers. ESTCube-1 was operated through ICPTerminal which the author adapted for in-orbit operations. The author performed in-orbit firmware updates on CDHS for testing improved attitude determination and control algorithms. The author contributed to writing of all sections.

[**IV**] The author supervised the definition of requirements, the design, implementation and testing of the bootloader for both the on-board computer and camera. The author derived the requirements, designed, implemented and tested the firmware updating functionality for the on-board computer. The author later generalised the bootloader and software library for firmware updates on future missions. The author contributed by writing the text as well as designing tables and figures.

Acronyms and abbreviations

1U	Single Unit CubeSat
ADC	Analogue to Digital Converter
ADCS	Attitude Determination and Control System
AIV	Assembly, Integration, Verification
AP	Access Port
ARQ	Automatic Repeat-Request
CAD	Computer Aided Design
CAM	Camera
CDHS	Command and Data Handling System
COM	Communication system
COTS	Commercial Off-The-Shelf
CRC	Cyclic Redundancy Check
CW	Continuous Wave
CVCM	Collected Volatile Condensable Material
DLR	Deutsches Zentrum für Luft- und Raumfahrt e.V.
EMI	Electro-Magnetic Interference
EPS	Electrical Power System
FoV	Field of View
FRAM	Ferroelectric Random Access Memory
FSK	Frequency Shift Keying
GS	Ground Station
HAL	Hardware Abstraction Layer
HDLC	High-Level Data Link Control
HIL	Hardware In Loop
I^2C	Inter-Integrated Circuit
ICP	Internal Communications Protocol
IOD	In-Orbit Demonstration
LEO	Low Earth Orbit
MCU	Microcontroller
MEMS	MicroElectroMechanical Systems
NAND	Not-AND
NOR	Not-OR
PCB	Printed Circuit Board
PFM	Proto-Flight Model
PL	Payload
PSYS	Platform System

PWM	Pulse Width Modulation
RAM	Random Access Memory
RBF	Remove Before Flight
RF	Radio Frequency
RTC	Real-Time Clock
Rx	Receive
S/C	Spacecraft
SNR	Signal to Noise Ratio
SPI	Serial Peripheral Interface
SRAM	Static Random Access Memory
SSO	Sun-Synhronous Orbit
TC	Telecommand
TLE	Two-Line Element set
TML	Total Mass Loss
TRL	Technology Readiness Level
Tx	Transmit
UART	Universal Asynchronous Receiver-Transmitter
UDP	User Datagram Protocol
UKF	Unscented Kalman Filter
USB	Universal Serial Bus

Chapter 1
Introduction

1.1 Background

Electric Solar Wind Sail (E-sail) [1] is a novel electric propulsion technology which enables quick rendezvous missions towards potentially hazardous asteroids [2, 3], fast interplanetary rendezvous missions [4], near-Sun missions or missions with non-Keplerian orbits [5]. In the atmospheric plasma, E-sail can be used to deorbit spacecraft [6, 7].

Thus far, spacecraft have generally relied on either chemical, cold gas or electric propulsion for orbital maneuvres. Both chemical and cold gas propulsion require propellant which takes up a significant part of the spacecraft mass. Compared to chemical and cold gas propulsion, electric propulsion generally delivers lower levels of thrust but its main advantage is that it relies less on propellant and more on power [8, 9]. While various chemical, cold gas and electric propulsion technologies are considered mature and reliable for large spacecraft, the corresponding technologies for small satellites are still in their infancy [10, 11].

The E-sail technology is based on Coulomb interaction between positively charged tethers and the protons in solar wind. By utilising the solar wind momentum flux for propulsion, E-sail is propellantless. A high voltage supply and electron emitters are used to maintain the charge of the tethers [12]. The long and thin tethers are kept coplanar and straightened by spacecraft rotation. The tether spin plane can be tilted and the overall thrust level can be controlled by adjusting tether potentials [13]. In order to enable the usage of E-sail on-board large or small spacecraft, the Technological Readiness Level (TRL) must be raised by conducting in-orbit validation of the technology.

Testing E-sail technology in space poses several scientific challenges [13]: deploying a two-filament tether made of 25 and 50 µm wires in microgravity without tangling or damaging the tether, verifying its deployment, keeping the tether at positive potential in the atmospheric plasma, and verifying the E-sail effect. The spacecraft would be spun to about $360\,^\circ\,\mathrm{s}^{-1}$ and the centrifugal force acting on the tether end-mass would aid in keeping the tether straightened during unreeling. The reel would be motorized in order to perform the unreeling in controlled steps. Tether deployment could be verified from a change in spin rate as well as by having a camera on-board [14]. By modulating the tether potential with proper timing, the spin rate of the spacecraft could either be

increased or decreased. The E-sail Coulomb force could thus be measured indirectly from the spacecraft spin rate.

When given ambitious challenges, it is often the best to tackle the challenges in small steps. The ESTCube-1 team proposed the hypothesis that a significant part of the E-sail technology can be tested with a 1U CubeSat ($10 \times 10 \times 11.35\,\mathrm{cm}^3$, 1.3 kg nanosatellite [15]).

Since the introduction of the CubeSat standard [15], the interest in nanosatellite platforms for scientific as well as commercial missions has increased significantly [16–19]. The standardised launcher-payload interface yields great flexibility in launcher selection and enables the bulk deployment of CubeSats which helps to reduce the launch cost of an individual CubeSat [20]. On one hand, thanks to the standardisation of the formfactor and highly limited volume, mass and power, the development and launch cost of a typical CubeSat is maintained below that of a larger spacecraft. On the other hand, due to the typical maximum volume of 6 l, mass of 12 kg and power of 30 W [15, 21], it is more challenging to fit payloads on nanosatellites as compared to larger spacecraft. Regardless of the challenges, several scientific nanosatellites have been launched and several companies have emerged which sell CubeSat platforms and their components or provide services based on nanosatellite constellations and their data [22].

By 2019, 10% of the nano- and microsatellites launched had a scientific mission [19]. Among several others, BRITE, CSSWE, and RAX-2 belong to the scientific nanosatellite category. The BRITE constellation observes the variability of the brightest stars [23, 24]. The CSSWE CubeSat measured energetic particles in the near-Earth environment [25]. RAX-2 studied the formation of plasma irregularities in Earth's ionosphere [26].

About 56% of the nano- and microsatellites launched by 2019 had a commercial mission [19]. Planet (former Planet Labs) provides services on visual and near-infrared images from a constellation of nanosatellites. By the time of writing, Planet had successfully launched about 300 Dove satellites [27, 28]. Spire Global provides global ship tracking and weather monitoring services and has launched about 150 CubeSats by the time of writing [29].

By 2019, about 27% of the nano- and microsatellites had been launched with technology demonstration missions [19]. Among others, BEESAT, TechEdSat-1, CanX-4, CanX-5 and STRAND-1 belong to the category of nanosatellites for technology demonstration. BEESAT tested the performance of miniature reaction wheels for attitude stabilisation [30]. TechEdSat-1 demonstrated a miniature radiation hardened platform for future missions [31]. CanX-4 and CanX-5 demonstrated autonomous formation flight in orbit [32]. In addition

to hosting several other payloads, STRAND-1 demonstrated butane resistojet and pulsed plasma thruster technologies for propulsion [33].

At the time of its planning, ESTCube-1 had one of the most complicated scientific missions for a CubeSat. The following technical challenges had to be resolved: miniature tether spool which withstands launch vibrations, non-magnetic reel motor with low power consumption, miniature bipolar high voltage supply for 500 V, electron emitters with low power consumption [34], attitude control system for controlled spin-up to a high angular rate [35], electrical power system which is able to charge the batteries at high spin rates [36–38], communication system which enables telecommands and telemetry at high spin rates, and a small camera [14] which can detect reflection of sunlight from the small end-mass or from the thin tether **[I]**. Prior to ESTCube-1, most of these challenges had not been tackled yet. ESTCube-1 served as a test platform to validate these technologies for future missions. Launched in 2013 and deactivated in 2015, ESTCube-1 was the first nanosatellite designed to perform in-orbit testing of the E-sail payload in the aforementioned configuration **[I]**.

1.2 Progress in this work

While there are several commercial nanosatellite platforms available, none of them are designed to achieve and withstand the spin rate required for tether deployment. In order to meet the challenges, ESTCube-1 was designed around the E-sail payload. Due to the unprecedented mission and payload requirements, new technologies had to be developed which were not yet available for nanosatellites. All ESTCube-1 subsystems: communication (COM), electrical power system (EPS), Command and Data Handling System (CDHS), attitude determination and control system (ADCS), camera payload (CAM) were developed in-house. While maintaining focus on the systems with significant contribution by the author, this work presents the overall architecture, requirements for the spacecraft, design of CDHS, the electrical and software integration of several other subsystems, as well as the post-launch characterisation of several spacecraft systems.

This thesis presents the original contribution of the author to the overall architecture of ESTCube-1, requirements for the spacecraft, design of CDHS, the electrical and software integration of several other subsystems, as well as the post-launch characterisation of several related spacecraft systems.

Based on the mission objectives in Section 3.2 and architectural constraints in Section 3.4, requirements are presented in Section 4. Section 5 provides an overview of the design of the spacecraft, with focus on the aspects most closely

related to the author's contribution in Section 1.3. The in-orbit performance of ESTCube-1 is summarised in Section 6.

1.3 Author's role in the development

The main partners in ESTCube-1 development were the University of Tartu, Tartu Observatory, Tallinn University of Technology, The Estonian University of Life Sciences, Finnish Meteorological Institute, University of Helsinki, University of Jyväskylä and German Aerospace Center (DLR).

The author has contributed to the selection of the E-sail mission, definition of the mission objectives and requirements, as well as to the design, development and validation of spacecraft subsystems. Based on the objectives and requirements, the author designed, developed and tested the first prototype of the CDHS hardware as well as supervised the development and testing of all the following revisions of CDHS hardware. The author contributed to the development of the avionics testbench of the spacecraft and performed electrical and software integration testing of CDHS, CAM, COM, EPS and mission payload. The author developed software for CDHS and integrated ADCS software on-board CDHS. Several CDHS software components were later used on CAM. Additionally, the author co-supervised the design, development and validation of ICP (Internal Communications Protocol) and contributed to the design, development and validation of ICPTerminal. ICPTerminal was used for communicating with, and for testing the spacecraft subsystems individually, as well as for operating the whole spacecraft in orbit.

Chapter 2
E-sail development roadmap

Novel technologies are usually applied to either medium or large scale missions once there is a track record of several successful technology demonstrations. This process is often referred to as increasing the Technology Readiness Level (TRL) [39]. It is important to avoid immature technologies on medium or large scale space missions, especially in mission-critical applications such as propulsion due to the high risk and high cost of a failure.

A full-scale E-sail technology demonstration mission would take place in interplanetary space and would involve about 20 tethers at 20 kV potential and a tether length of 20 km [13]. Due to the technical complexity of the full-scale E-sail technology demonstration, it is preferred to perform independent testing of several key components, as well as to scale the technology step-by-step. The steps to reach the full-scale technology demonstration are listed as follows [3, 5, 6, 13, 40–42]:

1. Scalable tether production.
2. Demonstration of controlled spin-up of a spacecraft, to produce enough centrifugal force on tether end-mass for tether deployment.
3. Demonstration of reliable tether reeling.
4. Demonstration of a high voltage supply and electron emitters to maintain a positive potential on the tether.
5. Indirect measurement of the E-sail effect by measuring the acceleration or deceleration of spacecraft spin-rate in atmospheric plasma flow, with a periodically charged tether.
6. Indirect measurement of the E-sail effect by measuring the orbital decay of a spacecraft with a charged tether, due to drag in atmospheric plasma flow.
7. Measurement of the E-sail effect with a single tether in real solar wind conditions at an apogee of about $30R_E$ where R_E is the radius of the Earth.
8. Orbital control with a single tether E-sail in real solar wind environment.

9. Interplanetary navigation with a single tether E-sail.

10. Demonstration of reliable deployment of 20 or more tethers with remote units and auxiliary tethers to avoid tether collisions.

11. Interplanetary navigation with a system which consists of 20 or more tethers, remote units and auxiliary tethers. Illustration of such a system is provided in Figure 1.

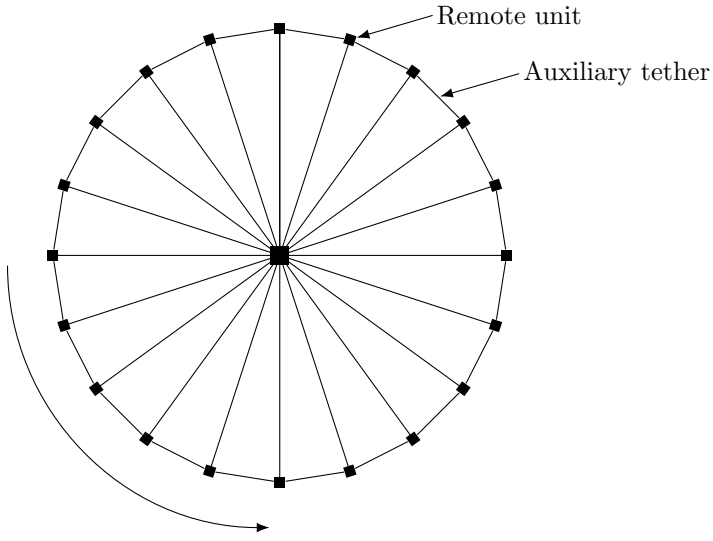

Figure 1: Illustration of a full-scale 20 tether E-sail with centrifugally stabilising auxiliary tethers and remote units with auxiliary tether reels and propulsion for spinup and spin control. Adapted from the original version with untensioned auxiliary tethers [13].

Most of the steps listed above cannot be verified in labs on the ground due to the complexity of mimicking the relevant environment.

Although the deployment of tethers has been demonstrated by prior missions [43–46], the missions have flown with different tether structure and materials which are not suitable for the E-sail mission. For the E-sail mission, Hoytether [47] and Heytether [13, 40–42] have been considered. While high voltage supplies and electron emitters have been flown before [48], keeping a thin tether at a high potential in respect to the surrounding atmospheric plasma is yet to be achieved.

The goal of ESTCube-1 was to demonstrate controlled spin-up of the satellite, tether reel-out in space, tether charging as well as to validate the

plasma physics aspect of the E-sail concept by measuring the electrostatic force acting on a charged tether as it moves through the ionospheric plasma in a Low Earth Orbit (LEO) [13][**I**]. A more detailed list of ESTCube-1 mission objectives are presented in Section 3.2.

Chapter 3
Mission objectives, architecture and timeline

3.1 Development phases

According to the ECSS-M-ST-10C [49] standard, spacecraft development timeline is split into phases, each of which ends with a review. The phases are listed in Table 1, along with their corresponding dates for the ESTCube-1 example. Phase 0 ends with a specification of mission objectives and preliminary technical requirements for the spacecraft. By the end of Phase A, the model philosophy and verification approach have been defined, a detailed risk analysis has been performed and technical solutions have been proposed to meet the mission objectives and requirements. The specification of external interfaces as well as prototyping of critical technologies belongs to Phase B. Phase C involves the detailed definition of internal and external interfaces as well as the production and pre-qualification of spacecraft components. The manufacturing, assembly and testing of flight hardware, software and associated ground support equipment are performed in Phase D. In the case of ESTCube-1, Phase C and Phase D were merged. Phase E is reserved for the on-orbit verification of spacecraft components and spacecraft operations to achieve the mission objectives. In Phase F, the mission is wrapped up and spacecraft is disposed of.

Table 1: ESTCube-1 mission development timeline.

Phase	**Activity**	**Time**
0	Mission analysis	02.09.08 – 17.04.09
A	Feasibility study	17.04.09 – 13.04.10
B	Preliminary definition	13.04.10 – 31.08.10
C	Detailed definition	31.08.10 – ...
D	Qualification and production	... – 01.03.13
E	Operations, utilisation	07.05.13 – 17.02.15
F	Disposal	17.02.15

3.2 ESTCube-1 mission objectives

The results of ESTCube-1 Phase A feasibility study [50] indicated that the first indirect measurement of the E-sail effect in LEO could be performed with

a 1U CubeSat. Based on the E-sail development roadmap in Section 2 and ESTCube-1 Phase A feasibility study [50], the following mission objectives were derived for ESTCube-1:

1. Deploy 10 m of aluminium tether with a wire thickness of 25 µm . . . 50 µm [34].
   - Spin the spacecraft to at least $360\,^\circ\,\mathrm{s}^{-1}$ which would provide enough centrifugal force to deploy a 0.1 g tether with a 1.2 g End Mass **[I]**.
   - Maintain a spin axis tangential to the magnetic field lines of the Earth (illustrated in Figure 3).
   - Perform controlled tether deployment step by step, verifying each step.
   - Verify tether deployment by taking camera images of the tether End Mass.
   - Verify deployment from a change in spin rate which is caused by the change in moment of inertia.
2. Measure the Coulomb force that the atmospheric plasma exerts on the charged tether.
   - While the spacecraft is within ±15° of the geographical poles of the Earth, perform periodical charging of the tether either to a potential of +500 V or −500 V in respect to spacecraft frame [34].
   - Measure tether voltage and tether current.
   - Measure the performance and lifetime of the cold cathode electron emitters in the +500 V mode [34].
   - Measure the cumulative change in satellite spin rate. In one polar pass, angular rate is expected to change by approximately $0.5\,^\circ\,\mathrm{s}^{-1}$ **[I]**.

From the point of view of the E-sail roadmap, it was critical to at least measure the in-orbit performance of the ESTCube-1 ADCS spin-up algorithm which enabled simple and robust tether deployment. Spin-up to angular rates as high as $360\,^\circ\,\mathrm{s}^{-1}$ is challenging because of the high risk of losing control over the spacecraft either because of the limited reaction time of the attitude controller, the loss of ground-communications or the inability to collect power from the solar cells. Due to the mass, volume and power constraints of the 1U CubeSat form-factor, the on-board computational performance is low, the selection of attitude determination sensors is limited, and the selection of actuators for attitude control is limited to just magnetic torquers [50]. Historically, angular

rates of $120\,^\circ\,\mathrm{s}^{-1} \ldots 540\,^\circ\,\mathrm{s}^{-1}$ have been utilised for spin stabilisation [11]. Prior to ESTCube-1, there were also published results on the utilisation of magnetic torquers for spin stabilisation [51] but as far as the author is aware, magnetic torquers have not been used to obtain spin rates above $60\,^\circ\,\mathrm{s}^{-1}$ [52].

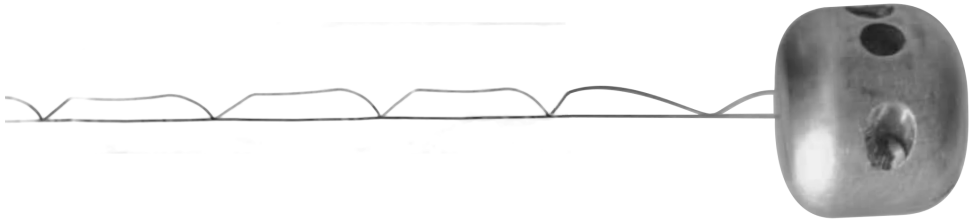

Figure 2: Composite image of the double strand aluminium Heytether [13] and End Mass [34] to illustrate the setup used on ESTCube-1.

In order to produce enough pull at the start of tether deployment, a 1.2 g aluminium End Mass is attached at the end of the tether [**I**]. The setup of a double strand Heytether with an End Mass is illustrated in Figure 2. The End Mass has a reflective surface to enable verification of deployment with a camera [53]. Tether deployment is to be performed in steps, which makes it possible for the spacecraft operators to monitor the spacecraft attitude, adjust the spin axis or increase the spin rate, if needed. Due to the conservation of angular momentum, the full tether deployment causes the spacecraft spin rate to reduce from the initial $360\,^\circ\,\mathrm{s}^{-1}$ to about $20\,^\circ\,\mathrm{s}^{-1}$ [**I**]. Since ADCS must already estimate the angular rate of the spacecraft for detumbling and spin-up, the result can be used to verify tether deployment.

Due to its orbital motion, the spacecraft moves through the orbital plasma with its tether rotating downstream or upstream. By charging the tether as it rotates downstream, the spin rate can be increased. By charging the tether as it rotates upstream, the spin rate can be decreased [**I**]. This is illustrated in Figure 3. The E-sail Coulomb force could then be inferred from measurements of spacecraft spin rate.

The mission can be performed either on near-equatorial or a near-polar orbit. A near-equatorial orbit would be preferable for the E-sail experiment because the magnetic field vector is more homogenous. However, equatorial launches are less common and would make it difficult to utilise ground stations at high latitudes for ground communications.

In a near-polar orbit, the experiment can be performed in only a fraction of the orbit when the orbital plasma stream and spin plane are nearly coplanar. However, in the case of a near-equatorial orbit it would not be possible to spin

the spacecraft around the magnetic field vector using just magnetic torquers and it would not be possible to utilise ground stations located in Estonia for communicating with the spacecraft [50].

For spin-up with magnetic torquers, a near-polar orbit would be preferred due to the directional variation of the magnetic field which enables a spin plane parallel to the equatorial plane (the desired spin plane alignment is illustrated in Figure 3) [13]. The E-sail experiment would be conducted under conditions where the magnetic field is perpendicular to the spin plane and the plasma flow caused by orbital motion is in the spin plane [13]. Under these conditions the Lorentz and Coulomb forces acting on the tether would be coplanar with the spin plane and the forces would not tilt the spin plane. Assuming a near-polar orbit, the E-sail experiment would be conducted at $\pm 15^{\circ}$ from the geographical poles where the spin axis is tangential to the magnetic field [50].

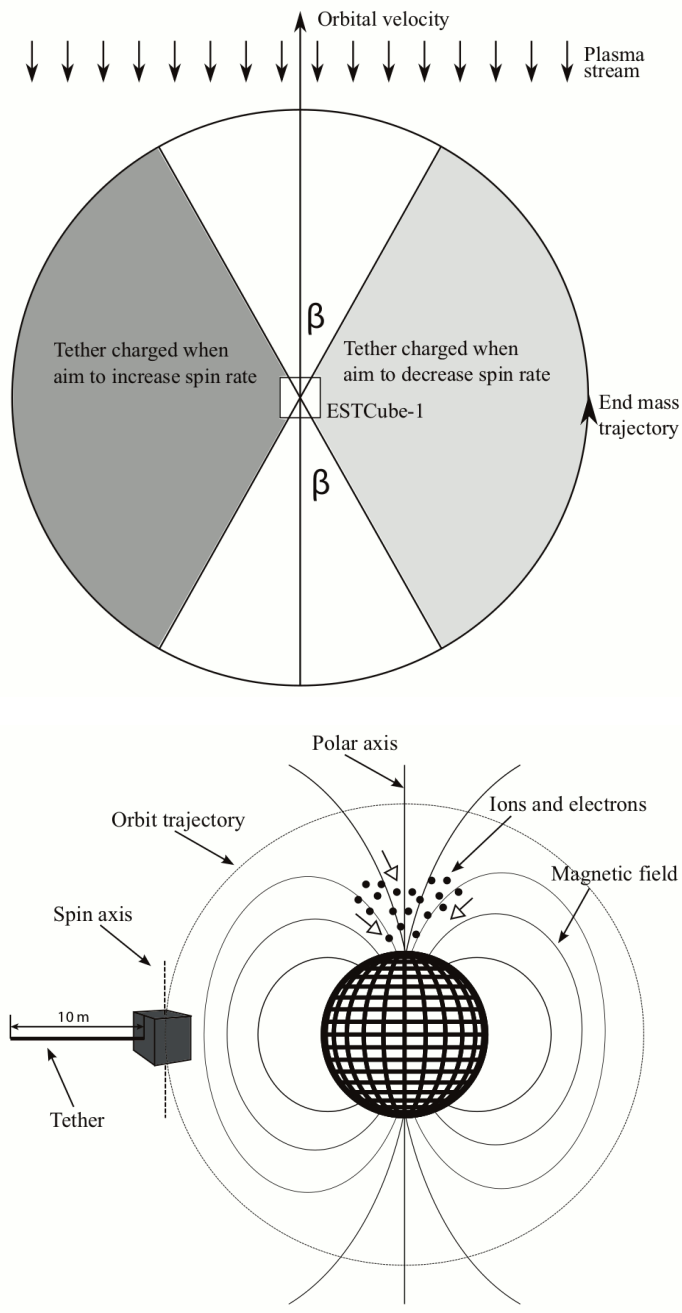

Figure 3: The mission objective to charge the tether synchronously with the rotation of the spacecraft is illustrated at the top. In this case, $\beta = 15°$. The mission objective on spin axis alignment is illustrated at the bottom. [13] **[I]**

It was planned to validate the spacecraft platform for potential utilisation on future missions. The performance and degradation of spacecraft systems developed in-house were to be monitored. The following systems were developed in-house: EPS, COM, ADCS, CDHS, CAM, payload high voltage supply and reel controller.

In parallel to the spacecraft development, a Ground Station (GS) dedicated for spacecraft operations was to be developed and maintained. It was planned to use radio amateur frequencies for communication with the spacecraft: 437.250 MHz for the beacon, 437.505 MHz for telemetry downlink and 145 MHz for telecommand uplink **[I]**. Mission Control System (MCS) software was to be developed in partnership with CGI Estonia for operating the spacecraft in-orbit. Throughout the MCS development [54–56], emphasis was put on educational aspects and the involvement of students from the Institute of Computer Science [57].

Regarding public outreach, with ESTCube-1 being the first Estonian project to develop a spacecraft, the successful deployment and establishment of radio contact was the most critical whereas other mission objectives could be considered a bonus. Since ESTCube-1 already has an objective to take images of the tether End Mass to verify tether deployment, it could also be used to take images of Estonia from space for science popularisation and promotional purposes.

3.3 Time constraints

Spacecraft design is usually defined by one of the following most limiting elements, called design drivers: mission payload, launch window, launcher payload capacity, experiment timeline, etc. With a limited budget and the launch window defined by other spacecraft, the main design driver for ESTCube-1 was its development timeline. The timeline was dependent on the launch date, which, in 2012, was shifted to about half a year earlier than initially planned. Initially it was planned to launch ESTCube-1 on the Polar Satellite Launch Vehicle (PSLV) at the end of 2013. Instead, ESTCube-1 was launched with the second Vega test launch on May 7th, 2013. The testplan was adapted to meet the new time schedule and the team focused on the most critical tasks in order to have a functional spacecraft in orbit. This had a significant impact on the capability to carry out scientific experimentation as well as to gather relevant telemetry from the E-sail payload. The timeline also impacted the capability to collect telemetry characteristic to the degradation of spacecraft subsystems throughout the mission lifetime.

Additionally, the in-orbit operation of the spacecraft was constrained by the limited number of passes over our ground stations, not more than 8 passes per day with pass contact times between 4 min and 13 min. Due to the limited volume, mass and power budgets of the spacecraft, data transfer between the spacecraft and ground station was constrained by 1200 bps uplink and 9600 bps downlink speeds [**I**]. The in-orbit performance and optimizations in bandwidth utilisation are described in Section 6.

3.4 System architecture

In order to provide context and terminology for the requirements in Section 4, this section briefly describes ESTCube-1 system architecture.

The development of ESTCube-1 was split into ground and space segments, each of which were further divided into subsystems. The ground segment is involved with the development and maintenance of GS for satellite communications and MCS which provides an interface for the operators to control the spacecraft. The space segment is involved with space environment analysis as well as the development and testing of the spacecraft. ESTCube-1 subsystems and their corresponding segments are shown in Figure 4.

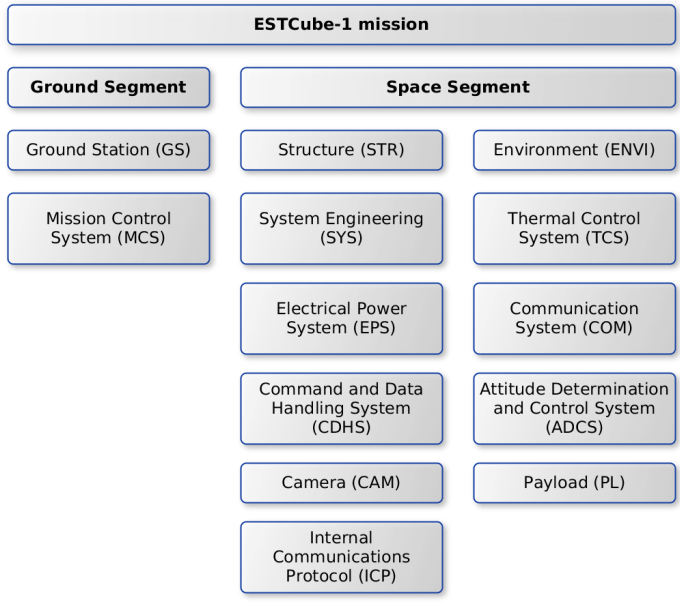

Figure 4: ESTCube-1 system architecture, based on ESTCube-1 Phase A report [50].

MCS notifies a spacecraft operator of the upcoming radio contact when the spacecraft is about to rise over the horizon. During radio contact, GS antennae track the spacecraft and the operator uses MCS to enter telecommands which are converted into packets and passed to the GS for radio transmission. Any telemetry received over the radio by the GS is forwarded to MCS for interpretation and storage.

Each typical spacecraft consists of a platform, also referred to as spacecraft bus, and at least one payload (PL). The spacecraft architecture may vary from mission to mission and depending on the mission any of the platform systems can be experimental and considered a payload. On ESTCube-1, only the E-sail module with its tether reel, reel motor and its controller, electron emitters, and high voltage supply were labelled as payload. A spacecraft platform typically contains a mechanical structure (STR) an electrical power system (EPS), a communication system (COM), a command and data handling system (CDHS) or on-board computer, and an attitude determination and control system (ADCS). All platform systems use a common protocol to communicate, which for ESTCube-1 is called internal communication protocol (ICP). A simplified communication topology diagram of ground and space segment subsystems of ESTCube-1 are shown in Figure 5.

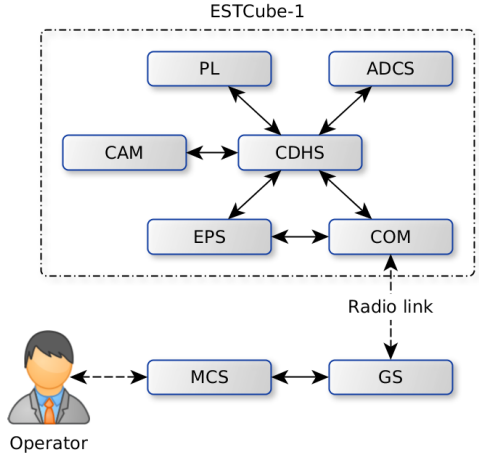

Figure 5: ESTCube-1 system architecture diagram with interfaces.

The design of a spacecraft structure involves computer aided design (CAD), structural analysis and manufacturing of spacecraft frame, side panels, deployables or any other mechanics. Spacecraft mechanical interface must conform to the specifications of the launch and deployment service providers, and usually

involves testing against prescribed vibration and shock profiles. EPS collects power from solar cells, charges its batteries, distributes power to other spacecraft systems and performs the related diagnostics. COM receives radio packets from ground stations, extracts their contents, forwards them to the on-board computer and / or other on-board systems, and finally receives responses which it relays back to the ground stations. The on-board computer (OBC) or CDHS of a spacecraft receives telecommands, schedules commands for execution at a specific time in the future, handles commands and distributes them to payloads and other platform systems. Unless a dedicated platform system is reserved for telemetry collection and storage, it is the job of CDHS. The task of an ADCS in Low Earth Orbit (LEO) is to determine the orientation of the spacecraft in respect to the Earth or Sun and perform the necessary corrections.

Chapter 4
Spacecraft requirements

Based on the mission objectives in Section 3.2, the requirements in Appendix A have been deducted for the spacecraft. Dedicated subsections are only provided for systems closely related to author's contribution.

Since the tether deployment is to be performed with the help of a centrifugal force acting on the tether end-mass, ADCS must be able to spin the spacecraft up to the desired angular rate around the desired axis. EPS must be able to charge the batteries and COM must be able to maintain radio communication with GS while the spacecraft is spinning. Both CAM and ADCS must be able to verify tether deployment. Due to the limited coverage of the ground stations which can be used for ESTCube-1 operations, CDHS must be able to control the payload high voltage supply and electron emitters autonomously. In order to acquire images of Estonia, ADCS should be able to point CAM towards Estonia and CDHS should be able to trigger CAM imaging while passing over Estonia. The spacecraft platform must be miniaturized to fit the E-sail payload, at the cost of modularity and utilisation of standard interfaces. In order to perform an E-sail test mission with a 1U CubeSat, all its systems must be optimized for low mass, volume and low current consumption.

4.1 Mission

The spacecraft must have a near-polar orbit in order to enable the E-sail experiment without compromising contact with the ground stations in Estonia.

More specifically, a Sun-Synhronous Orbit (SSO) is preferred for maintaining the thermal balance of the spacecraft as well as for taking images in the same lighting conditions. On the SSO the spacecraft is in sunlight for at least a part of the pass over the ground stations in Estonia, providing additional power for the experiment and spacecraft communications with degraded batteries at the end of the mission. The SSO also allows spacecraft operators to work during the day.

The orbital altitude of ESTCube-1 must enable a mission lifetime of at least 1 year and should remain below the inner Van Allen belt at 1000 km in order to reduce the amount of shielding which is needed against radiation. Most of the SSO missions are launched at altitudes 600 km . . . 800 km, which would also be suitable for ESTCube-1.

4.2 Structure

Most of the requirements for the structure are defined by the CubeSat design specification [15] and launch vehicle user manual [58]. The CubeSat design specification lists the constraints on material selection, spacecraft mass, its shape and dimensions, and the mechanical interface which is in contact with the spacecraft deployer on the launch vehicle. The spacecraft deployment service provider [59] may override or elaborate on the constraints set by the CubeSat design specification. Launch vehicle user manual defines the depressurisation curve and vibration, shock profiles which the spacecraft must withstand.

Additionally, the CubeSat design specification defines the maximum Total Mass Loss (TML) and Collected Volatile Condensable Material (CVCM) of the materials used. The CubeSat design specification recommends the area of venting holes per ventable volume to reduce the amount of trapped gas during the launch. Launch provider details the thermal vacuum bakeout procedure to ensure proper outgassing of components before integration onto the launch vehicle.

Specifically for ESTCube-1, the requirement for spin axis alignment also posed a constraint on ferromagnetic materials in the spacecraft. The structural requirements are listed in Appendix A.1.

While not listed in the appendix, spacecraft structure is further defined by requirements from environmental analysis [60, 61] to protect the spacecraft against corrosion and radiation, requirements from thermal analysis [62, 63] to provide thermal insulation and heat transfer paths, and requirements from the spacecraft systems and payloads. The structural design of the spacecraft sets further requirements on the hardware design of other subsystems.

4.3 Electrical power system

EPS inherits requirements from the CubeSat specification [15] as well as from the requirements of all other on-board systems. The CubeSat specification defines the maximum battery capacity and by spacecraft form-factor, limits the surface area available for solar cells. In order to keep the satellite mechanical design as robust as possible, it was decided not to use deployable solar panels. However, this limited satellite power production at the beginning of life to 2.4 W . . . 3.4 W [36].

To ensure that the deployment timer does not start while the spacecraft is being integrated into the ISIPOD [59], RBF pins are to be used. Even if the deployment timer would start by accident, it must be possible to reset the timer by depressing the deployment switches again. While a single deployment switch

is enough to fulfil the requirements, at least two deployment switches should be implemented to reduce the likelihood of a faulty switch causing the activation of the spacecraft while still in the dispenser. As the first system to be powered on after the release of the deployment switches, EPS guarantees that all other spacecraft systems remain powered off until the spacecraft has separated from the dispenser. Antenna deployment is allowed only after 30 min since the release of the deployment switches. This helps to ensure that the deployed spacecrafts have been separated enough to avoid collisions and tangling of deployables.

To reduce the risk of RF transmission before the successful deployment of antennas, the antenna deployment sequence should be initiated at least 10 times. During each deployment attempt, the burner wire should be powered for 15 s, and then cooled for 15 s before the next attempt [64]. EPS is the first spacecraft system to be powered, and should maintain a real-time clock (RTC) supplied from the batteries. It must be possible to synchronise the RTC with telecommands [64].

To reduce current through voltage regulators, the drivers for magnetic torquers should be supplied from the main power bus and implemented on EPS [65]. The latency and duty cycle accuracy are defined by the ADCS control algorithm frequency and characteristics of the communication interface between EPS and CDHS.

The EPS requirements are listed in Appendix A.2. EPS design sets further requirements on the electronics design of other subsystems.

4.4 Attitude determination and control

ESTCube-1 ADCS requirements are driven by the mission objectives. In order to deploy the tether, the spacecraft needs controlled spin-up to at least $360\,^\circ\,\mathrm{s}^{-1}$ with its spin axis aligned to Earth's polar axis. For the spin axis alignment with an accuracy of 3°, attitude determination must be functional and have an error of less than 2° at high spin rates [66].

The system should have at least a sun sensor per spacecraft side in addition to magnetometers and gyroscopic sensors in order to satisfy the requirement for attitude determination error. Measurements from multiple magnetometers and gyroscopic sensors should be combined to improve the Signal to Noise Ratio (SNR) of the measurements and to recover in the case that one of the sensors is compromised.

Both spin-up and pointing must be achieved with just magnetic torquers, as the spacecraft lacks available power and free volume for any other actuators.

The actuation period of magnetic torquers should be maximised while accounting for the frequency of the attitude control algorithms and the duration of magnetometer measurements. Enough delay should be reserved between the actuation of magnetic torquers and magnetometer measurements to avoid the saturation of magnetometers.

In order to reliably take photos of Estonia (one of the secondary mission objectives), the spacecraft must have a pointing accuracy of at least 10°. Both pointing and magnetic field model require on-board orbit propagation with a perturbations model, which in turn relies on updated two-line element set (TLE) and absolute time from CDHS.

The ADCS requirements are listed in Appendix A.3. The ADCS design sets further requirements on the electronics and software design of other subsystems.

4.5 Command and data handling

CDHS inherits most of the requirements from the mission objectives, system architecture and from ADCS and PL. The number of UART peripherals is driven by the point-to-point links to other platform systems. The number of SPI peripherals is driven by the number of Analogue to Digital Converters (ADC) in ADCS and PL. Additionally, SPI is needed for on-board non-volatile Random Access Memory (RAM) and mass storage. The number of I^2C peripherals is driven by the number of magnetometers and gyroscopic sensors and the desired level of redundancy on the ADCS printed circuit board (PCB). Additionally, CDHS needs one digital input and 8 digital output lines for payload control.

CDHS runs the Unscented Kalman Filter (UKF) [67] for attitude determination and needs enough computational power to achieve the desired update frequency of 10 Hz. For the UKF to run at 10 Hz, CDHS must be able to acquire ADCS sun sensor and magnetometer measurements at least at 10 Hz and gyroscopic sensor measurements at least once per second. However, at later phases of development it was found that running UKF at update frequencies as low as 3 Hz [35] or 2.5 Hz [66] are enough for spin-up and E-sail measurements.

CDHS schedules commands, distributes commands to other systems, collects housekeeping data and stores measurements from the payload as well as from the platform systems on request. Command scheduling is used for triggering camera images as well as for spin-synchronous charging of the tether. Due to the ground resolution of CAM, the relative accuracy of command scheduling must be ± 1 s or better in order to acquire images of Earth targets. However, due to the high spin rates involved, the spin-synchronous charging of the tether requires a relative scheduling accuracy of 10 ms or better. Attitude

determination orbital model requires absolute time with an accuracy of $\pm 1\,\mathrm{s}$ or better. CDHS should automatically synchronise its RTC with that of EPS which is battery-backed.

CDHS should provide at least 4 MiB non-volatile storage to either store one full orbit of ADCS measurements at 10 Hz with a data rate of up to $6\,\mathrm{KiB\,s^{-1}}$. To store daily payload measurements at 1 Hz, CDHS should provide at least 1.4 MiB of non-volatile memory with a data rate of up to $20\,\mathrm{B\,s^{-1}}$. Additionally, CDHS should provide mass storage for 10 CAM images which amounts to at least 5 MiB.

In order to reduce the amount of data to be downlinked, CDHS should be able to perform lossless compression on the measurement logs. CDHS provides non-volatile storage for ADCS configuration tables (estimated size 4 KiB).

In order to test tether reel-out as well as to tighten or loosen the tether during assembly, CDHS must support telecommands to reel out or reel back in a specified length of tether. After assembly and verification, CDHS must only support tether reel-out. The length of tether reeled out must be maintained in non-volatile memory.

Both positive and negative E-sail modes must be supported. In the positive high voltage mode, the tether would be charged to a positive high potential and CDHS must be able to individually activate or deactivate each electron emitter. In the negative high voltage mode, the tether would be charged to a negative high potential which requires CDHS to enable and disable the ground switch on telecommand. CDHS must be able to power up the high voltage supply and its measurement circuit via EPS, enable and disable the positive or negative high voltage output at scheduled times or on telecommand.

The procedure for controlling the payload high voltage supply and electron emitters is complex and error-prone. Moreover, in the case that the tether or one of the electron emitters short-circuits, CDHS must quickly follow the procedure to power off the payload. The communication delays and spacecraft operator reaction time would be too long to handle the payload control. Thus, CDHS must be able to control the payload, detect, isolate and autonomously recover from potential errors.

To monitor the degradation of CDHS components, both current consumption and temperature measurements are to be acquired. However, since ADCs also experience degradation which causes incorrect measurements, current and temperature measurements should be acquired from independent ADCs.

The CDHS requirements are listed in Appendix A.4. The CDHS design sets further requirements on the electronics and software design of other subsystems.

4.6 Other systems

Considering the cost and the duration of radio frequency coordination for commercial frequency bands, the spacecraft would have to use the radio amateur frequencies for communications. Additional benefits of the radio amateur frequencies is the international support from radio amateurs in receiving spacecraft telemetry. However, the usage of radio amateur frequencies introduces additional requirements for the mission. The mission must be of interest to the radio amateur community, the telemetry and its format must be open and documented, and with a telecommand it must be possible to permanently switch off the transmitter on the spacecraft. Standard data link layer should be used to allow radio amateurs to use existing equipment to receive the spacecraft. MCS must provide a public web interface to collect telemetry from radio amateurs.

The motor controller developed in-house obtained most of its requirements from the payload reel motor specifications and other spacecraft systems such as EPS and CDHS. During assembly, integration and verification (AIV) the motor controller must support both reel-in and reel-out of the tether on signals from CDHS [68]. After AIV, the motor controller should only support tether reel-out.

The payload high voltage supply developed in-house obtained most of its requirements from the mission objectives and from the specifications of the tether reel and electron emitters. The high voltage supply must be able to measure tether voltage, current and the anode current of the active electron emitter. It must be possible to activate the positive mode of operation with the tether charged to a positive potential and the active electron emitter to negative potential. It must also be possible to activate the negative mode of operation with the tether charged to a negative potential. Operation modes must be controllable by CDHS and voltage and current measurements must be delivered to CDHS on an interface isolated from the high voltage board.

During tether deployment, CAM must be able to image the tether End Mass. This yields further requirements on the focal length and radiometric sensitivity of CAM. CAM must support lossless images which would enable calibration and postprocessing of the images on the ground [53].

The requirements are listed in Appendix A.5. The designs of COM, CAM, PL set further requirements on the design of other subsystems.

Chapter 5
Design

This section describes the spacecraft design, with emphasis on author's contribution as well as design aspects which are necessary to explain the author's work.

In order to fit the mission into a 1U CubeSat while fulfilling all the requirements, the spacecraft platform had to deviate from those available commercially and all spacecraft subsystems had to be developed specifically for the mission.

5.1 Hardware design

Overall, the satellite systems were optimised for low power consumption, low mass, low volume and low cost. Consumer grade Commercial-Off-The-Shelf (COTS) components were used where applicable. However, consumer grade components rarely have guarantees for lifetime and performance in the space environment. In order to mitigate the risks of using consumer grade components in space, basic hardware redundancy and fault tolerance methods were used.

In order to have a more robust spacecraft, the number of deployable elements was minimised. The only deployables on the spacecraft were the transmission and reception antennas, and the tether.

In this section, signals in the spacecraft system bus connector are shown in the typewriter font, for example `CDHS_DAC1`. The system bus connector pinout is shown in Appendix B.

5.1.1 Payload

By the time of the ESTCube-1 proto-flight model (PFM) assembly, the Electronics Research Laboratory at the University of Helsinki had set up a semi-automatic factory and produced a tether of length 19.5 m. The tether consisted of two parts: 3.5 m of two-filament Heytether, illustrated in Figure 2, and 16 m of single-filament tether. The Heytether structure was produced from a 50 µm basewire and a 25 µm loop wire [34].

Two cold cathode electron emitters were developed for ESTCube-1 PFM by the University of Jyväskylä. The emitters had graphite coated nickel cathodes and electroformed nickel mesh anodes, with a cathode-anode distance of 100 µm [34]. The electron emitters could be enabled with an active high signal on either `GUN1` or `GUN3`.

The tether reel, its electrical contact for tether charging, the reeling mechanism and launch lock (PL_LLOCK) were developed by the German Aerospace Center (DLR) in Bremen [34]. In addition to the relevant competence, DLR already had a suitable motor and a reference design for the motor controller. The final reel motor controller and reel lock (PL_RLOCK) were developed at the University of Tartu [68].

The payload motor controller had two digital inputs for direction (PL_RMOTOR0 to reel in, PL_RMOTOR1 to reel out) and one digital output for feedback (PL_MCOUNTER). The motor was controlled with a sawtooth signal. Each sawtooth cycle was indicated by a pulse on the PL_MCOUNTER line [68]. Prior to the motor controller integration into ESTCube-1 flight model, a firmware update was performed to disable PL_RMOTOR0.

The high voltage supply could be switched into positive mode by setting NEG_HV_SUP low and POS_HV_SUP high or into negative mode with inverted states on the two lines. Additionally, the design incorporated a ground switch PL_GNDSW to connect the high voltage output to spacecraft ground in the negative mode.

Payload tether current and anode current measurements were acquired from an ADC on the payload high voltage board, the inputs of which were isolated with voltage to frequency to voltage conversion. The output voltage was measured by an on-board ADC which used signals ADCS_SPI0_* and PL_ADC_CS.

The payload modules were supplied by 3.3 V, 5 V and 12 V supplies which had to be enabled and disabled in a specific order, depending on the desired operation mode. Additionally, the supplies had to be enabled and disabled with specific delays to let the supply voltage stabilise.

5.1.2 System bus connectors

Although complete CubeSat subsystem modules could be procured already at the time of ESTCube-1 development, all of them either assumed that the placement of connectors and electronics fixtures conform to the classic PC/104 [69] or PC/104+ [70] layout. For ESTCube-1, the dimensions of the electronics boards were adjusted as well as mounting holes were shifted in order to fit the payload. While the used system bus connector with 120 pins was compliant to PC/104+, the connector was moved closer to the edge of the PCB in order to maximise usable board area. The mechanical PCB template with dimensions is shown in Figure 6.

While there are several manufacturers for the PC104+ connectors, SAMTEC was preferred because of their prior flight heritage on Pumpkin CubeSat Kit [71]. Moreover, SAMTEC provides all the necessary specifications, mechanical draw-

ings, CAD models and material declaration documents for their products. Combinatorial analysis of the PC104+ connectors revealed that some flight model connectors needed to be cut for assembly. Although SAMTEC offered manufacturing of custom connectors, the lead time would not have been acceptable.

All system bus connectors on the flight model had 4×30 pins with 2 mm pitch and gold contacts with at least 0.38 µm of gold. Each pin allowed a current up to 3.8 A and voltage up to 250 VAC. Connector nominal insertion force was 0.59 N with the guaranteed number of mating cycles over 100. Tail shrouds were not used due to issues with availability. Figure 6 illustrates the system bus connector stackup on the ESTCube-1 flight model.

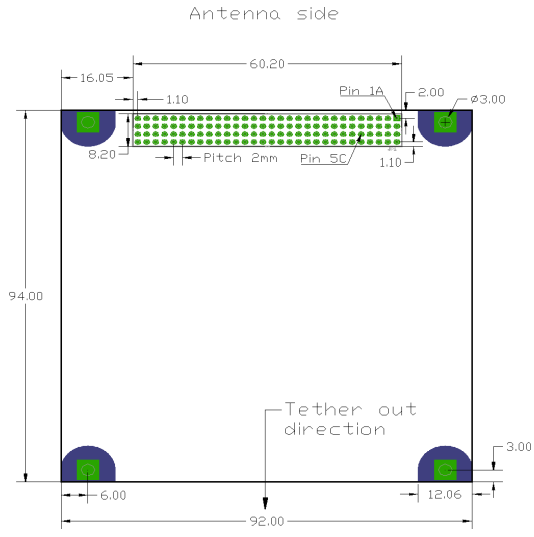

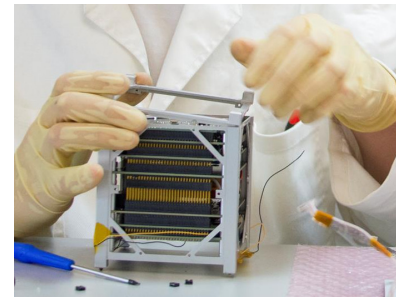

Figure 6: The drawing on the left presents the ESTCube-1 PCB template with antenna deployment system and tether release direction indicated. The photo on the right shows the integration of the ESTCube-1 flight model. System bus connector stackup is visible through the frame.

Due to the large number of pins, the total insertion force of the connectors made it difficult to assemble and disassemble the subsystem stack. The insertion force was large enough to cause a stress within the PCB that might damage vias or components close to the connector. Although not an issue with the assembly of the flight model which was assembled once, the repetitive assembly and disassembly of the spacecraft engineering model caused CDHS flash memory devices to malfunction. Moreover, despite the use of thermals on PCB layouts,

the large number of ground pins on the connector and ground planes on the PCBs made it difficult to solder the connectors.

The electrical pinout of the system bus connector is shown in Appendix B. In the system bus connector pinout, signals were grouped based on signal type to reduce cross-talk. Signal groups were separated by electrical ground connections to reduce electromagnetic interference with neighbouring signal groups as well as to provide electrical ground at low resistance.

The system bus pinout was iteratively reviewed and updated by spacecraft platform and payload teams. To simplify the process, scripts were developed to export the pinout from a Google Drive spreadsheet and generate schematic and PCB layout symbols for the system bus connector in Eagle CAD[1]. The schematic symbol of the connector was split into gates which are called signal groups in the pinout legend in Appendix B. Each subsystem had a dedicated gate to expose its public interface to other subsystems.

5.1.3 Subsystem stack-up

The PCBs of the spacecraft systems were stacked on top of each-other by mating their system bus connectors. Spacers were then added between the PCBs and threaded rods were inserted through the four corners of the stack. The payload was placed in the middle, with EPS and its heavy batteries as close to the middle as possible to have the spacecraft center of mass close enough to its geometric center. COM was located on one side and ADCS with one magnetic torquer on the other side of the stack. Electronics on the side panels were connected with custom-made ribbon cables made of twisted pairs. The overall hardware design of ESTCube-1 is shown in Figure 7.

[1] Autodesk Eagle [72] is an electronic design automation software.

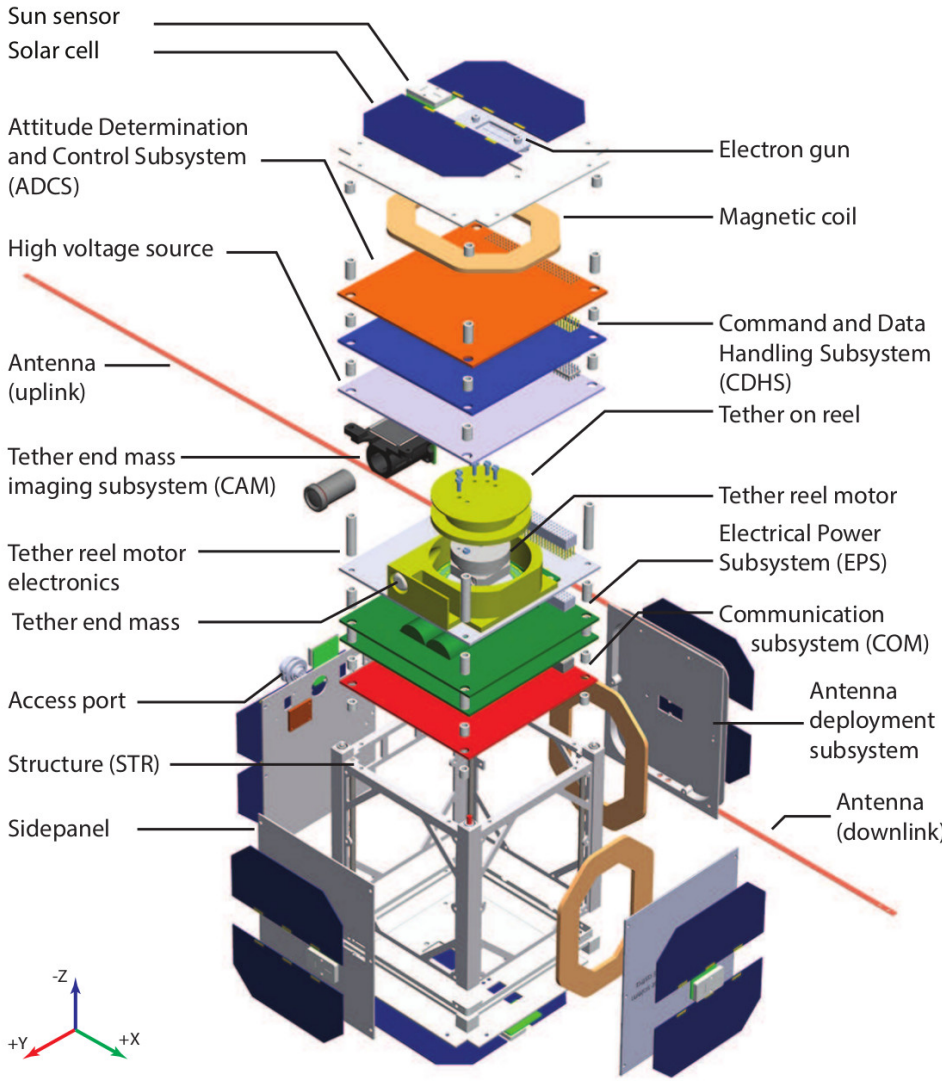

Figure 7: Overall hardware design of ESTCube-1 [**I**].

The spacecraft did not have enough free volume to fit commercial propulsion modules nor reaction wheels. Thus, for detumbling, pointing and spin-up ESTCube-1 relied on three custom magnetorquers, one per axis.

Due to the small dimensions of the spacecraft most of the power switching, voltage regulation and current measurement tasks were delegated to the EPS. This complicated EPS design and increased the number of supply lines in the system bus connector. However, it relieved EPS of coordinating the power supply design for other subsystems.

In order to alleviate the risks of compromised communication interfaces between subsystems, the spacecraft had a mesh of point-to-point communication links with routing. Due to the limited amount of UART peripherals, two on COM and three on EPS, CAM could only be connected to CDHS which had enough peripherals. The topology of the UART connections is shown in Figure 8.

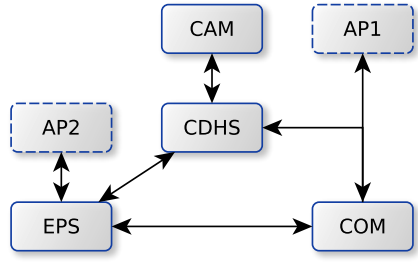

Figure 8: ESTCube-1 subsystem network topology. Arrows represent full duplex UART lines between subsystems. AP1 and AP2 depict the UART connections connected to the spacecraft Access Port (AP).

The third UART connection on EPS was reserved for the spacecraft access port which is marked as AP2 in Figure 8. To facilitate the pre-flight firmware updates of both COM and CDHS with a minimal number of pins reserved on the access port, the UART connection between COM and CDHS was forked to the access port which is marked as AP1 in Figure 8. Even though it was possible to monitor the communication between COM and CDHS when both were powered on simultaneously, either COM or CDHS had to be powered off to transmit packets to the spacecraft through AP1. Through combinations of RBF jumpers, it was possible to force EPS to power either COM, CDHS, or both. Additionally, EPS could be controlled through the second UART on the access port, AP2.

5.1.4 Command and data handling system

The Command and Data Handling System was based on two identical microcontrollers in a cold redundant configuration with memory devices in hot redundant configuration. Cold redundancy of the CDHS microcontroller was implemented using bi-directional high-bandwidth bus switches with 24 channels (SN74CB3Q16211 [73]). The bus switches supported the switching of both digital or analogue signals. Bus switches were grouped by microcontrollers and peripherals, as illustrated in Figure 9.

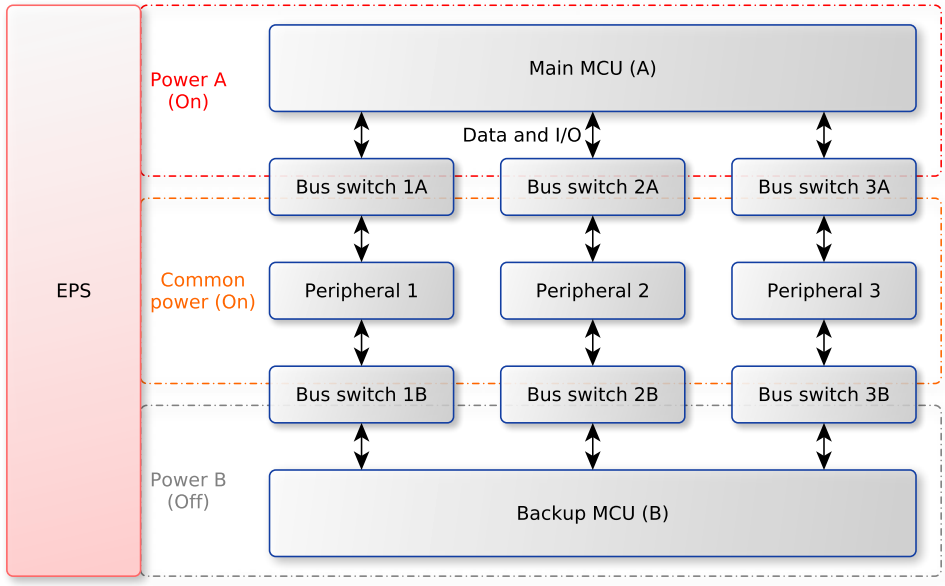

Figure 9: Bus switching scheme used on ESTCube-1 CDHS [**II**].

On telecommand, EPS switched between CDHS microcontrollers. EPS also measured the current consumption of CDHS components and protected it against overcurrent. In order to minimise the time that it took for CDHS to completely power off after being disconnected by EPS, the capacitances on CDHS were minimised. On one hand, by reducing on-board capacitance the likelihood of damage due to single event latch-up was reduced. On the other hand, the low capacitance on CDHS caused rapid fluctuations in load on the EPS regulators for CDHS.

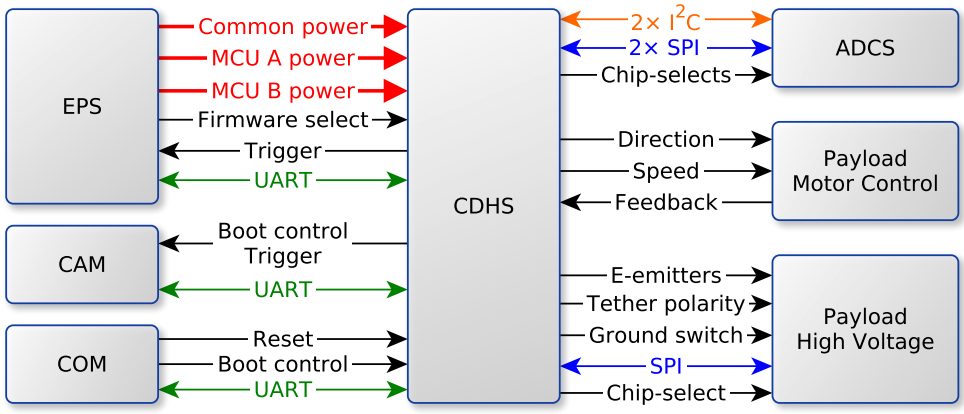

Figure 10: Electrical interfaces between CDHS and other ESTCube-1 systems [**II**]. Different signal types are indicated with different colors.

The interfaces between CDHS and other platform systems are shown in Figure 10. CDHS microcontrollers were powered by individual supply lines from EPS, whereas bus switches and on-board peripherals (except RTC) were powered from a common supply line. In the case that the main microcontroller (MCU) was activated, EPS enabled power on MCU A and CDHS common supplies. In the case that EPS was commanded to switch CDHS to the redundant microcontroller, power to MCU A was removed before enabling power to MCU B.

The "firmware select" (`CDHS_FIRM`) signal between EPS and CDHS allowed EPS to select the active CDHS microcontroller to boot the backup firmware image on reboot or power-cycle. A dedicated digital signal was reserved between EPS and CDHS to facilitate automatic synchronisation of CDHS RTC with that of EPS to sub-second accuracy, as well as to enable low-latency triggering of magnetorquer controllers on EPS.

For communication with EPS, COM and CAM, ICP over UART was used. The UART used for ICP communication to COM also allowed for reprogramming the active CDHS microcontroller through its bootloader in microcontroller ROM. In order for this to work, the CDHS active microcontroller would have been powered on or reset with the boot control pin active. CDHS microcontroller reset and boot control pins were exposed to COM, to enable firmware updates in the case that all the CDHS firmware images on a microcontroller became corrupted. Similarly, CDHS was able to reprogram CAM microcontroller through the UART reserved for ICP communication. A

signal was reserved for scheduled image triggering, which also acted as the CAM microcontroller boot control pin on microcontroller power-on.

In total, 6 digital I/O lines were reserved on the CDHS interface for payload motor control. Four digital outputs on CDHS were reserved for electron emitters on the payload high voltage module. CDHS had one digital output for enabling or disabling the high voltage positive mode and another for the negative mode. Provided that the high voltage supply was in negative mode and the high voltage ground switch `PL_GNDSW` active, the H-bridge connected the negative output of the voltage converter to the tether and the positive output to the satellite body.

Due to the high number of different buses (UART, SPI, I^2C) needed of CDHS, STM32F103VFT6 [74] with 5x USART, 3x SPI and 2x I^2C in the LQFP100 package was selected. While barely providing enough computational power for ADCS algorithms, the microcontroller had a current consumption low enough for the mission. During the CDHS development, STMicroelectronics released the STM32F4 microcontroller series with hardware Floating Point Unit. In order to mitigate the risk of insufficient computational resources for the ADCS algorithms, CDHS electronics was designed to have drop-in support for the STM32F4 series. However, with the complete errata not available yet, the STM32F4 series was not considered mature for the mission. Moreover, the CDHS Hardware Abstraction Layer (HAL) did not yet support the STM32F4 series and would have needed more work.

Peripheral devices were distributed on buses in such a way that CDHS would suffer minimal functionality loss in the case that one of the buses became non-responsive. The distribution of I^2C and SPI buses is illustrated in Figure 11. I^2C1 and I^2C2 were used for ADCS gyroscopic sensors and magnetometers. I^2C1 was also connected to the first Ferroelectric Random Access Memory (FRAM). SPI1 and SPI2 were connected to the sun sensor ADCs on the ADCS PCB. Additionally, SPI1 was connected to the ADC on the payload high voltage PCB as well as to FRAM2, FRAM3 and FRAM4. SPI2 was connected to Flash3, whereas Flash1, Flash2, FRAM5, FRAM6 and RTC were on SPI3.

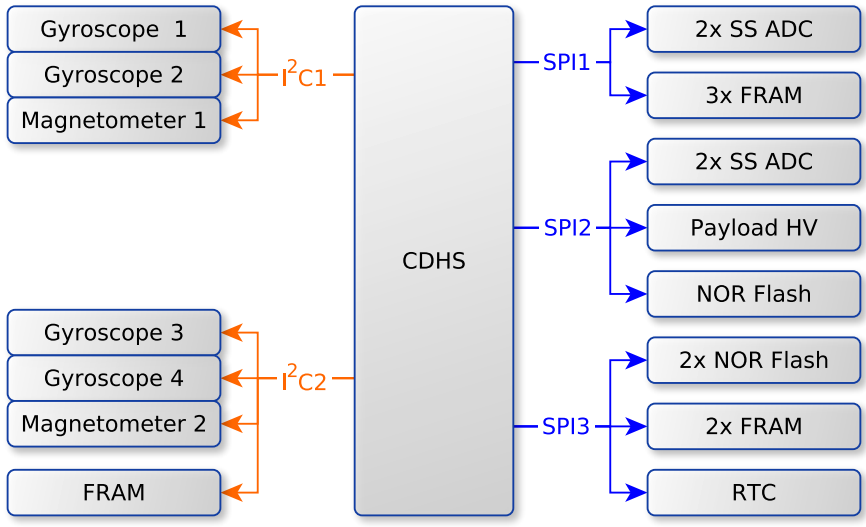

Figure 11: Distribution of I^2C and SPI peripherals on ESTCube-1 CDHS [**II**]. HV in the figure stands for high voltage and SS for sun sensor. Different signal types are indicated with different colors.

If SPI1 had failed, CDHS would have lost access to only half of the FRAM devices. If SPI2 had failed, CDHS would have lost access to one of its mass storage memories whereas the other two would have remained functional. The interfaces to other spacecraft systems were more critical - if either SPI1 or SPI2 were to fail, then half of the sun sensors would have been lost. Also, there was no redundancy on the high voltage payload module. Preliminary testing of the SPI buses confirmed their reliability. Compared to SPI, I^2C buses were found to be significantly less reliable [**III**].

COM was connected to UART1, CAM to UART2 and EPS to UART4. If UART1 had failed, then packets aimed at COM would have been transmitted on UART4 and EPS would have forwarded them to COM. At first COM would have still attempted to respond via CDHS UART1 until a timeout, after which it would have also redirected the response to CDHS through EPS.

Preliminary testing with the CDHS prototype revealed that the UART Tx lines were sensitive to static electricity. In order to improve charge dissipation, 100 kΩ pull-up resistors on all UART Tx lines were introduced in all later revisions of the CDHS electronics. No issues with static electricity were encountered on the more recent STM32F2, STM32F4 or STM32F7 series microcontrollers. In order to avoid generative interference between the CDHS

UART and EPS UART level converter from 5 V to 3.3 V, series resistors were added on the CDHS UART lines.

The low pin count of memory devices with serial interface enables the use of smaller microcontroller packages with lower current consumption. On ESTCube-1, the required storage data rates were low enough to enable the usage of memory devices with serial interface. FRAM devices were used to store files uploaded to CDHS, Flash file system metadata, CDHS error log, payload measurements and on-board scripts.

FRAM is non-volatile, known to be reliable for high number of write cycles with fast access times, has very low current consumption and is more radiation tolerant than typical Flash devices [75, 76]. However, compared to other types of memory, FRAM typically lacks in memory density. One 128 KiB I^2C FRAM [77] and five 256 KiB SPI FRAM [78] devices were incorporated in the CDHS design. FRAM devices in the SOIC16 package were used, which made them easy to solder and easy to attach logic analyser probes to, if necessary.

For mass storage of camera images and ADCS measurements, Not-OR (NOR) Flash memory devices were used. Although NOR Flash memory supports byte-aligned writes, they have lower memory density when compared to Not-AND (NAND) Flash. Both NOR and NAND Flash memory devices typically only support erasing of large blocks or sectors. ESTCube-1 CDHS implemented three S25FL128 [79] devices with SPI interface in order to fulfil the storage space requirements with plenty of margin at the cost of a few pins on the microcontroller. On ESTCube-1 CDHS, flash memory devices in the WSON8 package were used because of their good availability. However, during the assembly and disassembly of the subsystem stack on the spacecraft engineering model, the system bus connector produced mechanical tension in the PCB which caused some Flash memory devices to malfunction. Flash memory devices in other packages might have been more tolerant to mechanical stresses. On ESTCube-1 PFM there were no issues with the Flash memory due to the significantly lower number of mating cycles.

The selection of the ESTCube-1 CDHS RTC (DS3234 [80]) was driven by its accuracy of ±3.5 ppm internal temperature compensation within a wide temperature range −40 °C . . . 85 °C, and an SPI interface. The temperature sensor of the RTC has an accuracy of ±3 °C. For time synchronisation, the CDHS heartbeat pin `CDHS_HBEAT` was used.

Although originally reserved for emergency beacon keying from CDHS, the `CDHS_DAC1` pin was never used. The beacon keying functionality was implemented on EPS [65], which allowed for CDHS to be powered off when unused and helped to reduce spacecraft power consumption.

5.1.5 Camera

ESTCube-1 camera [14, 53] was based on the image sensor MT9V011 from Aptina [81], microcontroller STM32F217ZG [82] from STMicroelectronics and a 2 MB Static Random Access Memory (SRAM) IS61WV102416BLL-10TLI [83]. The microcontroller was similar to the STM32F103ZE [74] used on CDHS [**II**], which simplified the porting of software from CDHS to CAM.

The camera was integrated onto the high voltage supply PCB in the payload module. To minimise the PCB area occupied by the camera, its interface was optimised for minimum number of signals. In addition to the 3.3 V supply and ground, only a UART (`CAM_RX`, `CAM_TX`), an external trigger `CAM_SHOT` and a heartbeat line `CAM_HBEAT` were connected to the system bus connector. Whereas all the signals from CAM were connected to CDHS, none of them were connected to the spacecraft access port in order to save on the access port pin count. The fact that CAM UART was only connected to CDHS allowed for higher baud rates between CAM and CDHS without interfering with other subsystems.

5.2 Software design

The following subsections describe the software design of the spacecraft internal communication protocol, the software used for operating the spacecraft, as well as the software design of active subsystems on-board the spacecraft. As part of the author's contribution, the software design of subsystems is focused on CDHS software, the integration of ADCS algorithms on CDHS, as well as on the software interfaces between CDHS and other subsystems.

5.2.1 Internal communication protocol

Due to the highly limited resources on ESTCube-1, the standard communication protocols such as the CubeSat Space Protocol or Ethernet over serial could not be used for satellite-wide communication between the spacecraft subsystems. A custom communication protocol was developed, which implemented only the necessary subset of features, and was easy to port to the different architectures such as the 8-bit AVR, 16-bit MSP430 and 32-bit STM32 on ESTCube-1.

ESTCube-1 internal communication protocol (ICP) was loosely based on the asynchronous version of the High-Level Data Link Control (HDLC [84]). ICP implemented the Go-Back-N Automatic Repeat-Request (ARQ) data protocol for reliable in-order delivery of packets. ICP maintained a statically defined list of data links to route packets through the mesh of interconnected

subsystems [**II**].

A simulation environment was developed to test ICP in specific scenarios and to verify ICP's ability to recover. The environment started ICP nodes for each subsystem, connected them with User Datagram Protocol (UDP) sockets, and executed subsystem-specific scripts. With the help of the simulation environment, the following scenarios were tested: simple request and response, packet forwarding through another subsystem, packet forwarding through several subsystems, automatic retransmission of missed packets, rerouting due to the failure of a hardware signal line or the loss of a whole UART peripheral.

In order to verify that subsystems conform to the ICP protocol, a command terminal for sending packets and interpreting responses was developed. ICPTerminal was a Python PySide[2] application for testing individual subsystems, an integrated spacecraft or even for operating the spacecraft in-orbit. For mission operations, ICPTerminal acted as a front-end which connected to the Mission Control System endpoints [87].

For testing individual subsystems, the terminal could be configured to act as an ICP node connected via Universal Serial Bus (USB) serial point-to-point links. The terminal could be configured with the ICP node identifier of any subsystem, making it possible to simulate a subsystem in software, or to monitor communication between two subsystems. During the Phases C and D, subsystem-specific extensions were developed for ICPTerminal to exchange files with the spacecraft, convert between file formats and aid in visualizing the data received from the spacecraft. For CDHS, the following extensions were developed: firmware update extension, viewer for error logs, device table manager, configuration table manager, file transfer extension for both raw memory regions and files, a file converter to extract human-readable tables from binary journals, and an extension to manage filters for on-board logging of telecommands.

5.2.2 Ground communications

ESTCube-1 COM had an uplink baud rate of $1200\,\mathrm{bit\,s^{-1}}$, and a downlink baud rate of $9600\,\mathrm{bit\,s^{-1}}$ [**I**]. The main ground stations at Tartu University [88–92] and Tartu Observatory [93, 94] were both half-duplex and the switchover from reception to transmission took at least 50 ms. In order to reduce the overhead of switching between reception and transmission, the protocols for file transfer and firmware updates were designed to support bulk transfer. The downlink speed from the spacecraft, as well as the duration of communication passes

[2]PySide [85] is a Python module providing bindings for Qt [86], a cross-platform application framework.

with the ground stations in Estonia set constraints to the amount of telemetry which could be transmitted by the spacecraft. Except for the Continuous Wave (CW) or telemetry beacon, the spacecraft did not transmit without a request to do so by telecommand.

On ESTCube-1, the production of telemetry was directly controlled by the spacecraft operator. The sampling frequency and time span of ADCS and payload on-board measurements were selected to keep the telemetry file size in the range of 10 KiB . . . 2048 KiB for file downlink to be completed in the reasonable timeframe of up to three weeks. One camera image in raw format, at 640×480 px, 10 bit totalled to 378 KiB, which made it possible to acquire one image every 3 days considering the downlink datarate. Both CAM and CDHS supported multiple responses per request, which reduced the number of packets uplinked at lower baud rate, as well as reduced the switching between reception and transmission at the ground station.

Regardless of the request interval and the amount of data requested, there was a delay between the telemetry packets transmitted by ESTCube-1. While the delay varied from packet to packet, the average delay was 1/4 of the duration of a single 250 B packet. When COM received an ICP packet with the ground station endpoint marked as its destination, COM transmitted it over the radio and then replied to the source subsystem that it was ready to accept another packet. Although CDHS supported telemetry buffering which immediately sent the next packet whenever COM was ready, the notification messages from COM were not sent continuously due to which the telemetry buffering offered little to no improvement in downlink efficiency.

5.2.3 Electrical power system

Prior to launch, ESTCube-1 EPS could be started in different configurations, depending on the combination of the RBF jumpers. For pre-launch servicing, EPS had a dedicated ICP port which could be accessed via access port. With all jumpers removed, EPS started with the access port ICP connection disabled, and proceeded by powering on COM and then CDHS. Other RBF combinations allowed EPS to be started with the access port ICP connection `AP2`, or to skip the power-on of either COM or CDHS.

ESTCube-1 EPS had two in-orbit operation modes: a safe mode where EPS gathered and compiled beacon data, and a normal mode where CDHS collected the telemetry to be transmitted via beacon [64].

As the subsystem which was always powered on, ESTCube-1 EPS maintained the spacecraft time. CDHS could request time synchronisation from the EPS RTC. Upon the reception of the command to synchronise time, EPS

replied with an absolute timestamp in the future, and toggled the CDHS heartbeat pin `CDHS_HBEAT` when the announced time was reached. This helped to avoid non-deterministic latency introduced by ICP.

With direct access to the battery bus, EPS also hosted the drivers for launch- and reel locks and motor controllers for magnetic torquers. Magnetic torqers could be controlled by commanding EPS to configure the magnetic torquers and toggling `CDHS_HBEAT` at the desired time of activation. The command assigned the actuation timeout in milliseconds, and three desired Pulse Width Modulation (PWM) values, one for a magnetic torquer on each axis. To mitigate the risk of magnetic torquers accidentally left active, actuation time was always limited to the range of 0 ms . . . 255 ms [95]. Since CDHS used the `CDHS_HBEAT` pin as input or output depending on whether CDHS was synchronising its time or controlling magnetic torquers, care was taken to avoid racing conditions due to which both CDHS and EPS might have simultaneously treated the pin as an output.

If the spacecraft were to stop transmitting responses to telecommands due to an issue with packet transmission, COM could be power-cycled with a telecommand to EPS. In the case that power-cycling COM did not resolve the issue, a telecommand could be sent to EPS to power-cycle the whole spacecraft by disconnecting batteries until the spacecraft leaves the next eclipse and becomes powered from solar cells again. To reduce the risk of a non-responsive spacecraft due to the failure of telecommand reception, EPS would automatically power-cycle the whole spacecraft if no communication with Earth occurred for 12 hours since the last power-up **[III]**.

5.2.4 Command and data handling system

ESTCube-1 CDHS software had a multi-layered architecture as shown in Figure 12. On top of the standard peripheral library provided by STMicroelectronics, a custom hardware abstraction layer was used to work around any known issues in the standard peripheral library and to provide a common interface to both the STM32F1 and STM32F2 series. For simple multitasking, the miniature open-source real-time operating system FreeRTOS[3] was used. As the first task started on system boot, the system daemon initialised all the drivers, file systems, on-board time management, command scheduler and provided simple error handling and fallback sequences if any of them were to fail [95]. FreeRTOS was configured for 1 ms ticks with microcontroller sleep on idle.

[3]FreeRTOS [96] is a real-time operating system microkernel for embedded systems with limited resources.

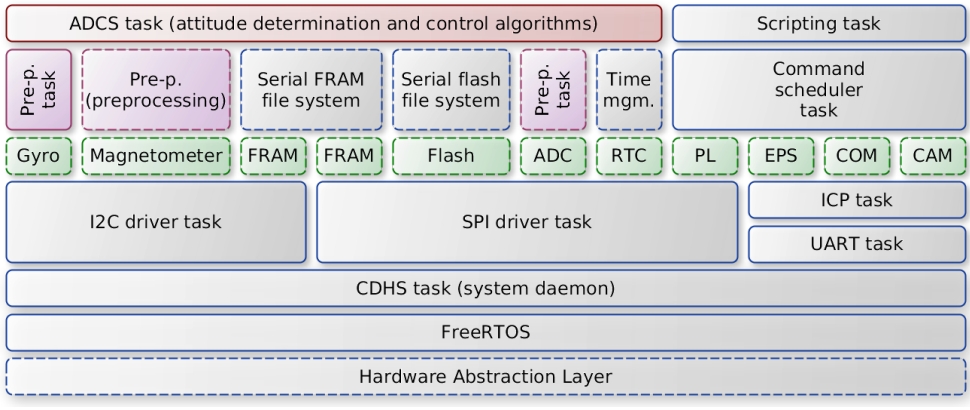

Figure 12: Software layers of ESTCube-1 CDHS, based on the author's master thesis [95]. Modules with their own FreeRTOS tasks are indicated with solid outline, whereas threadless modules are shown with dashed outline. Device drivers are shown in green, ADCS modules in red and the rest of the modules running on CDHS are in blue.

5.2.4.1 Peripheral drivers

I^2C and SPI drivers were each based on a transaction queue and a task waiting for messages on the queue. When a transaction was inserted into the queue, the corresponding task was woken, the content of the transmission buffers were sent, the reception buffers were filled and a callback function was invoked, after which the task was suspended again. I^2C peripherals were operated via interrupts and SPI transactions were performed via DMA to reduce the amount of MCU time consumed by peripheral communication.

Depending on the previously configured peripheral parameters, the drivers automatically reconfigured the peripheral to match the clock speed, phase and polarity settings of the target device which the transaction was addressed to. Even though the I^2C and SPI drivers supported asynchronous operation, the device drivers interfaced the I^2C and SPI bus drivers in blocking mode due to the sequential nature of the algorithms at the higher software layers. UART drivers had a transmission queue and task per UART peripheral, whereas the received data was passed to processing tasks via callbacks from the interrupt service routine.

5.2.4.2 ICP driver

While any task could send ICP packets, a dedicated ICP task handled the packet forwarding, interpretation of received packets, as well as the synchronisation of

ICP sequence numbers between subsystems. The ICP task on CDHS extracted a sequence of telecommands from incoming packets directed at CDHS, ADCS or PL. The telecommands were then enqueued for processing by the command scheduler which also mapped the the commands to their command handlers, depending on the command identifier, command source and destination.

5.2.4.3 Scheduling and handling of commands

The command scheduler extracted individual telecommands and executed them one by one. If one of the commands within a sequence failed, then the whole sequence was dropped and an error was logged. To avoid the loss of a radio packet with an important command, the packet could be re-transmitted several times, causing duplicated commands on CDHS. Command handlers were designed for idempotence, allowing for the same command to be executed several times in a row without harmful side effects.

ESTCube-1 CDHS had a simplified command-set which did not feature variables nor conditionals and none of the commands had return values. However, the command-set allowed command sequences to be fed to commands as arguments. This enabled simple loops, date-time scheduling of commands as well as redirection of command output to a file in any on-board file system or as ICP packets to any subsystem.

A command sequence loop simply started a timer which re-scheduled the same command sequence loop with the iteration count reduced by one. Care was taken to ensure short command execution time. In order to avoid scheduler lock-up, loop repetition intervals were limit-checked against a safe minimum. If a scheduler lock-up were to occur, then the CDHS watchdog timer would trigger a CDHS reboot, logging the issue in error log.

Operations taking too much time to be processed as a single command, were scheduled for background execution. CDHS had commands to monitor and control the background task operations.

For in-orbit profiling, CDHS had commands to measure the execution time of command-sequences, as well as to monitor the resource usage of FreeRTOS tasks during a given time. For simplicity, the CDHS scheduler only supported a single command priority. CDHS treated commands and responses the same, with the exception that the response identifier was remapped depending on the subsystem which sent the response. By using the same command scheduler for controlling and monitoring the states of other subsystems, the scheduler footprint in CDHS firmware was reduced.

CDHS supported telecommands which requested for file system info, file listings, file info, file checksum as well as telecommands which created, removed,

copied or truncated files. CDHS also supported telecommands to read from or write to files, as well as to directly read from or write to the memory of any on-board devices such as serial FRAM or flash memories, MCU Flash, MCU SRAM or any MCU registers. Additionally, there were telecommands reconfigure, get or set CDHS pin states.

5.2.4.4 Payload control

Due to simplifications in the electronics design of the payload high voltage module, the state machine for controlling its operation was rather complex. The procedure for enabling the supply for testing an electron emitter involved the switching of three power switches and a ground switch in the correct order and with the correct timing. During the procedure the voltages, current consumption and current limiter states of multiple supply lines had to be monitored by polling the measurements from EPS. If an error occurred, the same procedure would have been reversed to safely power down the payload high voltage module. Moreover, positive and negative operation modes required different order and timing of control signals, whereas for tether reel-out the high voltage supply was to be left disabled. An error could permanently damage any electronics on-board, and the reaction time had to be as short as possible, discouraging the use of ground-assisted approaches. All payload control operations had a timeout to return the spacecraft to a safe state with the payload disabled in the case that communication with the spacecraft was lost.

To facilitate quick experiments with the electron emitters without having to upgrade the whole CDHS firmware each time, support for on-board scripting was used. The scripts were prepared and verified on the spacecraft engineering model before being uploaded to the spacecraft in-orbit. Due to its simplicity and low resource requirements, the Pawn [97] scripting engine was selected for use on CDHS.

5.2.4.5 Firmware updates

In its internal flash memory, CDHS MCU hosted a custom bootloader [98], bootloader log, two firmware image slots, two configuration tables and a device table. By default, the bootloader selected the firmware image to be booted based on the state of the `CDHS_FIRMW` pin. It verified the firmware image header, and then the checksum of the firmware image, stored bootloader status messages in a dedicated section in flash, and jumped to the first instruction in the firmware.

Bootloader commands in an SPI FRAM could be used to override the

default behaviour, either to copy a firmware image from an SPI FRAM to the specified firmware image slot in flash, or to select a specific firmware image slot to booting. If the selected firmware image had an invalid header or there was a Cyclic Redundancy Check (CRC) mismatch, the other firmware image was selected for booting. On startup, the firmware initialised a volatile error log and copied bootloader log messages from flash.

From the bootloader log, the firmware counted the consecutive number of reboots with no ground communication. Upon receiving the first telecommand from the ground, CDHS added an entry to the bootloader log which reset the counting of reboots the next time that the firmware was started. If the consecutive number of reboots without ground communication exceeded 6, then a fallback configuration was loaded and CDHS entered failsafe mode where all external devices were disabled and only the most basic functionality was supported.

As part of the basic functionality, CDHS routed ICP packets, handled telecommands and allowed for firmware updates. To reduce the risk of CDHS automatically enabling compromised hardware, ground assistance was required for recovering from the fallback mode. Each firmware image was uploaded in segments, with simple bitmap-based integrity checks and CRC as described in the fourth paper [**IV**].

5.2.4.6 Configuration tables

CDHS configuration table allowed for the spacecraft operator to change MCU clock frequency, sleep and timing parameters, queue lengths, task stack margins, file system mounting order, etc. The CDHS configuration table parameters are listed in the Appendix D.1.

Each configuration table had three copies: default values supplied with firmware, non-volatile values stored in flash, and an active copy in RAM. If the active copy of the configuration table became damaged, then the non-volatile copy could either be reloaded manually on telecommand or automatically on reboot. If the non-volatile configuration table became damaged, causing firmware to crash on startup, then CDHS would automatically enter failsafe mode. From failsafe mode, the configuration table could be reset to firmware defaults with a telecommand. All critical parameters in the configuration tables were automatically validated against hard-coded safe limits which had been tested on the spacecraft engineering model.

5.2.4.7 Device table

In addition to regular configuration tables, CDHS had a non-volatile device table which allowed for CDHS MCU peripherals, software features or external devices to be enabled or disabled. When a critical issue was encountered with any of the devices, CDHS disabled it until the spacecraft operator analysed the error log, manually re-enabled the device and stored the new device configuration in the non-volatile memory.

5.2.4.8 Exception handling

Error handling was performed with a custom exception handling library for C, based on `setjmp`, `longjmp` [99] and Duff's device [100]. The library initialised an exception stack of configurable depth for each FreeRTOS task which used the exception handling scopes. At the cost of RAM for the exception stacks and some execution overhead, the exception handling library helped to improve code readability and reduce firmware flash footprint by grouping error handling into a dedicated scope.

If the allocated exception stack was not large enough to store all the sublevels of exception handling scopes, then the error was propagated to the nearest scope which had been stored. While this could cause exceptions to propagate too far up the stack tree, it helped to ensure the handling of exception regardless of the resource limitations. CDHS used numerical exceptions which the ICPTerminal mapped to human-readable error messages.

5.2.4.9 Error logging

In fallback mode, errors were logged into a volatile buffer of fixed size in MCU SRAM. In normal mode, errors along with the total error and reset count were stored in an SPI FRAM. Error log was stored in a cyclic file with constant entry size, overwriting the oldest entries with more recent events. Although it was called error log, not all of its entries were errors. The log also stored warnings and other major events such as system reboots and file system reformats. In order to avoid filling the error log with a single looped error message, an error was only logged if the new entry was not equal to the previous one. Additionally, CDHS featured error filtering with the filter mask stored in the CDHS configuration table. Errors were also counted by category and the numbers were stored in a statistics file which could be periodically downloaded from the spacecraft.

5.2.4.10 Watchdog

To reduce the probability of CDHS becoming non-responsive due to an unexpected execution loop, a watchdog was implemented. The watchdog is triggered when the command scheduler either stops or spends too much time handling a single command. When triggered, the watchdog caused a CDHS reboot.

5.2.4.11 Handling of stack overflow and hard fault

On MCU memory management fault, bus fault, memory usage fault or hard fault, FreeRTOS malloc failure or FreeRTOS stack overflow, the error codes were stored in a dedicated "dirty" section in MCU SRAM before rebooting CDHS. The "dirty" section was only cleared on a power-cycle. On firmware startup, the section was checked for magic identifiers and error codes which were stored on a fatal error, after which the firmware copied the error codes into the error log.

In the case that a FreeRTOS stack overflow occurred, the dirty section was used to store the name of the task which exceeded its stack margin. On hard fault, the contents of the most commonly used ARM registers were stored in the dirty section.

5.2.4.12 File systems

Custom file systems ECRFS and ECFFS were developed for RAM and flash memory devices with serial interface [95]. ECRFS and ECFFS provided simple data storage with direct access to file contents and were optimised for minimal flash, RAM footprints and overhead. Both ECRFS and ECFFS guaranteed file continuity in memory. This enabled read and write operations using DMA with minimal file system overhead. Both file systems supported two types of files: regular "image" files and cyclic "journal" files. Each journal file was based on a cyclic buffer the size of the file. New journal entries wrapped around the end of the file, overwriting the oldest entries. Journal files were not designed to support dynamic entry length. Regardless, throughout the mission journals with dynamic entry sizes were used most often.

5.2.5 Attitude determination and control system

5.2.5.1 Sensor measurement

The ADCS software ran on CDHS, spanning the top three software layers in Figure 12. The lowest ADCS software layer contained device drivers for gyroscopic sensors, magnetometers and sun sensor ADCs.

ADCS had magnetic torquers with a maximum magnetic moment of roughly $0.1\,\mathrm{A\,m^2}$ [101]. The magnetic torquers were controlled via EPS, due to which the device drivers for magnetic torquers relied on the ICP task.

The second ADCS software layer consisted of signal preprocessing logic. A FreeRTOS task periodically polled measurements from the four gyroscopic sensors, discarded invalid measurement values, transformed the angular rate vectors into the spacecraft reference frame and averaged the measurements from the four sensors. To minimise the delay between the acquisition of sun sensor and magnetometer measurements, the measurements were performed by a single FreeRTOS task which also extrapolated the sensor measurements and iterated the attitude determination and control algorithms. The overall data flow of the attitude determination and control task is shown in Figure 13.

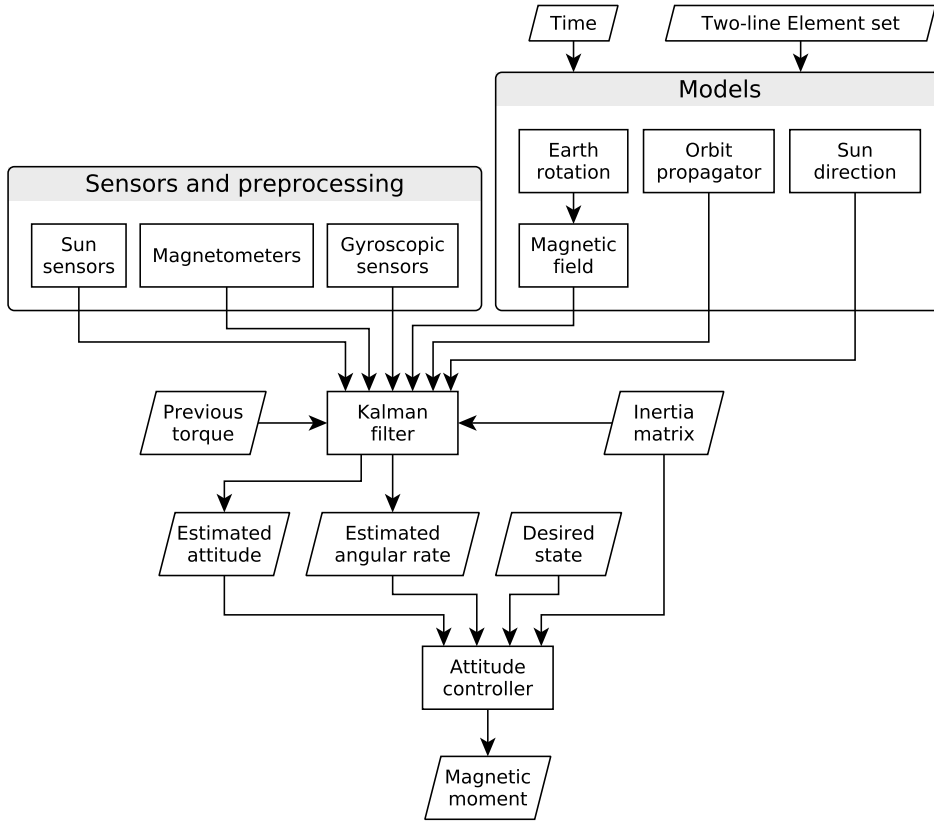

Figure 13: ESTCube-1 ADCS on-board data flow [66].

5.2.5.2 Attitude determination and control

In addition to fetching actual sensor measurements, the attitude determination and control task also propagated the spacecraft orbit, Earth's magnetic field and sun direction models for estimates based on the previous state [102]. As input, the models relied on a two-line element set [103] which specified the orbital position of the spacecraft and absolute time, both of which were updated from the ground prior to each ADCS experiment. UKF was used to provide attitude estimates based on the sensor measurements, model estimates, spacecraft inertia matrix and estimated torque from the previous iteration. The estimated attitude quaternion, together with the desired attitude were then fed to the active attitude controller [66].

An attitude controller could be selected by telecommand from the following list:

- Passive, attitude determination without attitude control.
- B-dot controller for detumbling or randomly tumbling the spacecraft.
- Magnetic torquers at a constant torque to observe the behaviour of the spacecraft in Earth's magnetic field. This controller was used to characterise the distortions in the magnetic field produced by the magnetic torquers.
- Magnetic torquers at a constant torque, with a configurable matrix to correct the distortion of magnetic torquer output.
- Pointing controller for ground or orbital targets.
- Controller for spin-up around the Z-axis.
- Controller for spin-up around a configurable diagonal axis.
- Experiment controller with the actuation of electron emitters.

5.2.5.3 Configuration table

The UKF parameters and the inertia matrix were taken from the ADCS configuration table on CDHS which could be altered with telecommands. The covariance of magnetometers could be configured, whereas the covariances of angular rate and sun sensor measurements were calculated on-board based on the sensor measurements. The ADCS software consisted of several libraries, some of which contained parameters which had to be configurable via telecommands.

All configurable parameters were marked with a C macro which assigned them to their dedicated section in memory which was then managed as the

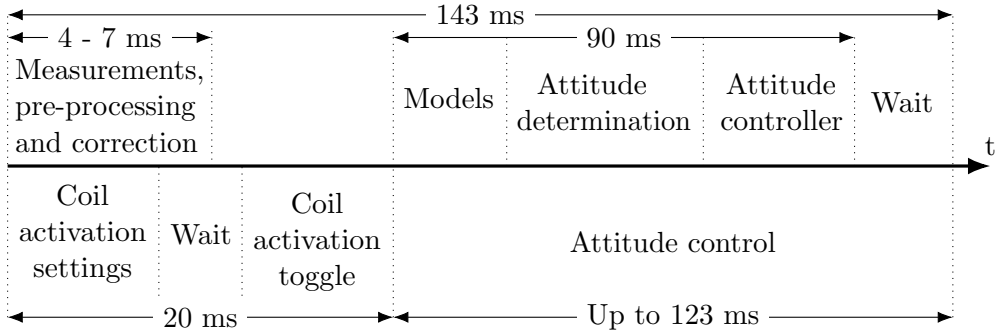

Figure 14: Timing of the ESTCube-1 attitude determination and control operations (not to scale) [104].

ADCS configuration table. Due to the lack of a single structure which would group all the parameters from all libraries, their addresses could change between firmware versions. While the sorting of symbols was used to alleviate the issue, the parameter addresses still changed when a new configurable parameter was introduced. The contents of the ADCS configuration table is listed in the Appendix D.2.

5.2.5.4 Timing

The timing of sensor measurements as well as that of attitude determination and attitude control algorithms was a compromise between control efficiency, computational overhead and potential errors due to attitude extrapolation. On ESTCube-1, attitude was extrapolated for the next iteration of attitude control. This made it possible to actuate magnetic torquers in parallel with the attitude determination and attitude control for the next iteration. The timeline for attitude determination and control at a frequency of 7 Hz is shown in Figure 14.

Based on the simulations, the ADCS algorithms would perform the best when run at a frequency of 10 Hz but the algorithms would still meet their minimum requirements at 2.5 Hz [66]. EPS allowed magnetic torquers to be actuated for up to 255 ms per attitude control iteration, with a PWM duty cycle from 0% to 98.8% in 0.39% steps. A delay of about 20 ms was needed between the telecommand to set magnetic torquer parameters and the signal to activate them. The delay helped to separate magnetometer measurements from magnetorquer actuation and ensured that EPS had enough time to process the magnetorquer control command. The magnetic actuators were active throughout the rest of the attitude determination and control iteration to

maximise the control efficiency. At a control frequency of 10 Hz, this left 80 ms for actuation, whereas at 3.6 Hz there was slightly over 255 ms for actuation. At frequencies below 3.6 Hz some control efficiency was lost due to the saturation of the actuation time.

On the other hand, long actuation periods with constant configuration are counter-productive if the spacecraft rotates more than 90° during a single actuation period. At an angular rate of $360\,^\circ\,\mathrm{s}^{-1}$, an attitude control frequency of at least 4 Hz was needed. At an angular rate of $841\,^\circ\,\mathrm{s}^{-1}$, an attitude control frequency of at least 10 Hz was needed. With all the optimisations enabled and CDHS MCU running at 72 MHz, one iteration of model propagation, attitude determination and attitude controller took between 54 ms . . . 61 ms. However, to reduce power consumption, it was preferred to run CDHS MCU at 36 MHz which yielded 79 ms . . . 109 ms per iteration. Both the MCU clock frequency and attitude control frequency could be configured with telecommands to the CDHS.

5.2.6 Camera

With minor modifications, the HAL, I^2C driver, UART driver, FRAM driver and error handling of CDHS were used on CAM. The SRAM was used to provide volatile storage for images, with ECRFS as the file system.

All ICP packets directed at, or sent by CAM were routed through CDHS. On reset, the trigger pin `CAM_SHOT` acted as `BOOT0` and when high at startup, the microcontroller executed its internal bootloader. Following the STM32 boot protocol [105], the bootloader started listening for commands on the UART lines. However, the STM32 boot protocol was not compatible with ICP. A dedicated firmware with an embedded CAM firmware was uploaded to CDHS and executed in order to program the CAM microcontroller with a firmware which already supported further firmware updates via ICP.

Chapter 6
In-orbit performance

As subsystems of the spacecraft platform, EPS, COM, CDHS and ADCS, were expected to non-intrusively fulfil their requirements and enable payload experiments. Spacecraft design and mission operations were optimised to reach the E-sail experiment within the short mission lifetime. Due to the focus on payload experiments, there was not enough time for dedicated in-orbit performance analysis of all spacecraft platform subsystems. However, the overall performance of the platform systems could be estimated to some degree from their conformance to requirements, anomalous changes in their key parameters and the utilisation of their features throughout the mission.

In this chapter, the focus is on parameters which relate to the author's contribution.

6.1 Command and data handling system

To monitor the degradation of CDHS in the LEO radiation environment, the following measurements were available: current consumption of each MCU, current consumption of the bus switches and hot redundant memories, MCU temperature and RTC temperature. Current consumption measurements were acquired by EPS and temperature measurements by CDHS. This reduced the likelihood of both current and temperature measurements being simultaneously affected by radiation in the same way.

Prolonged exposure to radiation increases leakage currents which cause an increase in both the current consumption and heat dissipation of the system [106, 107]. On a single event latch-up, a sudden increase in the current consumption and heat dissipation of the system can be expected [108]. Assuming that no permanent damage occurred, a power-cycle should restore the system to its original behaviour before the event. All CDHS supply lines from EPS had latching current limiters which power-cycled the supply on overcurrent.

6.1.1 Current consumption

Throughout the mission, none of the CDHS supply lines exceeded the 110 mA limit to trigger the EPS current limiter. However, as a means to conserve power as well as a pro-active measure against radiation damage, CDHS was

switched off between the passes unless an ADCS or payload experiment was underway. No anomalous changes were witnessed in the current consumption of memory devices nor in the current or temperature of either microcontroller.

Throughout the mission the current consumption of the CDHS MCU remained at (65 ± 7) mA or less, with the value depending on the tasks running, clock frequency and sleep settings. At day 130 of the mission, CDHS sleep mode was activated to reduce the average power draw. With the sleep mode active, the on-board MCU current measurements had an expanded uncertainty of 7 mA at 95% confidence level with a coverage factor of $k = 1.96$, based on 86465 measurements. Most often, CDHS MCU was clocked to 36 MHz with a current consumption between 27 mA ... 40 mA.

However, during the first 100 days of the mission, CDHS MCU was predominantly clocked to 72 MHz with a current consumption between 36 mA ... 60 mA. During this time period, on-board MCU current measurements were obtained with an expanded uncertainty of 2 mA at 95% confidence level with a coverage factor of $k = 1.96$, based on 39920 measurements.

The current consumption of the bus switches was typically in the range 10 mA ... 12 mA regardless of MCU activity. The expanded uncertainty of the on-board bus switch current measurements was 3 mA at 95% confidence level with a coverage factor of $k = 1.96$, based on 278251 measurements.

Increase in current consumption which could be related to radiation damage was not detected.

6.1.2 Temperature

Throughout the mission, the CDHS MCU temperature remained in the range of -5 °C ... 28 °C. The temperature of the CDHS RTC, which due to its low power dissipation (0.4 mW ... 1.32 mW) was close to the ambient temperature of the CDHS PCB, remained in the range of -5 °C ... 30 °C. Both the on-board MCU and RTC temperature measurements were obtained with an expanded uncertainty of ± 2 °C at 95% confidence level and a coverage factor of $k = 2.06$.

Increase in temperature which could be related to radiation damage was not detected.

6.1.3 Data storage

Both CDHS FRAM and NOR flash devices were used for non-volatile storage of on-board sensor measurements and housekeeping data from other platform systems. The data was stored as pairs of timestamp and telecommand response, which was straightforward to implement and enabled the selection of parameters

to be stored, at the cost of less than 15% overhead in data size. On-board measurement data was then compressed with QuickLZ [1] to reduce the data size 1.2 . . . 4 times. In addition to hosting telemetry, NOR flash on CDHS was also used to store images from CAM. Due to the high Shannon entropy of 10 bit Earth images, QuickLZ offered a very low compression ratio for images.

6.1.4 File systems

Telemetry was transferred from CDHS either as raw memory requests or as file content requests. During mission operations the two methods were used interchangeably, which is also reflected in Figure 17.

Although CDHS had one I^2C FRAM reserved for the ADCS configuration table, it was never used due to recurring issues with both I^2C buses [**III**]. Instead, configuration tables were stored in MCU flash.

One of the SPI FRAMs was used for logging on-board warnings and errors, as well as for storing simple on-board statistics. The file system metadata on the FRAM suffered from intermittent corruption and needed occasional reformatting due to immature implementation of on-board error logging.

While the flash file systems supported basic error detection and correction, the number of false positives was too large for the feature to be of use. The file systems failed to handle the non-deterministic timing of SPI flash erase and write operations. The flash file systems were eventually reconfigured with error detection disabled.

6.1.5 Firmware updates

Throughout the mission, there were 21 attempts to update CDHS firmware, 19 of which were successful. Two attempts were unsuccessful, one of them due to the failure of MCU A flash memory, the other due to the corruption of the firmware image during uploading. The ESTCube-1 firmware updating systems and their performance is described in more detail in the fourth publication [**IV**]. CDHS firmware updates with the corresponding lists of changes are listed in Appendix C. A typical CDHS firmware image of about 255 KiB took 1.5 days to upload to the spacecraft. The Shannon entropy of CDHS firmware was too high to benefit from QuickLZ compression.

After 105.3 days of operation and two successful in-orbit firmware updates, the internal flash memory of the CDHS MCU A could no longer be erased [**III**].

[1] QuickLZ [109] is a miniature compression library in C which is optimised for speed at the cost of compression ratio, which makes it attractive for embedded real-time systems.

Within the flash memory of MCU A, erasing of specific sectors within a single bank failed. Since then, MCU B was used prominently.

6.2 Camera

The performance of the on-board camera could be estimated by the number of images acquired. Throughout the mission, the camera firmware was updated only twice, which provided a good reference for its nominal operation in-orbit and made it possible to identify anomalies induced by radiation.

In total, around 300 images were downloaded throughout the mission. Figure 15 illustrates the timeline of image download from CAM throughout the mission. The total number of images taken in-orbit was about two magnitudes more, considering the extensive use of on-board image filtering based on their histogram as well as other images which were not considered "interesting" enough for download. Since CAM only had volatile memory, several images were lost due to EPS or CAM resets. The storage of CAM images in the non-volatile memory of CDHS was added at a late stage of the mission. A potential case of single event effect was detected in the CAM MCU as it entered an infinite loop at a memory address where it should not have been possible.

The RAM file system which was developed for the CDHS was also used on both the SRAM and I^2C FRAM without any issues. No issues were encountered with the image sensor I^2C communication which used the same I^2C drivers as CDHS and ADCS I^2C devices.

Figure 15: Timeline of image download from ESTCube-1 CAM.

6.3 Attitude determination and control

The performance of the attitude determination system could be measured by verifying its attitude estimate against camera images. Attitude determination accuracy of 1.44° with an uncertainty of 1.75° at 95% confidence level with a coverage factor of $k = 2$ was achieved [104]. However, ESTCube-1 camera images could only be obtained at angular rates below $7.1\,^\circ\,\mathrm{s}^{-1}$ [104] due to

which this method only enabled the verification of attitude determination accuracy at low spin rates.

To monitor the degradation of ADCS in the LEO radiation environment, the current consumption of ADCS and the temperatures of magnetometers, gyroscopic sensors and ADCs were available. While ADCS itself measured the on-board temperatures of its sensors, EPS measured the current consumption of the whole ADCS. With the current consumption and temperature measurements acquired by different systems, it should have been possible to distinguish radiation effects on ADCS sensors from radiation effects on ADCs.

EPS had a latching current limiter on the ADCS supply line to protect against single event latch-up. Both latch-up events and cumulative radiation damage should have been visible from the current consumption and temperature measurements.

The timeline of attitude determination and attitude control experiments is shown in Figure 16.

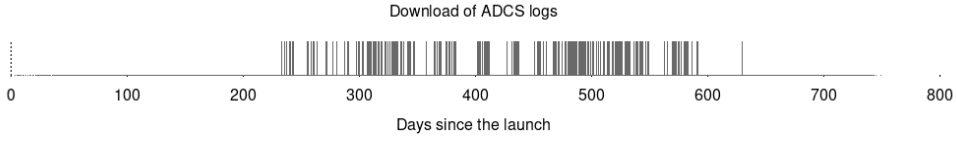

Figure 16: ADCS telemetry collection timeline on ESTCube-1 CDHS.

6.3.1 Current consumption

Throughout the mission, the current consumption of the ADCS sensors and ADCs remained below (79 ± 7) mA, with an average of (58 ± 7) mA with a 95% confidence level and a coverage factor of $k = 1.96$, based on 46394 measurements. Increase in current consumption which could be related to radiation damage was not detected.

6.3.2 Temperature

Throughout the mission, the temperatures of gyroscopic sensors and ADCs remained within $-5.5\,^{\circ}\mathrm{C} \ldots 32.2\,^{\circ}\mathrm{C}$. The temperature measurements from the gyroscopic sensors and ADCs were obtained with an expanded uncertainty of $\pm 2\,^{\circ}\mathrm{C}$ at 95% confidence level and a coverage factor of $k = 2.06$. Increase in temperature which could be related to radiation damage was not detected.

6.3.3 Sun sensors

One of the wires in the wire harness of a sun sensor became loose on final assembly, due to which one out of six sun sensors had to be discarded from on-board attitude estimation. The sun sensor measurements indicated a significant non-linearity at incidence angles close to the $\pm 45^\circ$ limits of Field of View (FoV). With a software update the FoV was clamped to $\pm 36.7^\circ$ and the function for estimating UKF sun sensor covariance matrix was updated, after which the five remaining sun sensors performed as expected. Due to the lack of a temperature corrected voltage reference for the ADCs on the spacecraft side panels, the uncertainty of sun sensor measurements was unknown.

6.3.4 Magnetometers, gyroscopic sensors

The temperature calibration coefficients obtained during the pre-launch testing campaign did not provide enough accuracy for in-orbit measurements. Magnetometer temperature calibration was re-performed in-orbit, based on the temperature measurements of the ADCs and gyroscopic sensors on the same PCB. The pre-launch calibration coefficients of the gyroscopic sensors were still applicable for attitude determination but the coefficients were fine-tuned based on the angular rate output from the UKF.

Due to the limited sampling rate of magnetometers, rolling average and derivative-based filtering of measurements were disabled prior to the tether deployment experiment.

Over time, more noise and spikes appeared in the magnetometer measurements, and I^2C communication errors became more common. Throughout the mission, the performance of both magnetometers remained very similar.

Similarly, the angular rate measurements became more congested in noise, spikes and I^2C communication issues over time. Since the launch, the second gyroscopic sensor showed anomalous quantisation error. With the second and fourth gyroscopic sensor on the same I^2C bus, both suffered from I^2C communication issues due to which both were discarded from on-board attitude estimation. Throughout the mission, the performance of the remaining two gyroscopic sensors remained very similar.

6.3.5 Attitude control

With spin-up around the Z axis as one of the primary objectives, the performance could be estimated based on the achieved angular rate and the accuracy of the spin axis. On ESTCube-1, the only actuators for attitude control were

magnetic torquers, one on each axis. Although the magnetic torquers performed according to expectations, the produced torque was distorted due to the ferromagnetic materials on the spacecraft and their residual magnetic field.

While an angular rate of $(841.4 \pm 0.5)\,^\circ\,\mathrm{s}^{-1}$ was achieved [101], the spin axis was tilted from the Z-axis by about 45° due to the residual magnetic field and distortion of the output of magnetic torquers. Due to the residual magnetic field and magnetic field distortion on magnetic torquer output, the pointing controller was not efficient enough to aim the on-board camera at Estonia. As a work-around, the B-Dot controller with a negative gain was used to tumble the spacecraft and increase the probability of capturing a photo of Estonia. With the help of a CDHS script which triggered CAM based on pointing error, and periodic imaging and histogram-based filtering of images on CAM, photos of Estonia were acquired.

6.3.6 Residual magnetic field

In-orbit demagnetisation was attempted to reduce the residual magnetic field with a magnetic moment of $0.096\,\mathrm{A\,m^2}$ [101], but the residual magnetic moment was slightly beyond the maximum output of the magnetic torquers, $0.094\,\mathrm{A\,m^2}$ [66]. Magnetometer measurements were taken before, between and after magnetisation and demagnetisation attempts on each axis. Magnetisation was attempted by enabling a magnetic torquer in one direction for about 10 minutes. Demagnetisation was attempted for 10 minutes on each magnetic torquer axis separately, with a control signal of decreasing amplitude and alternating polarity at frequencies 2.5 Hz and 5 Hz. No changes were witnessed in the residual magnetic field.

Final correction matrix for the magnetic torquers was obtained by attaching the engineering model to a string and hanging it in the middle of a Helmholtz coil. The spacecraft was powered from batteries with telecommands scheduled to acquire magnetic field measurements and activate the desired magnetic torquer for an hour. While magnetic field measurements were started on CDHS power-on, magnetic torquer was enabled about 30 minutes later, to let the spacecraft attitude stabilize enough to record its angle in respect to the magnetic field vector of the Helmholtz coil. Once the magnetic torquer had been enabled and the spacecraft attitude had stabilised again, the angle was recorded again. The test was performed for each spacecraft axis and magnetic torquer combination.

6.4 Communication system

The in-orbit performance of the communication system could be estimated based on the number of successfully exchanged packets in comparison to the number of packets discarded due to errors.

In total, the spacecraft received about 2.27 million packets from the ground stations, whereas about 289 thousand received packets were discarded due to bit stuffing or checksum errors. Many more packets were either lost in space due to the orientation of the spacecraft or on the ground due to physical obstructions such as buildings or trees surrounding the GS antenna at low elevation angles. Out of the 2.27 million packets, 851690 packets were routed through CDHS and either forwarded to or from CAM, or processed by CDHS. The rest of the packets were either handled by COM, or routed directly from COM to EPS. CDHS handled 288774 telecommands in total. The majority of telecommands sent to the spacecraft consisted of requests for file or raw memory content. The spacecraft transmitted about 2.22 million packets, most of which were responses to requests of file or raw memory content. The temporal distribution of file and memory content packets throughout the mission timeline is shown in Figure 17.

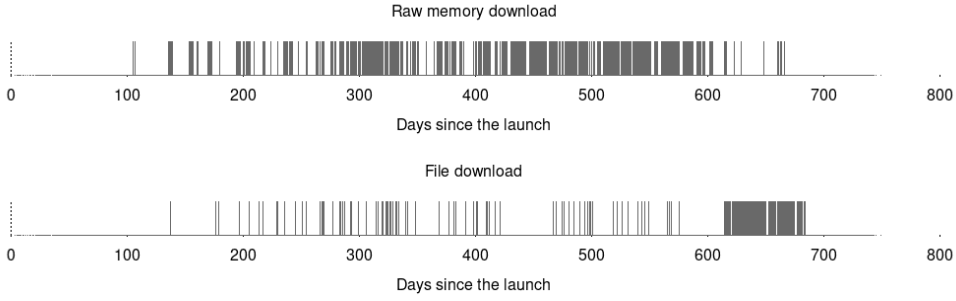

Figure 17: Timeline of raw memory (above) and file (below) download from ESTCube-1 CDHS.

Throughout the mission it occurred 323 times that COM temporarily lost its ability to transmit packets while still being able to receive telecommands. In 315 of the cases, power-cycling COM restored its functionality, whereas in 8 cases a power-cycle of the whole spacecraft was needed. In order to overcome natural packet loss and ensure that the spacecraft received the critical telecommands, the commands were transmitted repetitively. This resulted in more COM power-cycles than necessary for restoring its functionality. Most often, the issue with COM transmission occurred while transferring large amounts of

data such as camera images or measurement logs.

A part of the telecommand packet loss was due to discarded packets which could be accredited to an immature implementation of line decoding which was unable to handle long uniform bit sequences. For example, the first CDHS firmware images contained a large amount of `0x00` or `0xFF` bytes and could not be uploaded to the spacecraft. As a work-around, the source code of CDHS was adapted to produce firmware images with a minimum number of consecutive `0x00` or `0xFF` bytes. Additionally, COM did not verify the telecommand length against packet contents, which made it possible to append a string of random bytes to all telecommands sent to the spacecraft. This helped to increase the chances of COM accepting packets when transmitting them repetitively.

6.5 E-sail payload

The in-orbit performance of the electron emitters could be estimated by comparing their in-orbit volt-ampere characteristics to those measured in the lab. However, due to the highly experimental nature of the electron emitters used on ESTCube-1, their lifetimes were known to be very short.

One of the electron emitters had a lifetime of 1 minute, with a cathode current of $(300 \pm 60)\,\mu\text{A}$ at $(510 \pm 10)\,\text{V}$. The electron emitter short-circuited permanently during the first attempt to measure its volt-ampere characteristic. The other electron emitter was an open circuit and did not consume any current. During the electron emitter experiments, temporary loss of radio contact with the spacecraft was often witnessed.

The timeline of payload experiments is shown in Figure 18.

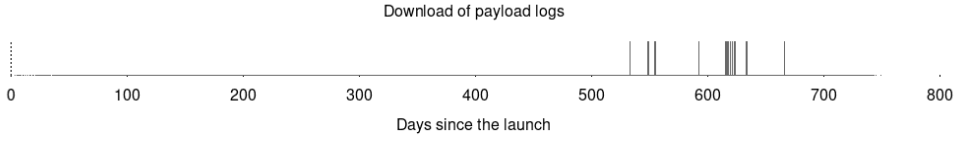

Figure 18: Payload telemetry collection timeline on ESTCube-1 CDHS.

Chapter 7
Discussions

The main objective of ESTCube-1 was to test enabling technologies for the electric solar wind sail [**I**]. The characterisation of the in-orbit performance of the platform systems developed in-house was secondary. Measurements for monitoring the in-orbit performance of CDHS [**II**] were only acquired when doing so would not compromise the mission. With a dedicated mission, it would have been easier to monitor the degradation of the system throughout the 2 years in space.

Throughout the mission, CDHS software was in constant development and improvement. On one hand, this made it possible to quickly react to the requests from the ADCS and payload teams, as well as to quickly resolve issues which were revealed during the in-orbit operation of the system [**III**]. On the other hand, the lack of a stable and constant firmware made it impossible to distinguish radiation-induced effects from regular software errors. With just two in-orbit firmware updates [**IV**] and several weeks of stress testing, an anomaly was encountered in the in-orbit behaviour of CAM that could be identified as a single event upset. In order to estimate the sensitivity to radiation, firmware should be finalised prior to launch, a thorough stress test should be carried out, and if possible, ground-based radiation tests should be performed to pre-determine the signatures of radiation damage on the hardware.

Although anomalous behaviour of CDHS was monitored throughout the mission, none of the anomalies witnessed on CDHS could be correlated to heightened solar activity nor the spacecraft passing through the South Atlantic Anomaly. If a single event latch-up had occurred, there should have been a step in current consumption and temperature measurements but no such anomalies were encountered on CDHS, ADCS nor CAM. At times, the spacecraft stopped transmitting responses to telecommands, or stopped receiving telecommands altogether. Unfortunately, the COM subsystem did not have the means to diagnose the issue and it is not known whether the issue was related to radiation damage. As COM could only fit a single firmware image with no backup, a firmware update was considered too risky to attempt. All subsystems and payloads should support in-orbit firmware updates and host at least two firmware images, one for backup [**IV**].

Although a software simulator of the FRAM and NOR flash memory devices was implemented and test-driven development was used for the custom file

systems, the test coverage could have been improved. Despite successfully passing the tests on the ground, file system issues were regularly encountered in-orbit, due to other software modules which had not been tested as thoroughly. Several of these issues were only resolved in time for follow-up missions such as ESEO cameras [110–112] and ESTCube-2 [113, 114]. The aforementioned issues caused occasional corruption or loss of data which was annoying for the spacecraft operators and teams working on data analysis but not critical for mission success. Much like the development of a communication protocol, the development and testing of custom file systems ought to be performed by a dedicated team and started as early as possible in order to reach the desired level of maturity by launch.

While ESTCube-1 ICP was more suitable for systems with low on-board resources in comparison to commonly used protocols such as CANopen [115] or CubeSat Space Protocol [116], the development of ICP cost a lot of time and effort. Although the end-result fulfilled its purpose and did not suffer from any major issues, several simplifications and work-arounds were implemented over time. The protocol was developed for a mesh topology of point-to-point links between subsystems [**II**]. However, in the long run the use of point-to-point links caused unjustified complexity in the overall design of the protocol. A shared bus with collision avoidance would have reduced the number of communication signals in the system bus and would have allowed for a simpler communication protocol between the spacecraft subsystems. This solution has been implemented on ESTCube-2 which uses a shared dual RS485 bus with dedicated signal lines for flow control to avoid packet collisions, to provide support for broadcast packets, to enable time synchronisation and high-priority transmission [117].

Throughout the mission, on-board scripts proved exceptionally useful in enabling new functionality without the need to perform a firmware update. Scripts were used to store spacecraft attitude measurements during camera imaging, to trigger image acquisition based on pointing error, and to acquire camera images during tether reel out. Scripts were also used to measure the volt-ampere characteristic of the on-board electron emitters, the effect of demagnetisation on the residual magnetic field, and the gyroscopic effect of the reel motor.

Due to the lack of low-pass filters on analogue signals, the on-board current and voltage measurements were undersampled and noisy. Although this made it possible to obtain statistics about high-frequency fluctuations, it made it difficult to determine the actual value of voltage or current consumption of a component. In order for on-board software to reliably detect anomalies in

voltage or current, properly filtered signals must be used.

From all the on-board sensors, the microelectromechanical (MEMS) magnetometers and MEMS gyroscopic sensors displayed the most significant degradation. In addition to the increasingly frequent communication errors on the I^2C bus, both the number of invalid measurements and the noise level of the magnetometers and gyroscopic sensors increased throughout the mission. One of the MEMS gyroscopic sensors suddenly started outputting measurements with a random bias [**III**]. Not only are MEMS sensors sensitive to vibration and shock, but also their in-orbit lifetime seems to be very limited. With several sensors in a hot redundant configuration, and on-board algorithms which remained functional on the loss of some sensors, the ADCS and payload experiments on ESTCube-1 could be prolonged up to 2 years. It is possible that with the help of radiation testing and proper screening, the lifetime of MEMS sensors could be extended.

Due to the time constraints described in Section 3.3, the residual magnetic moment and magnetic torquer output distortions could not be measured prior to launch. ESTCube-1 attitude measurements throughout the orbit did not match the behaviour expected based on attitude simulations. With none of its actuators active, the spacecraft aligned itself to Earth's magnetic field lines. Additional lab measurements on the engineering model were performed to acquire an estimate of the residual magnetic field and magnetic torquer output distortions for the flight model. It was shown that ESTCube-1 structure, batteries and electron emitters contain ferromagnetic materials which became magnetised during the launch [**III**]. However, since the only set of electron emitters had been mounted on the flight model, the measurements on the engineering model only provided a very rough estimate. Although the estimate was improved upon by observing the behaviour of the spacecraft in Earth's magnetic field, the estimate remained approximate. Given the time, magnetic torquers should be thoroughly calibrated and tested before the launch, especially if they are the only means of attitude control for the spacecraft.

Theoretically if the magnetic torquers produced a magnetic field stronger than that of the residual magnetic field, then it should be possible to magnetise or demagnetise the spacecraft using the magnetic torquers. However, for ESTCube-1 demagnetisation using the magnetic torquers had no effect because the residual magnetic field was in the same order of magnitude as the maximum output of the magnetic torquers [101].

The reel-out of the E-sail tether was unsuccessful. Several attempts were made to release the tether reel and tether end-mass locking mechanisms as well as to reel out the tether. While the current consumption of the motor

indicated that the motor was being actuated, the end-mass did not appear on the tether imager. In order to narrow down on the potential causes for failure, a few independent methods were used to determine whether the tether reel motor was rotating. Due to the conservation of angular momentum, if the motor rotates in one direction then the spacecraft is expected to rotate in the opposite direction. However, using the on-board gyroscopic sensors, no effect on spacecraft rotation was witnessed. It is also possible to determine rotation based on the assumption that the motor vibrations have a different spectrum, depending on whether the rotor is spinning. Using the on-board gyroscopic sensors, measurements were taken with the motor rotor fixed, and compared to the measurements taken with the rotor rotating. In order to improve the SNR, the motor was switched on and off according to a turbo code pattern. On the engineering model, it was possible to distinguish whether the rotor was rotating, based on the measurements of the reel motor vibrations from the gyroscopic sensors. In-orbit measurements, however, indicated that either the motor is not rotating or the method does not apply. Finally, consecutive images of the Earth were acquired with and without the motor being actuated. With enough delay between the consecutive images, the angular rate could be determined with enough accuracy to conclude if the motor is rotating or not. No change in angular rate was detected. The lack of sensors for feedback and diagnostics made it much more difficult to determine the cause of failure. On follow-up missions such as Aalto-1 and ESTCube-2, all locking mechanisms and motors have sensors for feedback.

Launched on June 23rd, 2017, Aalto-1 [118] was the next nanosatellite with the E-sail payload. On Aalto-1 the E-sail payload was configured as a deorbiting module [119]. At the time of writing, FORESAIL-1 [120] and ESTCube-2 are in development [113, 114, 121]. Both FORESAIL-1 and ESTCube-2 will test the E-sail payload as a deorbiting module and serve as test platforms for their follow-up missions [122].

Chapter 8
Conclusions

This thesis presents the overall architecture and requirements for ESTCube-1, the design of CDHS, its integration with the rest of the spacecraft platform and payload modules, and the in-orbit validation of the related systems.

ESTCube-1 was successfully launched on 7th of May 2013 and remained operational until 17th of February 2015. The spacecraft platform systems successfully fulfilled their requirements and the systems survived the pre-launch test campaign as well as the second Vega test launch with the accompanied vibration, shock and depressurisation. No mechanical nor electrical issues were encountered with CDHS, system bus connectors, nor the mechanical layout of the electronics boards. In-orbit operations to prepare for the E-sail experiment were the primary focus of the mission, with the in-orbit validation of spacecraft platform systems being secondary. Telemetry on the performance and degradation of CDHS was collected while the system was not actively used for attitude determination and control or payload experiments.

All spacecraft platform systems were developed specifically for the E-sail mission to enable spacecraft spin-up and attitude determination and control, and payload control at high spin rates [**I**]. ESTCube-1 CDHS was tasked with collecting measurements from attitude sensors, iterating attitude determination and control algorithms, and triggering the on-board actuators [**II**]. Methods were developed to enable simultaneous attitude determination and control, and to ensure the accurate timing of magnetic torquer actuation which made it possible to spin the spacecraft to the angular rate required for tether deployment, $360\,^\circ\,\mathrm{s}^{-1}$. At an angular rate below $7.1\,^\circ\,\mathrm{s}^{-1}$, ESTCube-1 was able to determine its attitude with an accuracy of 1.44° and an uncertainty of 1.75° [104]. With controlled spin-up, ESTCube-1 successfully demonstrated the capability to spin the spacecraft for tether deployment by achieving a record-breaking angular rate of $841\,^\circ\,\mathrm{s}^{-1}$ [101]. However, due to the residual magnetic field on the spacecraft [**III**], the real spin-axis deviated from the planned spin axis by about 45°.

With 19 successful in-orbit firmware updates [**IV**] and on-board scripting support, ESTCube-1 CDHS enabled in-orbit experimentation of attitude determination and control algorithms [35] in LEO. Configuration tables on CDHS were used to configure the attitude determination algorithm parameters as well as to switch between attitude controllers. CDHS was used to store measurements from on-board sun sensors, magnetometers and gyroscopic sensors in

the on-board memory and to downlink the telemetry for analysis. On-board scripting was used to trigger the on-board camera to take images of Estonia based on the pointing error, and test the payload tether reel motor as well as the high voltage supply and electron emitters.

The ESTCube-1 internal communication protocol ICP enabled communication between its platform systems [**II**]. Owing to the thorough on-ground testing, the protocol successfully followed its specifications on all three different microcontroller architectures. The developed ICP command terminal was not only used for testing the subsystems' compatibility to the protocol, but the terminal was also used extensively for testing subsystem features as well as for operating the spacecraft in-orbit.

During its mission, ESTCube-1 camera successfully acquired about 300 images of Earth including 5 images of Estonia. In addition to forwarding camera images, ESTCube-1 CDHS was tasked with payload control and collecting mission telemetry. While the high voltage supply and cold cathode electron emitters were also tested in-orbit, the measurement of the E-sail force was not possible due to unsuccessful tether deployment. Tether deployment failed due to a mechanical failure in the tether reel, its motor, reel lock or a combination of these [**III**].

All in all, the ESTCube-1 mission successfully demonstrated that a single unit CubeSat with magnetic torquers is capable of achieving the spin-rate required for unreeling an E-sail tether. The full demonstration of reeling out an E-sail tether is left for future missions.

Summary

This thesis presents the overall architecture and requirements for ESTCube-1 together with the design of the Command and Data Handling System (CDHS) and its integration with the rest of the spacecraft platform and the Electric Solar Wind Sail (E-sail) payload. Following the design and integration, in-orbit validation results are presented for CDHS.

E-sail is a novel propellantless propulsion technology which would enable quick interplanetary missions, asteroid rendezvous and missions with non-Keplerian orbits. ESTCube-1 was the first mission to test a prototype of the E-sail payload, for which the spacecraft was to spin around a specific axis to deploy the E-sail tether and to keep it straightened using centrifugal force. By charging the tether electrostatically as the spacecraft traverses the atmospherical plasma in Low Earth Orbit, the Coulomb force acting on the tether can be indirectly measured from a change in the spacecraft spin rate. ESTCube-1 was launched on 7 May 2013 and remained operational for 2 years and 2 weeks. While the angular rate required for tether deployment was reached successfully, tether deployment was not successful.

The focus of this thesis is on ESTCube-1 CDHS which measured the on-board attitude sensors, hosted the attitude determination and control algorithms, triggered the on-board actuators, controlled the payload and collected mission telemetry.

The capabilities to update firmware and execute scripts on CDHS enabled agile experimentation and improvement of sensor measurement filtering, attitude determination and control algorithms. The on-board telemetry logging of CDHS enabled the comparison of in-orbit performance to that of a simulation environment. ICPTerminal, developed for pre-launch testing of the spacecraft and interfaced with ESTCube-1 Mission Control System (MCS), enabled convenient in-orbit operations and telemetry processing.

E-sail tether deployment required spacecraft spin-up to at least $360\,^\circ\,\mathrm{s}^{-1}$ while maintaining the desired spin axis. To fulfil the requirement it was necessary for CDHS to measure attitude sensors and run attitude determination and control algorithms at a frequency of at least 10 Hz. CDHS was able to run the algorithms at the desired frequency while running at its maximum clock frequency of 72 MHz. To enable attitude control at high spin rates, magnetic torquers were actuated during attitude determination for the next iteration. At high spin rates the absolute and relative accuracy of on-board time and latency of actuation commands are very important. The developed system enabled

time synchronisation and actuator triggering between the electrical power system and CDHS to an accuracy of better than 1 ms which was sufficient for the desired spin rate. During tether deployment attempts, controlled spin-up to an angular rate of $841\,^{\circ}\,s^{-1}$ was successfully achieved.

The E-sail payload relied on real-time monitoring and control of its high voltage supply, electron emitters and tether charging. An autonomous payload controller was designed, implemented and tested on CDHS. The controller and on-board scripting were used to perform in-orbit validation of the payload high voltage supply and characterise the single electron emitter which surviced the launch.

In order to acquire images with the ESTCube-1 camera, CDHS was used to schedule image acquisition as well as to store and forward the images. The bootloader, peripheral and device drivers, error handling, command scheduler, and file systems developed for CDHS were also used on the ESTCube-1 camera and its follow-up projects.

All in all, by fulfilling the requirements set by the mission objectives and other spacecraft systems, ESTCube-1 CDHS helped to raise the Technological Readiness Level (TRL) of E-sail deployment.

Kokkuvõte (Summary in Estonian)

ESTCube-1 nanosatelliidi alamsüsteemide ja tarkvara disain ja karakteriseerimine

Käesolevas doktoritöös kirjeldatakse ESTCube-1 süsteemiarhitektuuri, satelliidi pardaarvuti ning sellega seotud süsteemide nõudeid ja disaini. Nõuete alusel disainitud süsteemide töö tulemuslikkust hinnati laboris sooritatud katsete ja orbiidilt kogutud tulemuste põhjal.

Elektriline päikesepuri on uudne kütusevaba käitursüsteem mis võimaldaks mittekeplerilisi orbiite ja kiireid möödalende planeetidest või asteroididest. ESTCube-1 oli esimene kosmosemissioon eesmärgiga demonstreerida elektrilise päikesepurje kontseptsiooni ja testida selleks vajalikke komponente. Satelliit tuli ümber oma telje pöörlema panna selleks, et purjetraati välja kerida ning et seda pingul hoida. Väljakeritud purjetraati elektrostaatiliselt laadides oleks saanud mõõta kulonilist tõukejõudu purjetraadi ning madalal Maa orbiidil satelliidi orbitaalliikumise sihis vastutuleva atmosfääri plasma vahel. Tõukejõudu oleks mõõdetud kaudselt, satelliidi pöörlemiskiiruse kaudu. ESTCube-1 jõudis orbiidile 7. mail 2013 ning sellel sooritati eksperimente 2 aasta ja 2 nädala vältel. Satelliidi pöörlemapanek õnnestus edukalt, kuid purjetraati ei õnnestunud välja kerida.

Käesoleva töö fookuseks on ESTCube-1 pardaarvuti mis sooritas satelliidi asendi mõõtmisi, käitas asendi määramise ja juhtimise algoritme, juhtis pardal olevaid aktuaatoreid, missioonilasti ning kogus telemeetriat.

Pardaarvuti võimaldas tarkvara uuendada ning skripte üles laadida, mis pakkus paindliku katseplatvormi sensorite näitude filtreerimise, asendi määramise ja juhtimise algoritmide katsetamiseks orbiidil. Tänu pardaarvuti võimele satelliidi süsteemidelt telemeetriat koguda ja seda säilitada, oli võimalik võrrelda algoritmide tööd orbiidil ja simulatsioonikeskkonnas. Satelliidi üleslennu eelseks testimiseks arendatud tarkvara ICPTerminal ühildati missioonijuhtimistarkvaraga et ICPTerminali ka satelliidi opereerimiseks ning orbiidilt kogutud telemeetria töötlemiseks kasutada.

Elektrilise päikesepurje traadi väljakerimiseks pidi satelliit ettenähtud pöörlemistelge säilitades saavutama pöörlemiskiiruse $360\,^\circ\,\mathrm{s}^{-1}$ või enam. Nõude täitmiseks pidi pardaarvuti suutma asendi andureid lugeda ning jooksutada asendi määramise ja juhtimise algoritme vähemalt 10 Hz sagedusel. Pardaarvuti suutis vajaliku sagedusega andureid lugeda ning algoritme käitada mikrokontrolleri maksimaalsel taktsagedusel 72 MHz. Selleks et juhtida satelliidi ori-

entatsiooni suurel pöörlemiskiirusel, aktiveeris pardaarvuti magnetmähised samaaegselt järgmise iteratsiooni asendi määramisega. Suurel pöörlemiskiirusel on oluline tagada absoluutse ja suhtelise aja täpsus satelliidi pardal. Arendatud süsteem võimaldas sünkroniseerida elektrilise toitesüsteemi ja pardaarvuti vahelist aega ning magnetmähiste lülitamist alla 1 ms veaga, millest piisas soovitud pöörlemiskiiruse saavutamiseks. Purjetraadi väljakerimise katsetuste käigus õnnestus kontrolli alt väljumata saavutada pöörlemiskiirus $841\,^{\circ}\,\mathrm{s}^{-1}$.

ESTCube-1 elektrilise päikesepurje moodul eeldas kõrgepinge toiteploki, elektronkiirgurite ning purje laadimise jälgimist ja juhtimist reaalajas. Pardaarvutile arendati autonoomne missioonilasti juhtmoodul mida kasutati koos skriptidega et orbiidil valideerida ning karakteriseerida kõrgepinge toiteplokk ja ainus elektronkiirgur mis satelliidi üleslennule vastu pidas.

Pardaarvuti säilitas ja edastas pardakaameraga tehtud fotosid ning võimaldas pildistamist ajastada. Pardaarvuti tarbeks väljatöötatud alglaadurit, seadmete ja liideste ajureid, veahaldust, käsuhaldurit ja failisüsteeme on edukalt rakendatud ka ESTCube-1 pardakaameral ning mitmetel jätkuprojektidel.

ESTCube-1 pardaarvuti täitis missiooni eesmärkidest ja teistelt satelliidi süsteemidelt tulenevad nõuded ning aitas tõsta elektrilise päikesepurje tehnoloogia valmidusastet tulevasteks missioonideks.

References

[1] P. Janhunen, "Electric sail for spacecraft propulsion," *J. Propul. Power*, vol. 20, no. 4, pp. 763–764, Jul. 2004. [Online]. Available: https://doi.org/10.2514/1.8580

[2] A. A. Quarta and G. Mengali, "Electric sail missions to potentially hazardous asteroids," *Acta Astronaut.*, vol. 66, no. 9, pp. 1506–1519, May 2010. [Online]. Available: https://doi.org/10.1016/j.actaastro.2009.11.021

[3] A. Slavinskis, P. Janhunen, P. Toivanen, K. Muinonen, A. Penttilä, M. Granvik *et al.*, "Nanospacecraft fleet for multi-asteroid touring with electric solar wind sails," in *2018 IEEE Aerospace Conference*. IEEE, Mar. 2018, pp. 1–20. [Online]. Available: https://doi.org/10.1109/AERO.2018.8396670

[4] A. A. Quarta, G. Mengali, and P. Janhunen, "Optimal interplanetary rendezvous combining electric sail and high thrust propulsion system," *Acta Astronaut.*, vol. 68, no. 5, pp. 603–621, Mar. 2011, special issue: Aosta 2009 Symposium. [Online]. Available: https://doi.org/10.1016/j.actaastro.2010.01.024

[5] P. Janhunen, P. Toivanen, J. Envall, S. Merikallio, G. Montesanti, J. G. del Amo *et al.*, "Overview of electric solar wind sail applications," *Proc. Estonian Acad. Sci.*, vol. 63(2S), pp. 267–278, May 2014. [Online]. Available: https://doi.org/10.3176/proc.2014.2S.08

[6] P. Janhunen, "Electrostatic plasma brake for deorbiting a satellite," *J. Propul. Power*, vol. 26, no. 2, pp. 370–372, Mar. 2010. [Online]. Available: https://doi.org/10.2514/1.47537

[7] P. Janhunen, "Simulation study of the plasma-brake effect," *Ann. Geophys.*, vol. 32, no. 10, pp. 1207–1216, Oct. 2014. [Online]. Available: https://doi.org/10.5194/angeo-32-1207-2014

[8] S. Mazouffre, "Electric propulsion for satellites and spacecraft: established technologies and novel approaches," *Plasma Sources Sci. Technol.*, vol. 25, no. 3, pp. 033 002:1–27, Apr. 2016. [Online]. Available: https://doi.org/10.1088/0963-0252/25/3/033002

[9] P. Fortescue, G. Swinerd, and J. Stark, Eds., *Spacecraft Systems Engineering*, 4th ed. John Wiley & Sons, Ltd., 2011.

[10] K. I. Parker, "State-of-the-art for small satellite propulsion systems," in *4th 2016 biennial Aerospace Systems Conference of the National Society of Black Engineers (NSBE)*, Aug. 2016, pp. 1–8. [Online]. Available: https://ntrs.nasa.gov/archive/nasa/casi.ntrs.nasa.gov/20160010571.pdf (Accessed 30/03/2019).

[11] J. R. Wertz, D. F. Everett, and J. J. Puschell, Eds., *Space Mission Engineering: The New SMAD.* Microcosm Press and Springer, 2011.

[12] P. Janhunen and A. Sandroos, "Simulation study of solar wind push on a charged wire: basis of solar wind electric sail propulsion," *Ann. Geophys.*, vol. 25, no. 3, pp. 755–767, Mar. 2007. [Online]. Available: https://doi.org/10.5194/angeo-25-755-2007

[13] P. Janhunen, P. K. Toivanen, J. Polkko, S. Merikallio, P. Salminen, E. Hæggström *et al.*, "Electric solar wind sail: Toward test missions," *Rev. Sci. Instrum.*, vol. 81, no. 11, pp. 111 301:1–11, Nov. 2010. [Online]. Available: https://doi.org/10.1063/1.3514548

[14] H. Kuuste, T. Eenmäe, V. Allik, A. Agu, R. Vendt, I. Ansko *et al.*, "Imaging system for nanosatellite proximity operations," *Proc. Estonian Acad. Sci.*, vol. 63(2S), pp. 250–257, May 2014. [Online]. Available: https://doi.org/10.3176/proc.2014.2S.06

[15] *CubeSat Design Specification Rev. 13*, California Polytechnic State University Std., Feb. 2014. [Online]. Available: https://static1.squarespace.com/static/5418c831e4b0fa4ecac1bacd/t/56e9b62337013b6c063a655a/1458157095454/cds_rev13_final2.pdf (Accessed 14/01/2015).

[16] G. Richardson, K. Schmitt, M. Covert, and C. Rogers, "Small satellite trends 2009-2013," in *Proceedings of the AIAA/USU Conference on Small Satellites*, vol. 29. UTAH State University, Aug. 2015, Opportunities, Trends and Initiatives, SSC-15-VII-3. [Online]. Available: https://digitalcommons.usu.edu/smallsat/2015/all2015/48/ (Accessed 17/09/2017).

[17] E. Buchen, "Spaceworks' 2014 nano/microsatellite market assessment," in *Proceedings of the AIAA/USU Conference on Small Satellites*, vol. 28.

UTAH State University, Aug. 2014, Private Endeavors, SSC-14-I-3. [Online]. Available: https://digitalcommons.usu.edu/smallsat/2014/PrivEnd/3/ (Accessed 17/09/2017).

[18] B. Doncaster, J. Shulman, J. Bradford, and J. Olds, "Spaceworks' 2016 nano/microsatellite market forecast," in *Proceedings of the AIAA/USU Conference on Small Satellites*, vol. 30. UTAH State University, Aug. 2016, Launch, SSC-16-II-1. [Online]. Available: https://digitalcommons.usu.edu/smallsat/2016/TS2Launch/1/ (Accessed 17/09/2017).

[19] S. DelPozzo, C. Williams, B. Doncaster, L. Carapaica, and D. Gerber, "Nano/microsatellite market forecast, 9th edition," SpaceWorks Enterprises, Inc., Market analysis report, 2019. [Online]. Available: https://www.spaceworks.aero/wp-content/uploads/Nano-Microsatellite-Market-Forecast-9th-Edition-2019.pdf (Accessed 23/03/2019).

[20] A. Chin, R. Coelho, L. Brooks, R. Nugent, and J. Puig-Suari, "Standardization promotes flexibility: A review of cubesats' success," in *Proc. AIAA 6th Responsive Space Conf.* AIAA, May 2008. [Online]. Available: https://citeseerx.ist.psu.edu/viewdoc/summary?doi=10.1.1.559.7055&rank=1 (Accessed 23/02/2019).

[21] S. C. Ekpo and D. George, "A system engineering analysis of highly adaptive small satellites," *IEEE Systems Journal*, vol. 7, no. 4, pp. 642–648, Dec. 2013. [Online]. Available: https://doi.org/10.1109/JSYST.2012.2198138

[22] "Utilizing the potential of NANOSATellites for the implementation of European Space Policy and space innovation," Tartu Observatory, Database developed within an FP7 project, 2013-2014, grant 313116. [Online]. Available: http://www.nanosats.eu/ (Accessed 28/07/2015).

[23] N. C. Deschamps, C. C. Grant, D. G. Foisy, R. E. Zee, A. F. J. Moffat, and W. W. Weiss, "The BRITE space telescope: Using a nanosatellite constellation to measure stellar variability in the most luminous stars," *Acta Astronaut.*, vol. 65, no. 5, pp. 643–650, Sep. 2009. [Online]. Available: https://doi.org/10.1016/j.actaastro.2009.01.026

[24] O. Koudelka, G. Egger, B. Josseck, N. Deschamp, C. C. Grant, D. Foisy *et al.*, "TUGSAT-1/BRITE-Austria — the first Austrian nanosatellite," *Acta Astronaut.*, vol. 64, no. 11, pp. 1144–1149, Jun. 2009. [Online]. Available: https://doi.org/10.1016/j.actaastro.2009.01.016

[25] Q. Schiller, D. Gerhardt, L. Blum, X. Li, and S. Palo, "Design and scientific return of a miniaturized particle telescope onboard the Colorado Student Space Weather Experiment (CSSWE) CubeSat," in *2014 IEEE Aerospace Conference*. IEEE, Mar. 2014. [Online]. Available: https://doi.org/10.1109/AERO.2014.6836372

[26] J. C. Springmann, B. P. Kempke, J. W. Cutler, and H. Bahcivan, "Initial flight results of the RAX-2 satellite," in *Proceedings of the AIAA/USU Conference on Small Satellites*, vol. 26. UTAH State University, Aug. 2012, Mission Lessons II, SSC-12-XI-5. [Online]. Available: https://digitalcommons.usu.edu/smallsat/2012/all2012/85/ (Accessed 14/01/2015).

[27] R. Zimmerman, D. Doan, L. Leung, J. Mason, N. Parsons, and K. Shahid, "Commissioning the world's largest satellite constellation," in *Proceedings of the AIAA/USU Conference on Small Satellites*, vol. 31. UTAH State University, Aug. 2017, Year in Review, SSC-17-X-03. [Online]. Available: https://digitalcommons.usu.edu/smallsat/2017/all2017/138/ (Accessed 17/09/2017).

[28] A. Escher, "Inside planet labs' new satellite manufacturing site," *TechCrunch*, Sep. 2018. [Online]. Available: https://techcrunch.com/2018/09/14/inside-planet-labs-new-satellite-manufacturing-site (Accessed 23/03/2019).

[29] H. J. Kramer, "Lemur nanosatellite constellation of Spire Global," ESA, Earth Observation Portal, 2017. [Online]. Available: https://directory.eoportal.org/web/eoportal/satellite-missions/l/lemur (Accessed 17/09/2017).

[30] H. Kayal, F. Baumann, K. Briess, and S. Montenegro, "BEESAT: A pico satellite for the on orbit verification of micro wheels," in *2007 3rd International Conference on Recent Advances in Space Technologies*. IEEE, Jun. 2007, pp. 497–502. [Online]. Available: https://doi.org/10.1109/RAST.2007.4284041

[31] F. Bruhn, "TechEdSat — CubeSat technology demonstration mission featuring plug-and-play and radiation hardened electronics," in *9th Annual CubeSat Developers Workshop*, Apr. 2012. [Online]. Available: http://mstl.atl.calpoly.edu/~bklofas/Presentations/DevelopersWorkshop2012/Bruhn_TechEdSat.pdf (Accessed 17/09/2017).

[32] N. G. Orr, J. K. Eyer, B. P. Larouche, and R. E. Zee, "Precision formation flight: The CanX-4 and CanX-5 dual nanosatellite mission," in *Proceedings of the AIAA/USU Conference on Small Satellites*, vol. 15. UTAH State University, Aug. 2007, The Upcoming Year, SSC-07-VI-02. [Online]. Available: https://digitalcommons.usu.edu/smallsat/2007/all2007/38/ (Accessed 03/09/2017).

[33] C. Bridges, S. Kenyon, C. Underwood, and V. Lappas, "STRaND-1: The world's first smartphone nanosatellite," in *2011 2nd International Conference on Space Technology (ICST 2011)*. IEEE, Sep. 2011, pp. 1–3. [Online]. Available: https://doi.org/10.1109/ICSpT.2011.6064651

[34] J. Envall, P. Janhunen, P. Toivanen, M. Pajusalu, E. Ilbis, J. Kalde *et al.*, "E-sail test payload of ESTCube-1 nanosatellite," *Proc. Estonian Acad. Sci.*, vol. 63(2S), pp. 210–221, May 2014. [Online]. Available: https://doi.org/10.3176/proc.2014.2S.02

[35] A. Slavinskis, U. Kvell, E. Kulu, I. Sünter, H. Kuuste, S. Lätt *et al.*, "High spin rate magnetic controller for nanosatellites," *Acta Astronaut.*, vol. 95, pp. 218–226, Feb. 2014. [Online]. Available: https://doi.org/10.1016/j.actaastro.2013.11.014

[36] M. Pajusalu, R. Rantsus, M. Pelakauskas, A. Leitu, E. Ilbis, J. Kalde *et al.*, "Design of the electrical power system for the ESTCube-1 satellite," *Latv. J. Phys. Tech. Sci.*, vol. 49, no. 3, pp. 16–24, Jul. 2012. [Online]. Available: https://doi.org/10.2478/v10047-012-0014-4

[37] M. Pajusalu, E. Ilbis, J. Kalde, H. Lillmaa, R. Reinumägi, R. Rantsus *et al.*, "Electrical power system for ESTCube-1: a fault-tolerant COTS solution," in *Proceedings of International Astronautical Congress*. IAF, Oct. 2012, pp. 7139–7144.

[38] M. Pajusalu, E. Ilbis, T. Ilves, M. Veske, J. Kalde, H. Lillmaa *et al.*, "Design and testing of the electrical power system for ESTCube-1," *Proc. Estonian Acad. Sci.*, vol. 63(2S), pp. 232–241, May 2014. [Online]. Available: https://doi.org/10.3176/proc.2014.2S.04

[39] *European Cooperation for Space Standardization, ECSS-E-HB-11A, Space engineering: Technology readiness level (TRL) guidelines*, ESA Std., Mar. 2017. [Online]. Available: https://ecss.nl/home/ecss-e-hb-11a-technology-readiness-level-trl-guidelines-1-march-2017/ (Accessed 14/04/2019).

[40] R. Kurppa, J. Ukkonen, S. Kiprich, H. Seppänen, P. Janhunen, and E. Hæggström, "Method for electric solar wind sail tether production," in *European Planetary Science Congress 2010*, vol. 294, Sep. 2010, pp. 429–455, MT6 Photonic Solar Sail and Electric Solar Wind Sail: new opportunities for Solar System and Planetary exploration missions (Workshop), EPSC2010-294. [Online]. Available: https://meetingorganizer.copernicus.org/EPSC2010/EPSC2010-294.pdf (Accessed 30/05/2019).

[41] T. Rauhala, H. Seppänen, J. Ukkonen, S. Kiprich, G. Maconi, P. Janhunen, and E. Hæggström, "Automatic 4-wire heytether production for the electric solar wind sail," in *IMAPS Topical Workshop and Tabletop Exhibition on Wire Bonding*, Sep. 2013, pp. 1–7. [Online]. Available: https://electric-sailing.fi/papers/Rauhala_IMAPS_wirebonding_2013_final.pdf (Accessed 30/05/2019).

[42] H. Seppänen, T. Rauhala, S. Kiprich, J. Ukkonen, M. Simonsson, R. Kurppa *et al.*, "One kilometer (1 km) electric solar wind sail tether produced automatically," *Rev. Sci. Instrum.*, vol. 84, no. 9, pp. 095 102:1–4, Sep. 2013. [Online]. Available: https://doi.org/10.1063/1.4819795

[43] Y. Chen, R. Huang, X. Ren, L. He, and Y. He, "History of the tether concept and tether missions: A review," *ISRN Astronomy and Astrophysics*, vol. 2013, pp. 1–7, Jan. 2013. [Online]. Available: https://doi.org/10.1155/2013/502973

[44] M. Kruijff and E. J. van der Heide, "Qualification and in-flight demonstration of a European tether deployment system on YES2," *Acta Astronaut.*, vol. 64, no. 9, pp. 882–905, May 2009. [Online]. Available: https://doi.org/10.1016/j.actaastro.2008.10.014

[45] T. Watanabe, H. A. Fujii, T. Kusagaya, H. Sahara, H. Kojima, S. Takehara *et al.*, "T-Rex: Bare electro-dynamic tape-tether technology experiment on sounding rocket S520," *The Journal of Space Technology and Science*, vol. 26, no. 1, pp. 14–20, 2012. [Online]. Available: https://doi.org/10.11230/jsts.26.1_14

[46] S. S. Gates, S. M. Koss, and M. F. Zedd, "Advanced tether experiment deployment failure," *Journal of Spacecraft and Rockets*, vol. 38, no. 1, pp. 60–68, Feb. 2001. [Online]. Available: https://doi.org/10.2514/2.3655

[47] R. P. Hoyt and R. L. Forward, "Alternate interconnection hoytether failure resistant multiline tether," American Patent 6 286 788B1,

2000. [Online]. Available: https://patents.google.com/patent/US6286788 (Accessed 06/04/2019).

[48] R. P. Hoyt and R. L. Forward, "Performance of the Terminator Tether™ for autonomous deorbit of LEO spacecraft," in *35th Joint Propulsion Conference and Exhibit*, vol. 38. AIAA, Jun. 1999, AIAA-99-2839. [Online]. Available: https://doi.org/10.2514/6.1999-2839

[49] *ECSS-M-ST-10C Rev.1 - Project planning and implementation*, European Cooperation for Space Standardization Std., Mar. 2009. [Online]. Available: http://ecss.nl/standard/ecss-m-st-10c-rev-1-project-planning-and-implementation/ (Accessed 17/01/2018).

[50] ESTCube team, "ESTCube-1 space system and mission description: Final document, phase A (EC1-A-MGM-1-SSMD)," University of Tartu, Report, 2010. [Online]. Available: https://sites.google.com/a/estcube.eu/estonian-student-satellite-program/estcube-1/missiooni-raportid/EC1-A-MGM-1-SSMD.pdf (Accessed 16/10/2017).

[51] A. de Ruiter, "A fault-tolerant magnetic spin stabilizing controller for the JC2Sat-FF mission," *Acta Astronaut.*, vol. 68, no. 1, pp. 160–171, Jan. 2011. [Online]. Available: https://doi.org/10.1016/j.actaastro.2010.07.012

[52] P.-S. Hur, R. G. Melton, and D. B. Spencer, "Meeting science requirements for attitude determination and control in a low-power, spinning nanosatellite," *Journal of Aerospace Engineering, Sciences and Applications*, vol. 1, no. 1, pp. 25–33, Apr. 2008.

[53] H. Kuuste, "ESTCube-1 tether end mass imaging system design and assembly," Bachelor Thesis, University of Tartu, May 2012. [Online]. Available: https://dspace.ut.ee/handle/10062/25658 (Accessed 18/03/2018).

[54] M. Vellak, "Using space-dynamics library OREKIT for optimal satellite contacts planning," Bachelor Thesis, University of Tartu, May 2013. [Online]. Available: https://dspace.ut.ee/handle/10062/32941 (Accessed 21/05/2019).

[55] E. J. Okugbeni, "Security implementation of Mission Control System for ESTCube-1 satellite," Master's thesis, University of Tartu, May 2014.

[Online]. Available: https://dspace.ut.ee/handle/10062/56035 (Accessed 21/05/2019).

[56] A. Lobjakas, "Hardware-in-the-loop testing module for Mission Control System," Bachelor Thesis, University of Tartu, May 2016. [Online]. Available: https://dspace.ut.ee/handle/10062/56251 (Accessed 21/05/2019).

[57] K.-L. Kusmin, "Application of Scrum methodology in long-term student projects on the example of ESTCube-1 Mission Control System," Bachelor Thesis, University of Tartu, May 2012. [Online]. Available: https://dspace.ut.ee/handle/10062/32899 (Accessed 21/05/2019).

[58] "Vega user's manual: Issue 4 revision 0, april 2014," Arianespace, User Manual, Apr. 2014. [Online]. Available: http://www.arianespace.com/wp-content/uploads/2015/09/Vega-Users-Manual_Issue-04_April-2014.pdf (Accessed 29/10/2017).

[59] *CubeSat Deployers*, ISIS - Innovative Solutions In Space B.V. Std., Feb. 2016. [Online]. Available: https://www.isispace.nl/wp-content/uploads/2016/02/CubeSat-deployers-Brochure-web-compressed.pdf (Accessed 14/04/2018).

[60] R. Soosaar and J. Viru, "ESTCube-1 preliminary system requirements and design: Environment, phase B (EC1-B-ENVI-1-PSRD)," University of Tartu, Report, 2010.

[61] R. Soosaar, "Space environment and how it affects the spacecraft in it," Master's thesis, University of Tartu, May 2009. [Online]. Available: https://sites.google.com/a/estcube.eu/estcube-1/Home/presentations/SpaceEnvironment.pdf (Accessed 21/05/2019).

[62] T. Peet, T. Ani, and K. Prants, "ESTCube-1 preliminary system requirements and design: Thermal control system, phase B (EC1-B-TCS-1-PSRD)," University of Tartu, Report, 2010.

[63] T. Peet, "Thermal control of ESTCube-1 spacecraft," Bachelor Thesis, University of Tartu, May 2012.

[64] T. Ilves, "ESTCube-1 electrical power system operation software," Master's thesis, University of Tartu, May 2013. [Online]. Available: https://dspace.ut.ee/handle/10062/32457 (Accessed 01/11/2017).

[65] E. Ilbis, "ESTCube-1 electrical power system – design, implementation and testing," Bachelor Thesis, University of Tartu, May 2013. [Online]. Available: https://dspace.ut.ee/handle/10062/32450 (Accessed 01/11/2017).

[66] A. Slavinskis, E. Kulu, J. Viru, R. Valner, H. Ehrpais, T. Uiboupin *et al.*, "Attitude determination and control for centrifugal tether deployment on ESTCube-1 nanosatellite," *Proc. Estonian Acad. Sci.*, vol. 63(2S), pp. 242–249, May 2014. [Online]. Available: https://doi.org/10.3176/proc.2014.2S.05

[67] S. J. Julier and J. K. Uhlmann, "New extension of the Kalman filter to nonlinear systems," in *Proc. SPIE, Signal Processing, Sensor Fusion, and Target Recognition VI*, I. Kadar, Ed., vol. 3068, Jul. 1997. [Online]. Available: https://doi.org/10.1117/12.280797

[68] J. Kalde, "Piezoelectric motor driver for CubeSat," Bachelor Thesis, University of Tartu, May 2012. [Online]. Available: https://dspace.ut.ee/handle/10062/32437 (Accessed 09/11/2017).

[69] *PC/104 Specification, version 2.3*, PC/104 Consortium Std., Jun. 1996. [Online]. Available: https://www.versalogic.com/support/pdf/pc104-23.pdf (Accessed 07/11/2017).

[70] *PC/104-Plus Specification, version 2.3*, PC/104 Embedded Consortium Std., Oct. 2008. [Online]. Available: https://pc104.org/wp-content/uploads/2015/02/PC104_Plus_v2_32.pdf (Accessed 07/11/2017).

[71] *CubeSat Kit PCB Specification*, Pumpkin Incorporated Std., Sep. 2003. [Online]. Available: http://www.cubesatkit.com/docs/CSK_PCB_Spec-A5.pdf (Accessed 04/01/2018).

[72] "Eagle," 1988. [Online]. Available: https://www.autodesk.com/products/eagle/overview (Accessed 15/06/2019).

[73] "SN74CB3Q16211 24-bit 2.5v / 3.3v low-voltage FET bus switch," Texas Instruments, Datasheet, May 2004. [Online]. Available: http://www.ti.com/lit/ds/symlink/sn74cb3q16211.pdf (Accessed 29/11/2017).

[74] "STM32F103xC, STM32F103xD, STM32F103xE: High-density performance line, ARM-based 32-bit MCU with 256 to 512KB Flash, USB, CAN, 11 timers, 3 ADCs, 13 communication interfaces," STMicroelectronics, Datasheet, Nov. 2015. [Online]. Available:

https://www.st.com/resource/en/datasheet/cd00191185.pdf (Accessed 19/11/2017).

[75] J. Namkung, , and J. Patel, "Reliability and endurance of FRAM: A case study," in *Non-volatile Memory Technology Symposium*. JPL TRS, Nov. 2002. [Online]. Available: http://hdl.handle.net/2014/10677 (Accessed 29/11/2017).

[76] C. Sansoè and M. Tranchero, "Use of FRAM memories in spacecrafts," in *Ferroelectrics-Applications*, M. Lallart, Ed. InTech, Aug. 2011, ch. 10, pp. 213–230. [Online]. Available: https://doi.org/10.5772/18529

[77] "FM25V10 1-Mbit (128 K x 8) serial (I^2C) F-RAM," Cypress Semiconductor Corporation, Datasheet, Dec. 2018. [Online]. Available: https://www.cypress.com/file/41666/download (Accessed 31/05/2019).

[78] "FM25V20A 2-Mbit (256 K x 8) serial (SPI) F-RAM," Cypress Semiconductor Corporation, Datasheet, May 2019. [Online]. Available: https://www.cypress.com/file/141396/download (Accessed 31/05/2019).

[79] "S25FL128S/S25FL256S 128-Mbit (16-Mbyte) / 256-Mbit (32-Mbyte) 3.0V SPI flash memory," Cypress Semiconductor Corporation, Datasheet, Apr. 2019. [Online]. Available: https://www.cypress.com/file/448601/download (Accessed 31/05/2019).

[80] "DS3234 extremely accurate SPI bus RTC with integrated crystal and SRAM," Maxim Integrated Products, Inc., Datasheet, Mar. 2015. [Online]. Available: https://datasheets.maximintegrated.com/en/ds/DS3234.pdf (Accessed 31/05/2019).

[81] "MT9V011 - 1/4-inch VGA digital image sensor," Micron, Datasheet, Jan. 2005. [Online]. Available: http://www.electronics123.net/amazon/datasheet/MT9V011.pdf (Accessed 31/05/2019).

[82] "STM32F215xx, STM32F217xx: ARM-based 32-bit MCU with up to 1MB Flash, camera interface," STMicroelectronics, Datasheet, Aug. 2016. [Online]. Available: https://www.st.com/resource/en/datasheet/stm32f215re.pdf (Accessed 18/03/2019).

[83] "IS61WV102416ALL, IS61WV102416BLL, IS64WV102416BLL: 1M x 16 high-speed asynchronous CMOS static RAM with 3.3V supply," ISSI, Datasheet, Jun. 2014. [Online]. Available: http://www.issi.com/WW/pdf/61WV102416ALL.pdf (Accessed 18/03/2019).

[84] W. Simpson, *RFC1549: PPP in HDLC Framing*, Internet Engineering Task Force (IETF) Std., Dec. 1993. [Online]. Available: https://tools.ietf.org/html/rfc1549#section-4 (Accessed 25/03/2018).

[85] "Pyside," Python bindings for the Qt framework. [Online]. Available: https://wiki.qt.io/Qt_for_Python (Accessed 15/06/2019).

[86] H. Nord and E. Chambe-Eng, "Qt," 1991, cross-platform application and user interface framework. [Online]. Available: https://www.qt.io/ (Accessed 15/06/2019).

[87] I. Sünter, "Practical training in computer engineering: Adapting ICPTerminal for ESTCube-1 mission operations," University of Tartu, Traineeship report, May 2014.

[88] U. Kvell, "Satellite communications center in the university of tartu," Bachelor Thesis, University of Tartu, May 2009. [Online]. Available: https://sites.google.com/a/estcube.eu/estcube-1/Home/presentations/Tartu_Ulikooli_Satelliitside_Keskus-UrmasKvell_2009.pdf (Accessed 29/05/2019).

[89] J. Mõttus, "Characterisation of satellite groundstation antenna system," Master's thesis, Estonian Aviation Academy, May 2009. [Online]. Available: https://sites.google.com/a/estcube.eu/estcube-1/Home/presentations/Satelliitside_antennis%C3%BCsteemi_parameetrite_m%C3%A4%C3%A4ramine.pdf (Accessed 20/05/2019).

[90] K. Voormansik, "Satellite signal strength measurements with the international space university ground station and the university of tartu ground station," Master's thesis, University of Tartu, Jun. 2009. [Online]. Available: http://astro.u-strasbg.fr/~koppen/GENSO/docs/VoormansikThesis.pdf (Accessed 20/05/2019).

[91] K. Kivistik, "Preselector module for the ground station of the student satellite," Bachelor Thesis, Estonian Aviation Academy, May 2012.

[92] I. Mahhonin, "Satellites tracking optimizations for ground stations," Bachelor Thesis, University of Tartu, May 2013. [Online]. Available: https://dspace.ut.ee/handle/10062/32461 (Accessed 01/06/2019).

[93] N. Andresen, "Ground station's software development for the observatory of tartu," Master's thesis, University of Tartu, May 2017. [Online]. Available: https://dspace.ut.ee/handle/10062/56545 (Accessed 21/05/2019).

[94] L. Joost, "Demodulation of BPSK using Software Defined Radio," Bachelor Thesis, University of Tartu, May 2016. [Online]. Available: https://dspace.ut.ee/handle/10062/53073 (Accessed 21/05/2019).

[95] I. Sünter, "Software for the ESTCube-1 command and data handling system," Master's thesis, University of Tartu, May 2014. [Online]. Available: https://dspace.ut.ee/handle/10062/43113 (Accessed 26/05/2014).

[96] R. Barry, "The FreeRTOS^{TM} kernel," 2003. [Online]. Available: https://www.freertos.org (Accessed 15/06/2019).

[97] "PAWN embedded scripting language," ITB CompuPhase, Scripting language, Oct. 1999. [Online]. Available: https://www.compuphase.com/pawn/pawn.htm (Accessed 25/03/2018).

[98] K. Tarbe, "Bootloader for ESTCube-1 command and data handling system and camera module," Bachelor Thesis, University of Tartu, May 2013. [Online]. Available: https://dspace.ut.ee/handle/10062/32839 (Accessed 31/05/2019).

[99] T. Schotland and P. Petersen, "Exception Handling in C without C++," OnTime Real-Time and System Software, Report, 1999. [Online]. Available: http://www.on-time.com/ddj0011.htm (Accessed 25/03/2018).

[100] T. Duff, "Duff's device," LucasFilm, Copy of mail exchange, Aug. 1988. [Online]. Available: https://www.lysator.liu.se/c/duffs-device.html (Accessed 25/03/2018).

[101] H. Ehrpais, J. Kütt, I. Sünter, E. Kulu, A. Slavinskis, and M. Noorma, "Nanosatellite spin-up using magnetic actuators: ESTCube-1 flight results," *Acta Astronaut.*, vol. 128, pp. 210–216, Nov. 2016. [Online]. Available: https://doi.org/10.1016/j.actaastro.2016.07.032

[102] A. Slavinskis, "ESTCube-1 attitude determination," Ph.D. Thesis, University of Tartu, Oct. 2015. [Online]. Available: https://dspace.ut.ee/handle/10062/49230 (Accessed 04/06/2019).

[103] T. S. Kelso, *NORAD Two-Line Element Set Format*, Center for Space Standards and Innovation (CSSI) Std., Dec. 2000. [Online]. Available: https://www.celestrak.com/NORAD/documentation/tle-fmt.asp (Accessed 25/03/2018).

[104] A. Slavinskis, H. Ehrpais, H. Kuuste, I. Sünter, J. Viru, E. Kulu *et al.*, "Flight results of ESTCube-1 attitude determination system," *J. Aerosp. Eng.*, vol. 29, no. 1, pp. 04 015 014:1–7, Apr. 2015. [Online]. Available: https://doi.org/10.1061/(ASCE)AS.1943-5525.0000504

[105] "AN3155 application note: USART protocol used in the STM32 bootloader," STMicroelectronics, Tech. Rep., Apr. 2019. [Online]. Available: https://www.st.com/content/ccc/resource/technical/document/application_note/51/5f/03/1e/bd/9b/45/be/CD00264342.pdf/files/CD00264342.pdf/jcr:content/translations/en.CD00264342.pdf (Accessed 31/05/2019).

[106] H. Kvedalen, "Study of radiation effects in COTS semiconductors for use in high energy physics experiments," Master's thesis, University of Oslo, May 2002. [Online]. Available: https://folk.uio.no/hallvark/Kvedalen.pdf (Accessed 02/06/2019).

[107] M. Amrbar, F. Irom, S. M. Guertin, and G. Allen, "Heavy ion single event effects measurements of Xilinx Zynq-7000 FPGA," in *2015 IEEE Radiation Effects Data Workshop (REDW)*. IEEE, Jul. 2015, pp. 1–4. [Online]. Available: https://doi.org/10.1109/REDW.2015.7336714

[108] S. M. Guertin, "Cubesat processor radiation efforts," in *5th NASA Electronic Parts and Packaging (NEPP) Program Electronic Technology Workshop*, Jun. 2014.

[109] R. Lenhardt and J. Alakuljala, "Gipfeli - High Speed Compression Algorithm," in *2012 Data Compression Conference (DCC)*, J. A. Storer and M. W. Marcellin, Eds. IEEE Computer Society, 2012, pp. 109–118. [Online]. Available: https://doi.org/10.1109/DCC.2012.19

[110] I. Sünter, H. Kuuste, J. Kütt, E. Ilbis, A. Agu, I. Iakubivskyi *et al.*, "Dual-camera payload for ESEO," in *Proceedings of Small Satellites, Systems & Services Symposium (4S)*. ESA Publications Division, Jun. 2016, pp. 1–10, Academic Projects, S13-4-145.

[111] I. Sünter, H. Kuuste, A. Slavinskis, A. Agu, E. Ilbis, G. Olentšenko *et al.*, "Design and testing of a dual-camera payload for ESEO," in *Proceedings of International Astronautical Congress*. IAF, Sep. 2016, pp. 1–10, Small Earth Observation Missions, IAC–16–B4.4.3,x31978.

[112] I. Sünter, H. Kuuste, and J. Kütt, "Optical characterisation of the ESEO optical payload," in *Proceedings of the 2nd Symposium on Space*

Educational Activities, L. Bacsardi and K. Kovacs, Eds., vol. 2. Budapest University of Technology and Economics, Apr. 2018, pp. 123–126.

[113] H. Ehrpais, I. Sünter, E. Ilbis, J. Dalbins, I. Iakubivskyi, E. Kulu *et al.*, "ESTCube-2 mission and satellite design," in *Proceedings of Small Satellites, Systems & Services Symposium (4S)*. ESA Publications Division, Jun. 2016, pp. 1–7, Mission Analysis, CS03-3-305.

[114] I. Iakubivskyi, H. Ehrpais, J. Dalbins, E. Oro, E. Kulu, J. Kütt *et al.*, "ESTCube-2 mission analysis: plasma brake experiment for deorbiting," in *Proceedings of International Astronautical Congress*. IAF, Sep. 2016, pp. 1–10, 45th Student Conference, IAC-16,E2,4,4,x33190.

[115] *CiA 301 version 4.2.0: CANopen Application Layer and Communication Profile*, CAN in Automation e.V. Std., Feb. 2011. [Online]. Available: https://www.can-cia.org/groups/specifications/ (Accessed 28/08/2015).

[116] *CubeSat Space Protocol (CSP)*, AAUSAT3, GomSpace Std., 2010. [Online]. Available: https://github.com/libcsp/libcsp (Accessed 31/05/2019).

[117] S. Tammesoo, "Internal Communication Protocol for ESTCube-2 subsystems," Bachelor Thesis, University of Tartu, May 2015. [Online]. Available: https://dspace.ut.ee/handle/10062/50465 (Accessed 08/04/2018).

[118] J. Praks, A. Kestilä, P. Niemelä, A. Näsilä, H. Leppinen, B. Riwanto *et al.*, "Aalto-1 nanosatellite mission status and initial observations," in *Proceedings of the 9th European CubeSat Symposium*, Nov. 2017, pp. 124–127.

[119] A. Kestil, T. Tikka, , P. Peitso, J. Rantanen, A. Näsilä *et al.*, "Aalto-1 nanosatellite — technical description and mission objectives," *Geosci. Instrum. Method. Data Syst.*, vol. 2, no. 1, pp. 121–130, Feb. 2013. [Online]. Available: https://doi.org/10.5194/gi-2-121-2013

[120] M. Palmroth, J. Praks, R. Vainio, P. Janhunen, E. K. J. Kilpua, N. Y. Ganushkina *et al.*, "FORESAIL-1 cubesat mission to measure radiation belt losses and demonstrate de-orbiting," *J. Geophys. Res. Space Physics*, vol. 124, May 2019. [Online]. Available: https://doi.org/10.1029/2018JA026354

[121] I. Iakubivskyi, H. Ehrpais, H. Kuuste, I. Sünter, E. Ilbis, M.-L. Aru *et al.*, "ESTCube-2 plasma brake payload for effective deorbiting," in *Proc. 7th*

European Conference on Space Debris, Apr. 2017, Debris Mitigation: Design Solutions.

[122] I. Iakubivskyi, P. Janhunen, J. Praks, V. Allik, K. Bussov, B. Clayhills *et al.*, "Coulomb Drag Propulsion experiments of ESTCube-2 and FORESAIL-1," in *Tethers in Space Proceedings*, May 2019, submitted.

Acknowledgements

The author gratefully acknowledges all the present and former ESTCube members and supervisors for their hard work on the ESTCube-1 and ESEO missions. The author is grateful to the Aalto, ESTCube and FORESAIL teams for taking the responsibility to continue with the E-sail experiments. Thanks to the hard work and persistence of Andris Slavinskis, Ph.D., Hendrik Ehrpais, Robert Märk and Erik Ilbis, ESTCube-2 development is progressing steadily.

Without the guest professor of University of Tartu and a researcher at the Finnish Meteorological Institute, Pekka Janhunen, Ph.D., the E-sail technology would not have been invented and ESTCube-1 would have had to settle for a less ambitious mission.

Without Prof. Mart Noorma, there would not have been an ESTCube-1. Without his encouragement and supervision, the author would not have considered enrollment to the Ph.D. programme. It was Mart's firm vision and enthusiasm that inspired the students to get together and achieve something beyond conceivable. Thanks to the guidance of Kārlis Zālīte, Silver Lätt, Jouni Envall, Tõnis Eenmäe and Viljo Allik it was possible to convert a rough concept into a fully functional spacecraft with several ground stations to support the mission operations. The author is grateful to Tõnis Eenmäe for supervising the author's bachelor thesis on the development of CDHS electronics prototype for ESTCube-1 and to Kārlis Zālīte, Ph.D., for supervising the author's master's thesis on ESTCube-1 CDHS software development and coordinating the writing of the author's first paper. Almost all the in-orbit operations were performed by the most conscientious student Erik Kulu, thanks to whom other students could concentrate on other aspects of the mission.

In addition to supervising the students, Tartu Observatory (now a part of the University of Tartu) offered full access to their facilities which proved to be most helpful. The author is exceptionally thankful to the director of Tartu Observatory, Anu Reinart, Ph.D., for her unwavering support to the ESTCube project.

The research was supported by the "Charles Villmann" scholarship and the European Regional Development Fund and the Investment and Development Agency of Latvia via the Latvian Electronic and Optical Equipment Competence Centre in Production Sector (Agreement nL-KC-11-0006) project number 2.9. Participation at conferences was enabled by the "Kristjan Jaak" and "Dora+" scholarships from the Archimedes Foundation.

The ESTCube-1 project was supported by the European Space Agency

(ESA) and the Ministry of Economic Affairs and Communication of Estonia via the ESA PECS project "Technology demonstration for space debris mitigation and electric propulsion on ESTCube-1 student satellite". The European Commission supported ESTCube-1 through the EstSpace FP7 project, the ESAIL FP7 project, and through the Erasmus training programme. The project owes a significant part of its success to the unwavering support from Madis Võõras and Ene Ergma.

Republic of Estonia
Ministry of Economic Affairs and Communications

Appendix A
Spacecraft requirements

The following tables provide a non-exhaustive overview of ESTCube-1 requirements. The requirements were derived from the system architecture in Section 3.4 and mission objectives in Section 3.2. The requirements that relate the most to the author's contribution, are elaborated upon in Section 4.

Table 1: Table of general requirements.

Id.	Pri.	Description	Rationale
SYS-1	High	Spacecraft (S/C) must have a near-polar orbit.	E-Sail experiment. Equatorial launches are rare and would pose communication issues with Tartu GS.
SYS-2	High	S/C must have a sun-synchronous orbit.	Earth imaging, additional power during passes.
SYS-3	High	Orbit altitude would be between 600 km . . . 800 km.	Typical for sun-synchronous (near-polar) orbits.
SYS-4	High	Mission lifetime of 1 year with a shielding of 1 mm of aluminum.	Mission lifetime, S/C formfactor and its mass budget.
SYS-5	High	S/C shall be compatible with the 1U deployer from the launch broker.	Shall use the launch broker Innovative Solutions In Space.
SYS-6	High	Out-gassing rate of materials less than 1% TML and 0.1% CVCM.	CubeSat standard.
SYS-7	High	AP capable of charging the EPS batteries.	Pre-launch charging of batteries.
SYS-8	High	AP capable of delivering ICP packets to EPS, COM or CDHS.	Pre-flight firmware updates and verification.
SYS-9	High	Possible to power-cycle the S/C.	Recovery from transient hardware issues.
SYS-10	High	Possible to reset any platform system (PSYS) on telecommand (TC).	Recovery from software issues.
SYS-11	High	COM and EPS always powered, other systems powered on demand.	Minimize power consumption.
SYS-12	High	All PSYS use either 3.3 V or 5 V supplies provided by EPS.	Minimise the number of voltage regulators.
SYS-13	High	Payloads are supplied with 3.3 V, 5 V, and / or 12 V.	Minimise the number of voltage regulators.
SYS-14	High	All PSYS will have either 4 or 6 layer PCBs, 1 mm thick.	Panelization of PCBs for manufacturer.
SYS-15	High	The design of all PSYS PCBs must follow the template (Figure 6).	Mechanical compatibility of systems.
SYS-16	Medium	All PSYS components with industrial (−40 °C . . . 100 °C) or automotive (−40 °C . . . 125 °C) operating temperature range.	Wide operating temperature range.

Table 1: Table of general requirements.

Id.	Pri.	Description	Rationale
SYS-17	High	PSYS must not produce fluctuations on the supply lines that interfere with other PSYS.	Electrical compatibility of systems.
SYS-18	High	PSYS must withstand 1×10^{-6} mbar without overheating.	Thermal compatibility of systems.
SYS-19	High	All system bus power lines are limited to ≤ 3 A.	Specification of the PC104+ connectors.
SYS-20	Medium	All inter-subsystem signals run through the system bus connector.	Simplify assembly.
SYS-21	Medium	At least 1/3 of the system bus pins reserved for ground.	Minimize Electro-Magnetic Interference (EMI).
SYS-22	Medium	System bus high frequency pins surrounded by ground pins.	Minimize EMI.
SYS-23	High	All PSYS use 3.3 V point-to-point UART links to communicate.	Common hardware interface between all active subsystems.
SYS-24	High	EPS, COM and CDHS shall use UART with 19200 baud, 8-bit words, 1 stop bit, no parity, no flow control.	Ground-communication is limited with 1200 bps uplink and 9600 bps downlink.
SYS-25	High	All PSYS use ICP for packet transfer and routing.	Common protocol between all active subsystems.
SYS-26	Medium	All PSYS should support in-orbit firmware updates.	In-orbit validation and comparison of algorithms.
SYS-27	High	None of the PSYS use integrated circuits in BGA packages.	Soldering quality is difficult to verify.
SYS-28	High	None of the PSYS use passives smaller than 0402.	Reduce risks during vibration, shock or ESD.
SYS-29	High	All PSYS use solder wire with lead.	Low eutectic melting temperature. Reduces risk of tin whiskers.

A.1 Structural requirements

Table 1: Table of structural requirements.

Id.	Pri.	Description	Rationale
STR-1	High	S/C dimensions: $10 \times 10 \times 11.35$ cm.	CubeSat standard, 1U.
STR-2	High	S/C mass < 1.33 kg.	CubeSat standard, 1U.
STR-3	High	AP and RBF must be on the same side.	CubeSat standard, accessibility for maintenance.
STR-4	High	RBF is removed after S/C is integrated into the POD.	CubeSat standard, enable deployment in orbit.
STR-5	High	RBF pins must be accessible from the access port region.	CubeSat standard, must remove RBF before launch.
STR-6	High	At least 75% of the rail will be in contact with the pod.	CubeSat standard.

Table 1: Table of structural requirements.

Id.	Pri.	Description	Rationale
STR-7	High	No components on S/C sides (including RBF) exceed 6.5 mm from the plane of the rails.	CubeSat standard.
STR-8	High	Aluminium 7075, 6061, 5005 and/or 5052 will be used for rails and structure.	CubeSat standard.
STR-9	High	Rails and standoff that are in contact with the POD rails shall be hard anodized.	CubeSat standard, prevents cold welding.
STR-10	High	Separation springs shall be used.	CubeSat standard, 1U. Ensures adequate separation of S/C.
STR-11	High	Separation springs will be centered on the end of the standoff.	CubeSat standard, 1U.
STR-12	High	Compressed separation springs shall be at or below the level of the standoff.	CubeSat standard, 1U.
STR-13	High	Actuated deployment switch will be at or below the level of the standoff.	CubeSat standard.
STR-14	High	S/C shall have $VentingArea > Volume/(50\,800\,\text{mm})$.	CubeSat standard.
STR-15	High	S/C center of mass < 2 cm of geometric center.	CubeSat standard, 1U.
STR-16	High	Width of rails ≥ 8.5 mm.	CubeSat standard.
STR-17	High	Rail surface roughness $< 1.6\,\mu$m.	CubeSat standard.
STR-18	High	Rail edges rounded to radius ≥ 1 mm.	CubeSat standard.
STR-19	High	Ends of rails have contact area $\geq 6.5 \times 6.5$ mm.	CubeSat standard.
STR-20	High	All parts remain attached to S/C during launch, ejection and operation.	CubeSat standard.
STR-21	High	Pyrotechnics are not allowed.	CubeSat standard.
STR-22	High	Withstands sine sweep $5\,\text{Hz} \ldots 2000\,\text{Hz}$ at up to $22.5\,g_{\text{peak}}$.	Vega launcher specifications.
STR-23	High	Withstands random vibration $20\,\text{Hz} \ldots 2000\,\text{Hz}$ at up to $22.5\,g_{\text{rms}}$.	Vega launcher specifications.
STR-24	High	Withstands shock $100\,\text{Hz} \ldots 1000\,\text{Hz}$ at up to 1410 g.	Vega launcher specifications.
STR-25	Low	Minimize the number of parts in the S/C frame.	Mass optimization.
STR-26	Medium	Minimize the usage of ferromagnetic materials.	Ferromagnetic materials cause S/C alignment to Earth's magnetic field and distort magnetic torquer output.

A.2 Electrical power requirements

Table 1: Table of electrical power system requirements.

Id.	Pri.	Description	Rationale
EPS-1	High	Electronics not be powered during launch.	CubeSat standard, avoid interference.

Table 1: Table of electrical power system requirements.

Id.	Pri.	Description	Rationale
EPS-2	High	S/C has at least 1 deployment switch.	CubeSat standard, requirement EPS-1.
EPS-3	High	S/C should have at least 2 deployment switches.	CubeSat standard, reliability.
EPS-4	High	Actuated deployment switch disconnects power system from powered functions (including RTC).	CubeSat standard, avoid interference.
EPS-5	High	While S/C is in the POD, deployment switch is always actuated.	CubeSat standard, avoid deployment in the POD.
EPS-6	High	If deployment switch toggles from actuated state and back, the deployment timers are reset.	CubeSat standard, reduce risk of deployment by mistake.
EPS-7	High	S/C has an RBF pin to cut all power during integration.	CubeSat standard, avoid deployment while inserting S/C into the POD.
EPS-8	High	Total capacity of the batteries $\leq$ 100 W h.	CubeSat standard.
EPS-9	High	Pre-launch diagnostics and battery charging performed with deployment switches depressed.	CubeSat standard, satellite is in the pod and access is limited to AP.
EPS-10	High	S/C shall incorporate battery protection and balancing for charging / discharging.	CubeSat standard, avoids unbalanced cell conditions.
EPS-11	High	Initiates antenna deployment $\geq$ 30 min after S/C deployment.	Cubesat standard, avoid tangling with other S/C.
EPS-12	High	Antenna deployment is performed 10 times with 30 s cycles.	Minimize probability of failure.
EPS-13	High	During an antenna deployment cycle, the burning wire is powered on for 15 s, then off for 15 s.	Let the wire cool down between attempts.
EPS-14	High	Start transmitting safe-mode beacon 10 min after antenna deployment.	Wait until the antenna oscillations have been dampened.
EPS-15	High	Transmit safe-mode beacon for at least 48 h with a 3 min interval.	International contribution from radio amateurs listening to the beacon.
EPS-16	High	Must not run initial start sequence when any of the RBF pins is attached.	Avoid antenna deployment during AIV.
EPS-17	High	Deployment sequence must not be initiated when connected to APD.	S/C must not deploy its antennas during pre-launch checks.
EPS-18	High	RF transmission is not used when connected to APD.	S/C must not transmit anything during pre-launch checks.
EPS-19	High	S/C hard-resets when left without ground communications for 12 h.	Automatically restore S/C to a safe state.
EPS-20	High	Able to power-cycle the S/C.	Recovery from SEL in EPS or COM.
EPS-21	High	Able to power on/off CDHS 3.3 V supply lines CDHS_A, CDHS_B.	Selection of CDHS MCU.
EPS-22	High	Able to power on/off CDHS 3.3 V supply line CDHS_BSW.	CDHS peripherals common to both MCUs.

Table 1: Table of electrical power system requirements.

Id.	Pri.	Description	Rationale
EPS-23	High	Current cut-off on CDHS_A, CDHS_B at $\geq 120\,\text{mA}$.	Protection against SEL in CDHS MCU.
EPS-24	High	Current cut-off on CDHS_BSW at $\geq 50\,\text{mA}$.	Protection against SEL in CDHS peripherals.
EPS-25	High	Must measure power consumption per supply line.	Beacon, housekeeping data and CDHS logging.
EPS-26	High	Measures current on CDHS_A, CDHS_B, CDHS_BSW (accuracy $\leq 1\,\text{mA}$).	Monitor radiation effects on CDHS components.
EPS-27	High	Able to power on/off ADCS 5 V supply line ADCS_5V.	Supply for ADCS sensors.
EPS-28	High	Current cut-off on ADCS_5V at $\geq 100\,\text{mA}$.	Protection against SEL in ADCS.
EPS-29	High	Supports TC for power-cycle and power on/off operations.	Power control from CDHS, manual power control from the ground.
EPS-30	High	Able to power on/off CAM 3.3 V supply line CAM_3V3.	Supply for camera.
EPS-31	High	Current cut-off on CAM_3V3 at $\geq 120\,\text{mA}$.	Protection against SEL in CAM.
EPS-32	High	Able to power on/off PL motor controller and ADC (3.3 V supply line PL_3V3).	Supply for motor controller, tether voltage, tether current and anode current measurements.
EPS-33	High	Able to power on/off PL motor (5 V supply line PL_5V).	Supply for reel motor.
EPS-34	High	Able to power on/off 12 V supply line PL_12V for the PL high voltage supply.	High voltage supply for the tether and e^- emitters.
EPS-35	High	Able to control the supply voltage of PL_12V by $\pm 10\%$.	Measure volt-ampere characteristics of e^- emitters.
EPS-36	High	Has dedicated UART for COM ICP.	Point to point links, to avoid inter-subsystem interference.
EPS-37	High	Had dedicated UART for CDHS ICP.	Point to point links, to avoid inter-subsystem interference.
EPS-38	Medium	Has dedicated UART for EPS debugging.	Direct control of the EPS with the APD when COM and CDHS are powered off.
EPS-39	High	Supports TC to control any regulator or power switch.	Manual control for unexpected work-arounds.
EPS-40	High	Supports TC to enable reel lock deployment for a specified amount of time.	EPS has the reel lock driver.
EPS-41	High	Supports TC to enable end-mass lock deployment for a specified amount of time.	EPS has the end-mass lock driver.
EPS-42	High	Supports TC to request current measurements.	EPS measures current consumption on each supply line.
EPS-43	High	Supports TC to request the states of power switches.	EPS has the power switches.
EPS-44	High	Collects and prepares data for the safe-mode beacon.	Only EPS and COM are powered on in safe mode.

Table 1: Table of electrical power system requirements.

Id.	Pri.	Description	Rationale
EPS-45	Medium	Should provide absolute time for other subsystems.	EPS has battery-backed RTC.
EPS-46	Medium	Provides TC for selecting CDHS MCU.	Avoid power switching on CDHS.
EPS-47	Medium	Provides TC for resetting CDHS MCU.	Avoid power switching on CDHS.
EPS-48	High	Supports in-orbit firmware updates.	Supports improvements, bug fixes.
EPS-49	High	Automatic rolls back to backup firmware image on fatal error.	Basic error recovery.
EPS-50	High	Has at least 1 backup firmware image.	Basic error recovery.
EPS-51	High	Firmware image CRC is verified before booting.	Avoid booting corrupt firmware.
EPS-52	High	Controls ADCS coils based on the received control signal.	Driving magnetic torquers from battery bus directly.
EPS-53	High	Manage shared COM PA.	COM transmits packets, EPS transmits CW beacon.
EPS-54	High	Supports TC for RTC synchronization.	Clock synchronization from the ground.
EPS-55	High	Provides RTC synchronization service for other systems.	Clock synchronization of CDHS, CAM.
EPS-56	High	Has a watchdog.	Recovery from infinite loops.

A.3 Attitude determination and control requirements

Table 1: Table of attitude determination and control requirements.

Id.	Pri.	Description	Rationale
ADCS-1	High	Detumble S/C from $360\,^\circ\,\mathrm{s}^{-1}$ to $\approx 1\,^\circ\,\mathrm{s}^{-1}$.	Restore safe operating conditions during spin-up controller tests.
ADCS-2	High	Spin-up S/C to $\leq 360\,^\circ\,\mathrm{s}^{-1}$.	Tether deployment.
ADCS-3	Medium	Align spin-axis to Earth's polar axis with pointing error $< 3°$.	Tether deployment. Maximise Coulomb drag, minimise Lorentz force on the tether.
ADCS-4	High	Spin axis must be perpendicular to the tether deployment direction. Deviation $< 10°$.	Tether deployment. Safe distance between tether and S/C frame.
ADCS-5	High	Determine attitude with accuracy $< 2°$.	Spin-axis alignment.
ADCS-6	High	Determine angular rate with accuracy $< 0.4\,^\circ\,\mathrm{s}^{-1}$.	Measure the E-Sail force.
ADCS-7	Medium	Point the camera at Estonia, $\pm 10°$.	Take images of Estonia.
ADCS-8	High	Attitude control with magnetic torquers.	Mass, volume, power budgets too low for propulsion or reaction wheels
ADCS-9	High	Has a sun sensor per S/C side.	Sun vector regardless of the illuminated side.
ADCS-10	Medium	Has at least 2 magnetometers.	Increase SNR by averaging.

Table 1: Table of attitude determination and control requirements.

Id.	Pri.	Description	Rationale
ADCS-11	Medium	Has at least 2 gyroscopic sensors.	Increase SNR by averaging.
ADCS-12	High	Interfaces analogue sun sensors on side panels.	Central ADC reduces overall power consumption of the system.
ADCS-13	High	Provides an SPI interface to sun sensor measurements for CDHS.	Not enough system bus pins for all the analogue signals.
ADCS-14	High	Consumes < 100 mA on ADCS_5V.	Power budget.
ADCS-15	High	Magnetic torquers active throughout most of the attitude control algorithm iteration.	Attitude control at high spin rates.
ADCS-16	High	Maintain enough delay between magnetometer measurements and the actuation of magnetic torquers.	Magnetic torquers saturate magnetometers.

A.4 Command and data handling requirements

Table 1: Table of command and data handling requirements.

Id.	Pri.	Description	Rationale
CDHS-1	High	PCB has cutouts for ADCS connectors.	Minimize distance between CDHS and ADCS PCBs.
CDHS-2	High	Consumes < 100 mA per supply line (CDHS_A, CDHS_B, CDHS_BSW).	Power budget.
CDHS-3	High	Has dedicated UART for EPS ICP link.	Point to point links, to avoid inter-subsystem interference.
CDHS-4	High	Has dedicated UART for COM ICP link.	Point to point links, to avoid inter-subsystem interference.
CDHS-5	High	Has dedicated UART for CAM ICP link.	Point to point links, to avoid inter-subsystem interference.
CDHS-6	High	Has at least two SPI peripherals for ADCS ADCs.	Sun sensor analogue measurements with redundancy.
CDHS-7	High	Has at least two I2C peripherals for ADCS magnetometers, gyroscopic sensors.	Magnetometer, gyroscopic sensor measurements with redundancy.
CDHS-8	High	At least 3x 3.3 V digital outputs to control PL motor direction and speed.	Tether deployment.
CDHS-9	High	Has a digital input to count PL motor pulses.	Feedback on tether deployment.
CDHS-10	High	At least 2x 3.3 V digital outputs to enable / disable PL electron emitters.	Electron emitters for positive mode.
CDHS-11	High	3.3 V digital output to enable / disable PL positive mode.	Measure E-Sail effect at +500 V potential.
CDHS-12	High	3.3 V digital output to enable / disable PL negative mode.	Measure E-Sail effect at -500 V potential.
CDHS-13	High	3.3 V digital output to connect / disconnect PL ground to S/C ground.	S/C body collects electrons in the PL negative mode.

Table 1: Table of command and data handling requirements.

Id.	Pri.	Description	Rationale
CDHS-14	High	Has SPI for PL ADC to measure tether voltage, current.	Measure tether voltage and current.
CDHS-15	High	Is able to activate CAM boot pins and reprogram its MCU.	CAM is only communicable through CDHS.
CDHS-16	Medium	Should have a dedicated UART for AP.	Improves debugging and monitoring capabilities on integrated S/C.
CDHS-17	High	Gathers housekeeping data from S/C subsystems.	OBCS is the only S/C subsystem connected to all other subsystems
CDHS-18	High	Periodically compiles housekeeping data for EPS beacon.	EPS operates COM to transmit beacon.
CDHS-19	High	Controls and monitors the payload.	Payloads are connected to the OBCS.
CDHS-20	High	Receives and distributes commands.	OBCS is the only S/C subsystem connected to all other subsystems.
CDHS-21	High	Executes commands and sends back responses.	S/C must be operable
CDHS-22	High	Automatically synchronizes time with EPS.	Only EPS has a battery-backed RTC.
CDHS-23	Medium	Provides TC to start time synchronization with EPS.	Resynchronization before high-accuracy experiments.
CDHS-24	High	Absolute time with accuracy $< \pm 1\,\mathrm{s}$.	Attitude determination orbital models.
CDHS-25	High	Runs ADCS algorithms.	OBCS has the highest computational power.
CDHS-26	High	Provides non-volatile storage for ADCS configuration tables.	ADCS configuration not lost on power loss or reboot.
CDHS-27	High	Provides non-volatile storage for ADCS logs ($> 4\,\mathrm{MiB}$, about $6\,\mathrm{KiB\,s^{-1}}$).	Single orbit of ADCS sensor measurements, attitude quaternion and error at 10 Hz.
CDHS-28	High	Provides non-volatile storage for PL logs ($> 1.4\,\mathrm{MiB}$, about $20\,\mathrm{B\,s^{-1}}$).	Single day of tether voltage, current, and e-gun current measurements at 1 Hz.
CDHS-29	High	Supports command scheduling with accuracy $\leq 10\,\mathrm{ms}$.	Charging tether synchronously to S/C spin.
CDHS-30	Medium	Performs lossless data compression.	Reduce measurement logs before downlink.
CDHS-31	High	Capable of measuring ADCS sun sensors at $\leq 10\,\mathrm{Hz}$.	Needed for attitude determination at high spin rates.
CDHS-32	High	Measures ADCS gyroscopic sensors at $\geq 1\,\mathrm{Hz}$.	Magnetic torquers accelerate up to $0.1\,^\circ\,\mathrm{s^{-2}}$.
CDHS-33	High	Measures ADCS magnetometers at $\leq 10\,\mathrm{Hz}$.	Needed for attitude determination in eclipse.
CDHS-34	High	Sends ADCS coil control signals (PWM, duration) to EPS.	Control of magnetic torquers.
CDHS-35	High	Able to run ADCS Kalman filter at up to 10 Hz.	Optimal value for spin-up and E-Sail measurements.

Table 1: Table of command and data handling requirements.

Id.	Pri.	Description	Rationale
CDHS-36	Medium	Provices non-volatile storage for 10 CAM images.	CAM has volatile storage for 4 images.
CDHS-37	High	Has a watchdog.	Recovery from infinite loops.
CDHS-38	High	Controls payload reel motor direction.	Needed during Assembly, Integration, Verification (AIV).
CDHS-39	High	Control payload reel motor speed.	Needed during AIV.
CDHS-40	High	Maintains non-volatile reel motor position.	Reel motor controller does not measure reel position
CDHS-41	High	Able to individually enable / disable electron emitters.	Cold rednudant emitters for positive tether mode.
CDHS-42	High	Supports partial file downlink, accounting for packet loss.	Downloading of measurement logs.
CDHS-43	High	Supports partial file uplink, accounting for packet loss.	Firmware updates.
CDHS-44	High	Provides TC for file write.	Firmware updates.
CDHS-45	High	Provides TC for file read.	Downloading measurement logs.
CDHS-46	Medium	Provides TC for raw memory read.	In-orbit debugging, forwards compatibility.
CDHS-47	Medium	Provides TC for raw memory write.	In-orbit debugging, forwards compatibility.
CDHS-48	High	Provides TC for ADCS raw sensor measurements.	Validation of ADCS algorithms.
CDHS-49	High	Provides TC for attitude parameters.	Validation of ADCS algorithms.
CDHS-50	High	Able to measure MCU temperature ($\pm 5\,^{\circ}$C).	Monitor radiation effects on MCU.
CDHS-51	Medium	Able to measure RTC temperature ($\pm 3\,^{\circ}$C).	Reference temperature for monitoring radiation effects on MCU.
CDHS-52	High	Supports 64-bit floating-point arithmetics.	ADCS algorithms use 32-bit and 64-bit floating-point arithmetics.
CDHS-53	High	Provides TC for config read.	Get active configuration.
CDHS-54	High	Provides TC for config write.	Change active configuration.
CDHS-55	High	Provides TC for config load.	Reset configuration.
CDHS-56	High	Provides TC for config save.	Save active configuration.
CDHS-57	High	Provides TC for TLE management.	ADCS orbital models.

A.5 Other requirements

Table 1: Table of other requirements.

Id.	Pri.	Description	Rationale
COM-1	High	Receives TC from GS over the radio.	Communication with the satellite in orbit.
COM-2	High	Forwards TC from GS to CDHS or EPS.	Ground-communication with any active system.

Table 1: Table of other requirements.

Id.	Pri.	Description	Rationale
COM-3	High	Receives TM from CDHS or EPS and forwards to GS.	Ground-communication with any active system.
COM-4	High	Frequency coordination is started $\leq$ 0.5 y before launch.	Frequency coordination may take several years.
COM-5	High	Frequency Shift Keying (FSK) uplink at 145 MHz . . . 146 MHz.	Requirement COM-1.
COM-6	High	CW beacon and FSK downlink at 435 MHz . . . 438 MHz.	Requirement COM-3.
COM-7	High	RF transmission power at antenna input < 1.5 W.	CubeSat standard for single RF inhibit.
COM-8	High	S/C has RF inhibit (TC to permanently switch off transmitter).	CubeSat standard, IARU regulations to avoid interference.
COM-9	High	S/C does not transmit before 45 min after deployment from POD.	CubeSat standard.
COM-10	High	Supports AX.25 for packet encapsulation.	Standard among radio amateurs.
COM-11	High	Amateur radio callsign based on GS callsign, with suffix "/S".	Estonian law for formulating callsigns.
COM-12	High	Provides TC for requesting COM housekeeping data.	Monitor in-orbit degradation of COM.
COM-13	High	PCB is $94 \times 92 \times 15$ mm.	S/C volume budget.
CAM-1	High	Angular resolution of $\leq 275''$.	Validate tether deployment by imaging the End Mass.
CAM-2	High	Radiometric sensitivity for end-mass detection.	Validate tether deployment by imaging the End Mass.
CAM-3	High	Field of view of $\geq 45°$.	Monitor tether deployment and photograph Estonia.
CAM-4	High	Capability to download unprocessed sensor data.	Raw images for post-processing.
CAM-5	Medium	On-board storage for more than 1 image.	Histogram-based filtering of images (nice to have).
CAM-6	High	Depth of field from 1 to ∞ m.	Imaging of tether and Earth.
CAM-7	Medium	Fits in $25 \times 94 \times 20\,\text{mm}^3$ on the PL high voltage supply PCB.	Close to tether and center of mass.
PL-M-1	High	Rotate the motor on command.	Enable controlled tether deployment.
PL-M-2	High	Height of the PCB components in area $65 \times 39\,\text{mm}^2$ in the middle of the PCB bottom side must be < 2 mm.	Reserved for EPS batteries.
PL-M-3	High	No components in the middle of the PCB top side.	Reserved for tether reel.
PL-M-4	High	Mounting holes and connectors for tether reel and motor, according to ESTCube-RYHB-ES-EP-001.	Payload specifications.
PL-M-5	High	Motor controller must generate unipolar sawtooth at 550 Hz . . . 590 Hz, with an amplitude of ≤ 35 V.	Motor specifications.
PL-M-6	High	The rising and falling edge durations must differ by at least 10×.	Motor specifications.

Table 1: Table of other requirements.

Id.	Pri.	Description	Rationale
PL-M-7	High	Motor direction must be controllable during AIV.	Reel-in of the tether during assembly.
PL-M-8	Medium	Motor direction should be fixed for flight.	Reduce risk of S/C operator error.
PL-M-9	High	Motor controller must consume $< 2\,\mathrm{W}$.	S/C power budget.
PL-M-10	High	Motor is controlled via 3.3 V digital signals.	Simple interface between CDHS and motor controller.
PL-M-11	High	Motor controller may be supplied with 3.3 V, 5 V, and / or 12 V.	EPS payload interface.
PL-HV-1	High	Generate $\pm 500\,\mathrm{V}$ $\pm 5\%$ to charge tether and power e^- emitters.	Charge the tether to positive high potential.
PL-HV-2	Medium	Change polarity of the high voltage supply on command.	Support positive and negative high voltage modes.
PL-HV-3	High	Measure tether voltage.	Measure E-sail effect, monitor degradation of high voltage supply.
PL-HV-4	High	Measure tether current.	Measure E-sail effect.
PL-HV-5	High	Measure e^- emitter anode current.	Characterise e^- emitters.
PL-HV-6	High	Control each e^- emitter individually.	Characterise each e^- emitter separately; cold redundancy.
MCS-1	High	Provide public web interface for radio amateurs to enter beacon data.	

Appendix B
System bus pinout

Tables 3 and 4 list the electrical pinout of the ESTCube-1 system bus connector.

Each signal (or pin) in the system bus connector is listed as a cell of two rows as shown in Table 2. There the first row lists the signal name and indicates the signal type with formatting. Table 1 shows the relation between the signal type and its formatting in the system bus pinout tables. Regular digital signals are shown in regular font, power supply lines are shown in bold and data lines (potentially high frequency) are shown in red. The background colour of each cell indicates the voltage level: light blue corresponds to 3.3 V, beige to ≈ 4.2 V, green to 5 V, dark blue to 12 V and grey to ground. Analogue signals are indicated by a yellow background.

Table 1: Legend for the system bus connector signal types.

Style	Description
XXX	3.3 V digital signal
XXX	3.3 V supply line
XXX	Main power bus supply line
XXX	5 V digital signal
XXX	5 V supply line
XXX	12 V supply line
	Ground
XXX	3.3 V analog signal
XXX	High current signal (> 30 mA)
XXX	Low frequency signal
XXX	High frequency signal (> 100 kHz)
xxx	Signal group

Table 2: Legend for a single system bus connector pin.

Pin column number

Pin row number

SIGNAL_NAME
SIGNAL_GROUP

Table 3: ESTCube-1 system bus connector pinout, first 15 rows.

	A	B	C	D
1	RBF1	RBF2	RBF3	
	EPS_EXT	EPS_EXT	EPS_EXT	EPS_EXT
2	RBF1_2	RBF2_2	RBF3_2	EXT
	EPS_EXT	EPS_EXT	EPS_EXT	EPS_EXT
3	CDHS_HBEAT	COM_BCN_DISABLE		ADCS_5V
	CDHS	COM	ADCS	ADCS
4	CAM_HBEAT		COM_PA_ENABLE	COM_5V
	CAM	COM	COM	COM
5		COM_HBEAT	CAM_SHOT	
	COM	COM	CAM	COM
6	COM_BCN_KEYER_OUT			CAM_3V3
	COM	COM	CAM	CAM
7		CDHS_FIRM	CDHS_BOOT0	COM_3V3
	CDHS	CDHS	COM	COM
8	COM_CDHS_RX		CDHS_NRST	
	COM	CDHS	COM	COM
9	COM_CDHS_TX	COM_EPS_TX		CDHS_A
	COM	COM	CDHS	CDHS
10		COM_EPS_RX	EPS_CDHS_RX	
	COM	COM	EPS	CDHS
11	COM_SCL		EPS_CDHS_TX	CAM_TX
	COM	COM	EPS	CAM
12	COM_SDA	ADCS_I2C1_SDA		CAM_RX
	COM	ADCS	EPS	CAM
13		ADCS_I2C1_SCL	ADCS_I2C0_SCL	
	COM	ADCS	ADCS	CAM
14	ADCS_SPI0_MISO		ADCS_I2C0_SDA	ADCS_SPI1_CS0
	ADCS	ADCS	ADCS	ADCS
15	ADCS_SPI0_MOSI	ADCS_SPI1_MOSI		ADCS_SPI1_CS1
	ADCS	ADCS	ADCS	ADCS

Table 4: ESTCube-1 system bus connector pinout, last 15 rows.

	A	B	C	D
16	ADCS_SPI0_SCK	ADCS_SPI1_SCK	ADCS_SPI0_CS0	ADCS_SPI1_CS2
	ADCS	ADCS	ADCS	ADCS
17		ADCS_SPI1_MISO	ADCS_SPI0_CS1	
	ADCS	ADCS	ADCS	ADCS
18	PL_MCOUNTER		ADCS_SPI0_CS2	
	PL	ADCS	ADCS	ADCS
19		CDHS_A_EXT		**CDHS_B**
		EPS_EXT	CDHS	CDHS
20		CDHS_B_EXT		**CDHS_BSW**
		EPS_EXT	CDHS	CDHS
21				**PL_3V3**
		EPS_EXT	PL	PL
22				**PL_5V**
			PL	PL
23				**PL_12V**
			PL	PL
24			CDHS_DAC1	
	PL	PL	CDHS	PL
25	PL_ADC_CS	PL_GNDSW		GUN1
	PL	PL	PL	PL
26			GUN3	GUN2
	PL	PL	PL	PL
27	**PL_RLOCK**	NEG_HV_SUP	GUN4	
	PL	PL	PL	PL
28	**PL_LLOCK**	POS_HV_SUP		**PL_RMOTOR0**
	PL	PL	PL	PL
29				**PL_RMOTOR1**
	PL	PL	PL	PL
30	**PL_RMOTOR5**	**PL_RMOTOR4**	**PL_RMOTOR3**	**PL_RMOTOR2**
	PL	PL	PL	PL

Appendix C
In-orbit firmware updates of the command and data handling system

Table 1 lists the firmware updates performed on the CDHS flight model in order to introduce new features, to improve software stability or to improve system performance. All firmware updates except for the first were performed with the spacecraft in-orbit.

The version column lists the version numbers with major version indicated in the most significant byte and automatically incremented build count in the least significant byte.

Table 1: List of CDHS firmware versions.

Version	**Upload date**	**Changelog**
0x120A	April 27, 2013	Pre-launch firmware with basic functionality: • In-orbit firmware updates. • Basic configuration tables. • Basic telecommand scheduling. • On-board logging of housekeeping data.
0x1211	June 8, 2013	Additional features: • On-board logging of any telecommands and telemetry. • Configuration tables for ADCS. • On-board RTC synchronization with EPS. • Telemetry buffering. • Packet beacon. • Compensation of measurement latency for ADCS sun sensors. • Telecommand for repetitive scheduling of commands. • Support for multiple telecommands per packet. • Fallback configuration on 6 consecutive reboots without radio contact.
0x1214	June 24, 2013	Improved stability and additional features: • Watchdog resets to secure against infinite loops. • Scheduling of CAM imaging trigger. • Post factum updates of error log timestamps. • Non-volatile reboot count.

Table 1: List of CDHS firmware versions.

Version	Upload date	Changelog
0x130E	August 19, 2013	Improved stability and additional features: • Improved stability of date-time scheduling. • Temperature compensation for ADCS angular rate measurements. • ADCS magnetic torquer control. • Multiple storage systems for the error log. • Configurable baud rate with CAM. • Telecommands for listing, creating and removing on-board files.
0x1404	September 14, 2013	Improved stability and additional features: • Improved the performance of ICP. • Improved ADCS drivers. • Improved the stability of telemetry buffering and calibration. • Non-volatile storage of stack overflow and memory allocation failure events. • Unit conversion and averaging of ADCS measurements of angular rate. • Telecommand for FreeRTOS performance measurements.
0x1500	December 21, 2013	Improved stability and additional features: • Logging of watchdog resets. • Non-volatile storage of watchdog reboot events. • Reduced code footprint (simplified date-time scheduler and removed unit tests). • On-board scripting with Pawn. • Telecommand to trigger magnetometer self-test mode. • Temperature compensation for magnetometer measurements. • Low-level filtering of sun sensors. Temperature measurements from sun sensor ADCs. • Automatic reinitialization of magnetometers and gyroscopic sensors. • Improved ADCS sensor low-level filters. • Telecommand to request for the output of ADCS sensor filters. • Reduced the average current consumption of the ADCS. • Look-up table to increase the performance of ADCS trigonometry. • Telemetry buffering for CAM image data.
0x1506	January 16, 2014	Improved stability and additional features: • Improved stability of ADCS sensor measurements. • Telecommand to request for uncalibrated sensor measurements. • Improved stability of telemetry buffering.

Table 1: List of CDHS firmware versions.

Version	Upload date	Changelog
0x1511	January 27, 2014	Improved the stability of the firmware and performed basic optimization: • Improved stability of ADCS sensor measurements. • Reduced firmware flash footprint. • Improved stability of command date-time scheduling.
0x1611	March 1, 2014	Improved stability, performance and integrated the first attitude control algorithms: • Improved stability of ADCS sensor measurements and triggering of magnetic torquers. • Integrated B-dot and spin-up controllers. • Improved the performance of the command scheduler.
0x1706	March 10, 2014	Improved stability and integrated a pointing control algorithm: • Improved stability of ADCS sensor measurements. • Resolved an issue in the normalization of Kalman filter output. • Resolved an issue with unit conversion in the low-level filter of gyroscopic sensors. • Integrated pointing controller. • Implemented basic support for compensating against the distortions in the magnetic torquer output.
0x1804	March 18, 2014	Improved stability: • Improved stability of ADCS sensor measurements. • Added support for offsets to magnetic torquer correction.
0x180A	March 29, 2014	Improved stability: • Improved stability of watchdog and on-board scripting. • Removed dedicated mission log (replaced with universal non-volatile storage of telemetry).
0x191A	May 10, 2014	Improved stability and a spin-up controller for arbitrary axis: • Improved timing of ADCS sensor measurements, algorithms and magnetic torquer actuation. • Implemented a mission controller for launch-, reel locks and electron emitters. • Improved stability of magnetic torquer control. • Telecommand to request for an estimate of the orbital position of the spacecraft. • Improved stability of on-board memory management and scripting. • Added support for firmware upgrades from the fallback configuration. • Integrated a spin-up controller for arbitrary axis.
0x191B	May 12, 2014	Clipped magnetic torquer control signals to the maximum value that is supported by EPS.

Table 1: List of CDHS firmware versions.

Version	**Upload date**	**Changelog**
0x1A04	June 12, 2014	Improved stability: • Automatic detection of whether ADCS is powered. Magnetic torquers are only actuated when ADCS is powered. • More robust timing between the measurement of ADCS magnetometers and the actuation of magnetic torquers.
0x1A07	July 30, 2014	Improved stability and resolved an issue with the extrapolation of sun sensor measurements.
0x1A0F	August 16, 2014	Improved stability and trustworthiness of sensor measurements: • Implemented on-board estimation of the correction matrix to compensate for the distortions in magnetic torquer output. • Implemented averaging for on-board temperature measurements that are used for temperature compensation.
0x1B04	August 24, 2014	Improved stability: • Improved stability of attitude control algorithms. • Telecommand to reinitialize the Kalman filter. • Automatic reinitialization of the Kalman filter when started in the eclipse. • Telecommands to start, swap or restart attitude determination and / or control algorithms. • Implemented desaturation for magnetic torquers. • Disturbance torque is now taken into account in the on-board attitude estimates.
0x1B08	August 26, 2014	Improved the accuracy of magnetic field estimates for the Kalman filter. Resolved an issue with the extrapolation of ADCS sensor measurements.
0x1C19	January 11, 2015	Implemented payload high voltage control and optimized the firmware, as well as introduced new features: • On-board data compression with QuickLZ. • Image transfer from CAM to on-board flash memory.
0x1C1A	January 25, 2014	Resolved an issue with the enabling of the PL3V3 line and improved the flexibility of the payload high voltage control.

Appendix D
On-board configuration tables

D.1 Configuration for command and data handling

Table 1 lists CDHS configuration parameters together with their addresses and sizes. There are three address columns: word index, half-word index and byte index. The configuration table is split into 75 words, where each word is divided further into either two half-words or four bytes. Parameters can be of the following types: 64-bit double `double`, 32-bit float `float`, 32-bit unsigned integer `uint32`, 32-bit signed integer `int32`, 16-bit unsigned integer `uint16`, 16-bit signed integer `int16`, 8-bit unsigned integer `uint8` or an 8-bit signed integer `int8`. To avoid the storage of type descriptors in the configuration table, a separate telecommand was reserved for reading or writing each parameter type.

When intervals or periods are either assigned a negative value or zero, then the periodic operation is disabled until a value is assigned that is large enough. The value `0xE57C00B1` is used as a magic placeholder, to avoid long sequences of consecutive 0 or 1 bits.

A minimum stack margin of 128 words is automatically added to all stack margins in the configuration table.

Floating-point vector types are indicated with `vecNf` where N corresponds to the vector dimensions. Integer vector types are indicated with `vecNi`, accordingly.

For brevity, the original spin controller for the Z axis will be called "Spin-Z", whereas the new spin controller for a configurable spin axis will be called "Spin-Arb".

Table 1: CDHS configuration table.

Address			Type	Name	Description	Default
0	0	0	uint32	`log_to_fram`	Store error log in SRAM (0) or FRAM (1).	1
1	0	0	uint32	`adcs_task_priority`	Priority of the task for ADCS algorithms.	2
2	0	0	uint32	`adcs_task_enabled`	ADCS task enabled (1) or disabled (0).	0
3	0	0	uint8	`adcs_estimate`	Attitude determination modes: none (0); sensors only (2); sensors with Sun model, SGP4, IGRF, Kalman filter (1); all the former with pointing (3).	0

Table 1: CDHS configuration table.

Address			Type	Name	Description	Default
3	0	1	uint8	adcs_controller	Attitude control modes: none (0); B-Dot (1); Spin-Z (2); Pointing (3); E-sail experiment (4); Constant magnetorquers (5); Spin-Arb (6); Test (7).	0
3	0	2	uint8	eps_coil_trigger_delay	Number of milliseconds to delay between setcoils2 and heartbeat trigger.	20
3	0	3	uint8	eps_silence_delay	EPS setcoils execution delay in milliseconds.	10
4	0	0	int32	beacon_period	Period for beacon transmission, in milliseconds.	-1
5	0	0	int32	reformat	Index of the file system to reformat on startup.	-1
6	0	0	int32	house_period	Period for collecting housekeeping data, in milliseconds.	-1
7	0	0	uint32	sch_task_period	Scheduler task idle delay, in milliseconds.	10
8	0	0	uint32	icp_task_period	ICP task idle delay, in milliseconds.	10
9	0	0	uint32	statistx_period	Period for saving on-board statistics, in milliseconds.	300000
10	0	0	uint32	scr_overlay_size	Size of script overlay pool, in bytes (should be word-aligned).	2048
11	0	0	uint32	sch_in_ram	Whether date-time scheduled commands are stored in RAM (1) instead of FRAM (0).	1
12	0	0	uint32	math_flags	Enable (1) or disable (0) look-up tables for trigonometry.	0
13	0	0	uint32	system_clock	Desired MCU clock frequency in MHz.	32
14	0	0	uint32	icp_tx_queue_size	Number of bytes to reserve for the queue of ICP packets to be transmitted. Based on tests, must be greater than 512.	1024
15	0	0	uint32	icp_num_sending_attempts	Number of tries for each packet.	1
16	0	0	uint32	icp_window_size	Window size for ICP Go-Back-N ARQ data protocol.	8
17	0	0	uint32	icp_update_packet_limit	Maximum number of packets processed per update.	8
18	0	0	int16	icp_resync_threshold	Number of "packet not delivered errors" before an ICP resync is scheduled or -1 to never resync due to packet errors.	-1

Table 1: CDHS configuration table.

Address			Type	Name	Description	Default
18	1	0	int16	`eps_silence_threshold`	Number of "packet not delivered errors" with EPS before a temporary ICP silence is triggered for EPS.	20
19	0	0	uint32	`itable_version`	Version of the firmware that stored this table, for potential incompatibility between versions.	-
20	0	0	uint32	`fwimg_pagemap_in_ram`	Firmware upload: store pagemap in FRAM (0) or in SRAM (1).	0
21	0	0	uint32	`mag_setup`	Magnetometer configuration flags.	
22	0	0	uint32	`gyro_setup`	Configuration flags for the gyroscopic sensors.	
23	0	0	uint32	`sync_by_rtc_period`	Interval for synchronising MCU time to the RTC time, to mitigate potential clock drift.	60000
24	0	0	uint32	`enable_beacon`		
25	0	0	uint32	`rts_timeout`	Timeout in centi-seconds for waiting a Ready-To-Send packet from COM.	20
26	0	0	uint32	`adcs_gyro_task_delay`	ADCS gyroscopic sensor task idle delay, in milliseconds.	300
27	0	0	uint32	`sch_dt_timer_threshold`	Timestamp difference threshold for assigning date-time commands to RTOS timers.	30
28	0	0	uint32	`sch_clr_on_startup`	Flags for clearing scheduler queues on startup (a safe default, just in case).	1
29	0	0	uint32	`packet_beacon_tmbuf`	Enable (1) or disable (0) telemetry buffering of packet beacon.	0
30	0	0	int32	`iwdog_period`	Watchdog timer reload value, -1 to disable.	0xFFF
31	0	0	int32	`pbeacon_period`	Packet beacon period, in milliseconds.	-1
32	0	0	uint8	`spifl_order0`	Flash file system index to assign to SPI Flash 1.	0
...	...	...	uint8	...	Flash file system index to assign to SPI Flash N.	N-1
33	0	0	uint16	`startup_flags0`	Startup flags for firmware image slot 0. Combination of fallback (1), MCU sleep on idle (2), rough MCU sleep on idle (4), no communication with EPS (8).	2
33	1	0	uint16	`startup_flags1`	Startup flags for firmware image slot 1. Combination of fallback (1), MCU sleep on idle (2), rough MCU sleep on idle (4), no communication with EPS (8).	2
34	0	0	uint32	`cam_uart_baud`	UART baud rate with CAM.	19200
35	0	0	int8	`spif_order0`	FRAM file system index to assign to SPI FRAM 1.	0

Table 1: CDHS configuration table.

Address			Type	Name	Description	Default
...	...	...	int8	...	FRAM file system index to assign to SPI FRAM N.	N-1
37	0	0	uint32	`sch_dt_xqt_missed`	Enable (1) or disable (0) execution of missed date-time commands.	1
38	0	0	int8	`i2c1_port_speed`	I^2C 1 port speed in multiples of 10 kHz.	40
...	...	...	int8	...	I^2C N port speed in multiples of 10 kHz.	40
39	0	0	int8	`spi1_port_speed`	SPI 1 port speed in MHz or 0 to let device drivers decide.	0
...	...	...	int8	...	SPI N port speed in MHz or 0 to let device drivers decide.	0
40	0	0	int32	`eps_guardian_period`	EPS guardian state polling period in seconds.	600
41	0	0	uint32	`reserved`	Reserved	-1
42	0	0	int32	`adcs_gyro_autosleep_delay`	Number of milliseconds between a gyro power management transaction and gyro measurements, or -1 to disable gyro power management.	-1
43	0	0	uint32	`reserved`	Reserved	-1
44	0	0	uint32	`log_flags`	Filter for error log, combination of bootloader messages (1), ICP errors (2), command scheduler messages (4), I^2C errors (8), ADCS sensors (16).	0xFFFFFFE6
45	0	0	int32	`user_data0`	An argument for on-board scripts.	0xE57C00B1
...	...	...	int32	...	An argument for on-board scripts.	0xE57C00B1
55	0	0	int8	`adcs_gyro_reset_delay`	Delay between a gyro reset and any follow-up transactions, in milliseconds.	10
55	0	1	uint8	`adcs_gyro_setup_delay`	Delay between gyro setup transactions, in milliseconds.	5
55	0	2	uint8	`adcs_mag_setup_delay`	Delay between magnetometer setup transactions, in milliseconds.	5
55	0	3	uint8	`adcs_gyro_reset_threshold`	Number of erroneous measurements before the gyro is hard-reset and reinitialized.	10
56	0	0	uint8	`adcs_mag_reset_threshold`	Number of erroneous measurements before the magnetometer is reinitialized.	10
56	0	1	uint8	`adcs_gyro_i2c_timeout`	I^2C timeout for gyro write-read transactions, in milliseconds.	40
56	0	2	uint8	`adcs_mag_i2c_timeout`	I^2C timeout for magnetometer write-read transactions, in milliseconds.	40
56	0	3	uint8	`adcs_dyn_R`	Disable (0) or enable dynamic covariance updates for sun sensors (1), gyroscopic sensors (2), both (3).	3

Table 1: CDHS configuration table.

Address			Type	Name	Description	Default
57	0	0	uint32	`adcs_mag_filter_flags`	Flags for enabling parts of the magnetometer filtering code, for debugging.	0xFFFFFFFF
58	0	0	int16	`adcs_gyro_task_stack`	Number of 32-bit words to reserve for the stack of the gyro task.	90
...	...	...	int16	`reserved`	Reserved	-1
59	1	0	int16	`adcs_flags`	Flags for the ADCS task, combination of the following: stop the task when ADCS power is cut (1), stop logging when ADCS power is cut (2), feed raw (unfiltered) angular rate to attitude controllers (4), feed raw (unfiltered) magnetic field measurements to attitude controllers (8), extrapolate sensor measurements based on angular rate from Kalman filter output (16), add angular rate bias to Kalman filter output (32), add magnetic field bias to Kalman filter output (64), reverse magnetic field bias (128).	15
60	0	0	uint16	`i2c_stack_size`	Number of 32-bit words to reserve for the stack of the I^2C daemon.	
60	0	2	uint8	`i2c_queue_len`	Length of the I^2C transaction queue.	
60	0	3	int8	`i2c_priority`	Priority of the I^2C daemon task.	2
61	0	0	uint8	`tmb_fs_type`	File system type for the telemetry buffer, either FRAM (0) or Flash (1).	0
61	0	1	uint8	`tmb_fs_index`	File system index for the telemetry buffer.	2
61	0	2	uint8	`tmb_fname`	File name (file index) for the telemetry buffer.	1
61	0	3	uint8	`eps_pl_hv_delay`	Delay between the TC to EPS for switching HV supply lines, in seconds.	2
62	0	0	uint8	`coil_dir0`	Direction of the magnetic torquer on the X axis, 0 for positive, 1 for negative.	1
62	0	1	uint8	`coil_dir1`	Direction of the magnetic torquer on the Y axis, 0 for positive, 1 for negative.	0
62	0	2	uint8	`coil_dir2`	Direction of the magnetic torquer on the Z axis, 0 for positive, 1 for negative.	1
62	0	3	uint8	`reserved`	Reserved	0
63	0	0	uint8	`coil_order0`	Index of the magnetic torquer on the X axis.	0
63	0	1	uint8	`coil_order1`	Index of the magnetic torquer on the Y axis.	1
63	0	2	uint8	`coil_order2`	Index of the magnetic torquer on the Z axis.	2
63	0	3	uint8	`reserved`	Reserved	0

Table 1: CDHS configuration table.

Address			Type	Name	Description	Default
64	0	0	uint16	`icp_op_queue_len`	Maximum number of operations waiting for the ICP task.	20
64	1	0	uint16	`reserved`	Reserved	0
65	0	0	uint32	`icp_task_stack`	Number of 32-bit words of stack to reserve for the ICP task.	360
66	0	0	float	`adcs_coil_timeout_unit`	Time unit for EPS setcoils command, milliseconds / value.	1.0
67	0	0	float	`adc_temp_weight`	Weight for the moving average of ADC temperature.	2.0
68	0	0	uint32	`adc_temp_period`	Interval for updating ADC temperature, in deci-seconds.	30
69	0	0	uint32	`pl_mode`	Payload mode while the experiment controller is running: high-voltage and motor disabled (0), positive tether mode (1), negative tether mode (2), negative tether mode with alternative ground (3), high-voltage off but motor enabled (4).	1
...	...	...	...	`reserved`	Reserved	
72	1	0	uint16	`eps_pl_flags`	Enable (1) or disable (0) ICP forwarding for EPS commands that involve the switching of payload supply lines.	1
73	0	0	uint8	`uart_task_priority`	Priority of the UART driver task.	2
73	0	1	uint8	`icp_task_priority`	Priority of the ICP task.	2
73	0	2	uint8	`sch_task_priority`	Priority of the command scheduler task.	4
73	0	3	uint8	`cam_fetch_flags`	Flags for fetching images from CAM: verify response addresses (1), verify response lengths (2), verify both (3).	3
74	0	0	uint16	`cam_fetch_img_timeout`	Timeout for CAM image requests, in milliseconds.	300
74	0	1	uint16	`cam_fetch_img_period`	Interval for CAM image requests, in milliseconds.	100

D.2 Configuration table for attitude determination and control

The parameters in the ADCS configuration table have been collected from ADCS libraries, none of which were developed by the author (except for magnetometer filtering). However, the service for runtime updates of these parameters was provided by the CDHS. As merely an example of the ADCS parameters, the table is incomplete.

Table 1: ADCS configuration table.

Addresses	Type	Name	Description
100	float	coil_margin	Safety margin (percentage) for calculating magnetic torquer timeouts.
...	...	...	...
111 - 113	vec3f	test_control_output	The magnetic output the test controller will request from the system.
114	float	gyro_calibration_constant	Coefficient for converting the output of the gyroscopic sensors from ADU into degrees per second.
115	float	g_gyro_filter_error_margin	Maximum difference between measurements.
116	float	gyro_max_consecutive_err	Maximum number of consecutive erroneous measurements that can occur without a filter reset.
117	float	gyro_filter_errorchecking_frequency	
118 - 123	vec6i	l_gyro_0_loc	Zero-biases of the gyroscopic sensors in ADU.
124 - 147	vec24f	gyro_temp_offset	Configurable linear temperature coefficients for gyros.
148 - 171	vec24f	gyro_temp_gain	Configurable linear temperature coefficients for gyros.
172 - 174	vec3i	mag_biases	Magnetometer zero-biases in ADU.
175 - 186	vec12f	mag_temp_linear	Slope of magnetometer temperature coefficient vs. temperature.
187 - 198	vec12f	mag_temp_offset_linear	Linear temperature-dependent offsets on magnetometer measurements.
199 - 200	vec2f	mag_total_weight	Importance of individual magnetometers in calculations.
201	float	mag_max_diff	Maximum absolute difference between 2 consecutive measurements.
202	float	mag_max_time_diff	Maximum allowed time difference between 2 consecutive measurements (that is, maximum time delta for extrapolation).
203	float	mag_filter_reset_threshold	Number of consecutive erroneous measurements that cause a filter reset.
204	float	mag_weight_expected	Weight of the expected magnetometer measurements.
...	...	...	...
214	float	sv_eclipse_boundary	ADU threshold for shadowed sensor.
215	float	sv_fov_boundary	Sun sensor field of view in radians.
...	...	...	...
226 - 228	vec3f	coilOutputXM	Coefficients for -X magnetic torquer output calculation w.r.t. max coil output.
229 - 231	vec3f	coilOutputXP	Coefficients for +X magnetic torquer output calculation w.r.t. max coil output.
232 - 234	vec3f	coilOutputYM	Coefficients for -Y magnetic torquer output calculation w.r.t. max coil output.

Table 1: ADCS configuration table.

Addresses	Type	Name	Description
235 - 237	vec3f	coilOutputYP	Coefficients for +Y magnetic torquer output calculation w.r.t. max coil output.
238 - 240	vec3f	coilOutputZM	Coefficients for -Z magnetic torquer output calculation w.r.t. max coil output.
241 - 243	vec3f	coilOutputZP	Coefficients for +Z magnetic torquer output calculation w.r.t. max coil output.
244	uint32	coil_selection	An array of four bytes (X, Y, Z, reserved) to enable (1) or disable individual magnetic torquers.
245 - 247	vec3f	coil_offset	Offset for coil control moments.
...	...	...	...
261	float	Kalman_frequency	Defines how often attitude estimation is performed.
262	uint8	use_coil_correction	Enable (1) or disable (0) coil correction matrix.
263 - 271	vec9f	inertia_matrix_inv	Inverse inertia matrix.
272 - 280	vec9f	inertia_matrix	Inertia matrix.
281 - 283	vec3f	inertia	Diagonal values of the inertia matrix.
...	...	...	...
500 - 511	vec12f	P_v	Kalman filter covariance parameters.
512 - 523	vec12f	Q_v	Kalman filter model noise covariance parameters.
524 - 532	vec9f	R_v	Kalman filter measurement noise covariance parameters.
533	float	bdot_gain	B-Dot gain.
534	float	bdot_cutoff_freq	B-Dot filter cutoff frequency, in Hz.
535	float	p_gain	Proportional pointing gain.
536	float	p_bdot_dnom	Nominal B-dot gain.
537	float	p_bdot_dmin	Minimal B-dot gain.
538	float	p_max_perr	Max pointing error for B-dot gain reduction.
539	float	p_bdot_n	B-dot filter coefficient.
540	float	spin_z_k	Spin-Z controller gain for overall convergence.
541	float	spin_z_k_1	Spin-Z controller gain for precession damping.
542	float	spin_z_k_2	Spin-Z controller gain for nutation damping.
543	float	omega_d_z_scal	Spin-Z desired angular rate around Z axis, in rad/s.
544 - 546	vec3f	satSpinAxis_S	Spin-Arb desired sat rotation axis in sat frame.
547 - 549	vec3f	alignAxis_I	Spin-Arb Earth axis to align with.
550	float	spin_realignment_gain	Spin-Arb controller gain for realignment.
551	float	spin_spinup_gain	Spin-Arb controller gain for spinup.
552	float	spin_precession_gain	Spin-Arb controller gain for precession effects.
553	float	spin_target_speed	Spin-Arb desired angular rate, in rad/s.
...	...	...	...

Table 1: ADCS configuration table.

Addresses	**Type**	**Name**	**Description**
555	float	`Kalman_ frequency_ spin_z`	Attitude estimation frequency during z-axis spin-up.
...	...	...	...

Appendix E
License

Non-exclusive license to reproduce thesis and make thesis public

I, Indrek Sünter,

1. herewith grant the University of Tartu a free permit (non-exclusive licence) to:
   reproduce, for the purpose of preservation, including for adding to the DSpace digital archives until the expiry of the term of copyright,

   Design and characterisation of subsystems and software for ESTCube-1 nanosatellite,

   supervised by Prof. Mart Noorma.

2. I grant the University of Tartu a permit to make the work specified in p. 1 available to the public via the web environment of the University of Tartu, including via the DSpace digital archives, under the Creative Commons licence CC BY NC ND 3.0, which allows, by giving appropriate credit to the author, to reproduce, distribute the work and communicate it to the public, and prohibits the creation of derivative works and any commercial use of the work until the expiry of the term of copyright.

3. I am aware of the fact that the author retains the rights specified in p. 1 and 2.

4. I certify that granting the non-exclusive licence does not infringe other persons' intellectual property rights or rights arising from the personal data protection legislation.

Indrek Sünter
21/06/2019

Publications

Curriculum vitae

Personal data

Name	Indrek Sünter
Date and place of birth	November 16, 1988, Tartu, Estonia
Citizenship	Estonian
Address	Kaunase str. 44-12, 50706 Tartu Tartumaa, Estonia
Phone	(+372) 56161367
E-mail	indrek.sunter@ut.ee

Education

2015 – 2019	University of Tartu, Ph.D. student, Physics
2012 – 2014	University of Tartu, M.Sc., Computer Engineering *cum laude*
2008 – 2011	University of Tartu, B.Sc., Physics

Professional career

2018 – present	KappaZeta Ltd., Estonia
2016 – present	Tartu Observatory, University of Tartu (Junior Research Fellow)
2014 – 2015	Tartu Observatory (Engineer)

Professional training

12 – 21 July, 2016	Alpbach Summer School: "Satellite observations of the global water cycle", Alpbach / Tyrol, Austria
1 – 12 September, 2014	ESEO Student Workshop, Bertinoro, Italy

Conference presentations

11 – 13 April, 2018	Conference "2nd Symposium on Space Educational Activities", Budapest, Hungary. *Oral presentation*: "Optical Characterisation of the ESEO Optical Payload"
26 – 30 Sept., 2016	Conference "67th International Astronautical Congress", Guadalajara, Mexico. *Oral presentation*: "Design and Testing of a Dual-Camera Payload for ESEO"
30 May – 3 June, 2016	Conference "Small Satellites, Systems & Services Symposium (4S)", Valletta, Malta. *Oral presentation*: "Dual-camera payload for ESEO"
19 – 21 August, 2015	Conference "Baltic Applied Astroinformatics and Space data Processing", Ventspils, Latvia. *Oral presentation*: "In-orbit firmware updates for nanosatellite platforms"
13 April, 2014	Seminar "XXI DevClub.lv", Riga, Latvia. *Oral presentation*: "ESTCube-1 firmware upgrades and testing"
17 November, 2013	Seminar "ASA Quality Assurance", Tallinn, Estonia. *Oral presentation*: "Quality assurance in ESTCube-1 firmware development"
19 – 21 July, 2013	Conference "AMSAT-UK Colloquium", Guildford, UK. *Oral presentation*: "ESTCube-1"

Awards and scholarships

2018	Archimedes Foundation KOMEET scholarship to attend the 2nd Symposium on Space Educational Acitivities
2017	Charles Villmann scholarship (Tartu Observatory)
2016	Harry Rowe Minmo award certificate for co-authoring the August 2015 IEEE AESS Magazine Article "ESTCube-1 In-Orbit Experience and Lessons Learned"
2016	Archimedes Foundation Kristjan Jaak scholarship to attend Small Satellites, Systems & Services Symposium
2016	Archimedes Foundation KOMEET scholarship to attend Alpbach Summer School
2016	Archimedes Foundation Dora Plus scholarship to attend the 67th IAC
2016 – 2019	University of Tartu, Institute of Physics Ph.D. student scholarship
2013 – 2014	University of Tartu, Institute of Technology M.Sc. student scholarship
2009 – 2011	University of Tartu, Institute of Physics B.Sc. student scholarship

Publications

1. I. Iakubivskyi, P. Janhunen, J. Praks, V. Allik, K. Bussov, B. Clayhills, ... **I. Sünter** *et al.*, "Coulomb Drag Propulsion experiments of ESTCube-2 and FORESAIL-1," in *Tethers in Space Proceedings*, May 2019, submitted.

2. **I. Sünter**, H. Kuuste, and J. Kütt, "Optical characterisation of the ESEO optical payload," in *Proc. 2nd Symposium on Space Educational Activities*, L. Bacsardi and K. Kovacs, Eds., vol. 2. Budapest University of Technology and Economics, Apr. 2018, pp. 123–126.

3. A. Slavinskis, P. Janhunen, P. Toivanen, K. Muinonen, A. Penttilä, M. Granvik, ... **I. Sünter** *et al.*, "Nanospacecraft fleet for multi-asteroid touring with electric solar wind sails," in *2018 IEEE Aerospace Conference*. IEEE, Mar. 2018, pp. 1–20. [Online]. Available: https://doi.org/10.1109/AERO.2018.8396670

4. I. Iakubivskyi, H. Ehrpais, H. Kuuste, **I. Sünter**, E. Ilbis, M.-L. Aru, E. Oro *et al.*, "ESTCube-2 plasma brake payload for effective deorbiting," in *Proc. 7th European Conference on Space Debris*, Apr. 2017, Debris Mitigation: Design Solutions.

5. H. Ehrpais, J. Kütt, **I. Sünter**, E. Kulu, A. Slavinskis, and M. Noorma, "Nanosatellite spin-up using magnetic actuators: ESTCube-1 flight results," *Acta Astronaut.*, vol. 128, pp. 210–216, Nov. 2016. [Online]. Available: https://doi.org/10.1016/j.actaastro.2016.07.032

6. I. Iakubivskyi, H. Ehrpais, J. Dalbins, E. Oro, E. Kulu, J. Kütt, ... **I. Sünter** *et al.*, "ESTCube-2 mission analysis: plasma brake experiment for deorbiting," in *Proc. International Astronautical Congress*. IAF, Sep. 2016, pp. 1–10, 45th Student Conference, IAC-16,E2,4,4,x33190.

7. **I. Sünter**, H. Kuuste, A. Slavinskis, A. Agu, E. Ilbis, G. Olentšenko, I. Iakubivskyi *et al.*, "Design and testing of a dual-camera payload for ESEO," in *Proc. International Astronautical Congress*. IAF, Sep. 2016, pp. 1–10, Small Earth Observation Missions, IAC–16–B4.4.3,x31978.

8. **I. Sünter**, H. Kuuste, J. Kütt, E. Ilbis, A. Agu, I. Iakubivskyi, S. Chopra *et al.*, "Dual-camera payload for ESEO," in *Proc. Small Satellites, Systems & Services Symposium (4S)*. ESA Publications Division, Jun. 2016, pp. 1–10, Academic Projects, S13-4-145.

9. H. Ehrpais, **I. Sünter**, E. Ilbis, J. Dalbins, I. Iakubivskyi, E. Kulu, I. Ploom *et al.*, "ESTCube-2 mission and satellite design," in *Proc. Small Satellites, Systems & Services Symposium (4S)*. ESA Publications Division, Jun. 2016, pp. 1–7, Mission Analysis, CS03-3-305.

10. **I. Sünter**, A. Slavinskis, U. Kvell, A. Vahter, H. Kuuste, M. Noorma, J. Kütt *et al.*, "Firmware updating systems for nanosatellites," *IEEE Aerosp. Electron. Syst. Mag.*, vol. 31, no. 5, pp. 36–44, May 2016. [Online].
Available: https://doi.org/10.1109/MAES.2016.150162

11. A. Slavinskis, H. Ehrpais, H. Kuuste, **I. Sünter**, J. Viru, E. Kulu, J. Kütt *et al.*, "Flight results of ESTCube-1 attitude determination system," *J. Aerosp. Eng.*, vol. 29, no. 1, p. 04015014:1-7, Apr. 2015. [Online]. Available: https://doi.org/10.1061/(ASCE)AS.1943-5525.0000504

12. A. Slavinskis, M. Pajusalu, H. Kuuste, E. Ilbis, T. Eenmäe, **I. Sünter**, K. Laizāns *et al.*, "ESTCube-1 in-orbit experience and lessons learned," *IEEE Aerosp. Electron. Syst. Mag.*, vol. 30, no. 8, pp. 12–22, Oct. 2015. [Online].
Available: https://doi.org/10.1109/MAES.2015.150034

13. S. Lätt, A. Slavinskis, E. Ilbis, U. Kvell, K. Voormansik, E. Kulu, ... **I. Sünter** *et al.*, "ESTCube nanosatellite for electric solar wind sail in-orbit technology demonstration," *Proc. Estonian Acad. Sci.*, vol. 63(2S), pp. 200–209, May 2014. [Online].
Available: https://doi.org/10.3176/proc.2014.2S.01

14. K. Laizāns, **I. Sünter**, K. Zālīte, H. Kuuste, M. Valgur, K. Tarbe, V. Allik *et al.*, "The design of fault tolerant command and data handling subsystem for ESTCube-1," *Proc. Estonian Acad. Sci.*, vol. 63(2S), pp. 222–231, May 2014. [Online].
Available: https://doi.org/10.3176/proc.2014.2S.03

15. H. Kuuste, T. Eenmäe, V. Allik, A. Agu, R. Vendt, I. Ansko, ... **I. Sünter** *et al.*, "Imaging system for nanosatellite proximity operations," *Proc. Estonian Acad. Sci.*, vol. 63(2S), pp. 250–257, May 2014. [Online].
Available: https://doi.org/10.3176/proc.2014.2S.06

16. A. Slavinskis, E. Kulu, J. Viru, R. Valner, H. Ehrpais, T. Uiboupin, ... **I. Sünter** *et al.*, "Attitude determination and control for centrifugal tether deployment on ESTCube-1 nanosatellite," *Proc. Estonian Acad. Sci.*, vol. 63(2S), pp. 242–249, May 2014. [Online].
Available: https://doi.org/10.3176/proc.2014.2S.05

17. A. Slavinskis, U. Kvell, E. Kulu, **I. Sünter**, H. Kuuste, S. Lätt, K. Voormansik *et al.*, "High spin rate magnetic controller for nanosatellites," *Acta Astronaut.*, vol. 95, pp. 218–226, Feb. 2014. [Online].
Available: https://doi.org/10.1016/j.actaastro.2013.11.014

Supervised theses

2019	Rain Eric Haamer, M.Sc. in computer engineering "Imaging Simulator and Geometric Image Stitching for a Low Earth Orbit Satellite with High Spin Rates," co-supervisor: Gholamreza Anbarjafari
2019	Miroslav Rolko, M.Sc. in computer engineering "Development and performance analysis of the Network Time Protocol Server," co-supervisor: Viljo Allik
2019	Aksel Allas, B.Sc. in physics "3D CNN for pixel-wise classification of crops using satellite imagery," co-supervisor: Kaupo Voormansik
2018	Ervin Oro, B.Sc. in informatics "Delta Updates for ESTCube-2 Onboard Computer Software," co-supervisor: Helle Hein
2017	Hannes Haljaste, M.Sc. in computer engineering "Electronics design and testing for ESTCube-2 on-board computer system with sensors for attitude determination," co-supervisor: Viljo Allik
2016	Aivar Lobjakas, B.Sc. in informatics "Hardware-in-the-loop testing module for Mission Control System," co-supervisors: Kaarel Hanson, Mare Koit
2016	Laur Joost, B.Sc. in physics "Demodulation of BPSK using Software Defined Radio," co-supervisor: Viljo Allik
2016	Miroslav Rolko, B.Sc. in computer engineering "Universal antenna rotator controller for satellite ground stations," co-supervisor: Viljo Allik
2015	Sander Tammesoo, B.Sc. in computer engineering "Internal Communication Protocol for ESTCube-2 subsystems," co-supervisor: Mart Noorma

Teaching

2018/2019 spring	"LTTO.00.005 Space Systems (6 EAP)" responsible lecturer
2017/2018 spring	"LOTI.05.077 Space Systems (6 EAP)" responsible lecturer
2016/2017 spring	"LOTI.05.077 Space Systems (6 EAP)" responsible lecturer

Elulookirjeldus

Isikuandmed

Nimi	Indrek Sünter
Sünniaeg ja -koht	November 16, 1988, Tartu, Eesti
Kodakondsus	Eesti
Address	Kaunase pst. 44-12, 50706 Tartu Tartumaa, Eesti
Telefon	(+372) 56161367
E-post	indrek.sunter@ut.ee

Haridus

2015 – 2019	Tartu Ülikool, doktorant, füüsika eriala
2012 – 2014	Tartu Ülikool, M.Sc., arvutitehnika eriala
2008 – 2011	Tartu Ülikool, B.Sc., füüsika eriala

Teenistuskäik

2018 – ...	KappaZeta OÜ, Eesti
2016 – ...	Tartu Observatoorium, Tartu Ülikool (nooremteadur)
2014 – 2015	Tartu Observatoorium (insener)

Täiendkoolitus

12 – 21 July, 2016	Alpbach suvekool: "Satellite observations of the global water cycle", Alpbach / Tyrol, Austria
1 – 12 September, 2014	ESEO tudengite koolitus, Bertinoro, Italy

Konverentside ettekanded

11.04 – 13.04 2018	Konverents "2nd Symposium on Space Educational Activities", Budapest, Hungary. *Suuline ettekanne*: "Optical Characterisation of the ESEO Optical Payload"
26.09 – 30.09 2016	Konverents "67th International Astronautical Congress", Guadalajara, Mexico. *Suuline ettekanne*: "Design and Testing of a Dual-Camera Payload for ESEO"
30.05 – 03.06 2016	Konverents "Small Satellites, Systems & Services Symposium (4S)", Valletta, Malta. *Suuline ettekanne*: "Dual-camera payload for ESEO"
19.08 – 21.08 2015	Konverents "Baltic Applied Astroinformatics and Space data Processing", Ventspils, Latvia. *Suuline ettekanne*: "In-orbit firmware updates for nanosatellite platforms"
13.04 2014	Seminar "XXI DevClub.lv", Riga, Latvia. *Suuline ettekanne*: "ESTCube-1 firmware upgrades and testing"
17.11 2013	Seminar "ASA Quality Assurance", Tallinn, Estonia. *Suuline ettekanne*: "Quality assurance in ESTCube-1 firmware development"
19 – 21 July, 2013	Conference "AMSAT-UK Colloquium", Guildford, UK. *Suuline ettekanne*: "ESTCube-1"

Uurimistoetused ja stipendiumid

2018	SA Archimedes KOMEET stipendium konverentsil 2nd Symposium on Space Educational Acitivities osalemiseks
2017	Charles Villmanni nimeline stipendium (Tartu Observatoorium)
2016	Harry Rowe Minmo auhinna sertifikaat artikli "ESTCube-1 In-Orbit Experience and Lessons Learned" kaasautorluse eest IEEE AESS Magazine 2015 augustikuu väljaandes
2016	SA Archimedes Kristjan Jaak stipendium konverentsil Small Satellites, Systems & Services Symposium osalemiseks
2016	SA Archimedes KOMEET stipendium Alpbach suvekoolil osalemiseks
2016	SA Archimedes Dora Pluss stipendium konverentsil 67th International Astronautical Congress osalemiseks
2016 – 2019	Tartu Ülikool, Füüsika Instituut Ph.D. tudengistipendium
2013 – 2014	Tartu Ülikool, Tehnoloogiainstituut M.Sc. tudengistipendium
2009 – 2011	Tartu Ülikool, Füüsika Instituut B.Sc. tudengistipendium

Publikatsioonid

1. I. Iakubivskyi, P. Janhunen, J. Praks, V. Allik, K. Bussov, B. Clayhills, ... **I. Sünter** *et al.*, "Coulomb Drag Propulsion experiments of ESTCube-2 and FORESAIL-1," in *Tethers in Space Proceedings*, May 2019, submitted.

2. **I. Sünter**, H. Kuuste, and J. Kütt, "Optical characterisation of the ESEO optical payload," in *Proc. 2nd Symposium on Space Educational Activities*, L. Bacsardi and K. Kovacs, Eds., vol. 2. Budapest University of Technology and Economics, Apr. 2018, pp. 123–126.

3. A. Slavinskis, P. Janhunen, P. Toivanen, K. Muinonen, A. Penttilä, M. Granvik, ... **I. Sünter** *et al.*, "Nanospacecraft fleet for multi-asteroid touring with electric solar wind sails," in *2018 IEEE Aerospace Conference*. IEEE, Mar. 2018, pp. 1–20. [Online].
Available: https://doi.org/10.1109/AERO.2018.8396670

4. I. Iakubivskyi, H. Ehrpais, H. Kuuste, **I. Sünter**, E. Ilbis, M.-L. Aru, E. Oro *et al.*, "ESTCube-2 plasma brake payload for effective deorbiting," in *Proc. 7th European Conference on Space Debris*, Apr. 2017, Debris Mitigation: Design Solutions.

5. H. Ehrpais, J. Kütt, **I. Sünter**, E. Kulu, A. Slavinskis, and M. Noorma, "Nanosatellite spin-up using magnetic actuators: ESTCube-1 flight results," *Acta Astronaut.*, vol. 128, pp. 210–216, Nov. 2016. [Online]. Available: https://doi.org/10.1016/j.actaastro.2016.07.032

6. I. Iakubivskyi, H. Ehrpais, J. Dalbins, E. Oro, E. Kulu, J. Kütt, ... **I. Sünter** *et al.*, "ESTCube-2 mission analysis: plasma brake experiment for deorbiting," in *Proc. International Astronautical Congress*. IAF, Sep. 2016, pp. 1–10, 45th Student Conference, IAC-16,E2,4,4,x33190.

7. **I. Sünter**, H. Kuuste, A. Slavinskis, A. Agu, E. Ilbis, G. Olentšenko, I. Iakubivskyi *et al.*, "Design and testing of a dual-camera payload for ESEO," in *Proc. International Astronautical Congress*. IAF, Sep. 2016, pp. 1–10, Small Earth Observation Missions, IAC–16–B4.4.3,x31978.

8. **I. Sünter**, H. Kuuste, J. Kütt, E. Ilbis, A. Agu, I. Iakubivskyi, S. Chopra *et al.*, "Dual-camera payload for ESEO," in *Proc. Small Satellites, Systems & Services Symposium (4S)*. ESA Publications Division, Jun. 2016, pp. 1–10, Academic Projects, S13-4-145.

9. H. Ehrpais, **I. Sünter**, E. Ilbis, J. Dalbins, I. Iakubivskyi, E. Kulu, I. Ploom *et al.*, "ESTCube-2 mission and satellite design," in *Proc. Small Satellites, Systems & Services Symposium (4S)*. ESA Publications Division, Jun. 2016, pp. 1–7, Mission Analysis, CS03-3-305.

10. **I. Sünter**, A. Slavinskis, U. Kvell, A. Vahter, H. Kuuste, M. Noorma, J. Kütt *et al.*, "Firmware updating systems for nanosatellites," *IEEE Aerosp. Electron. Syst. Mag.*, vol. 31, no. 5, pp. 36–44, May 2016. [Online].
Available: https://doi.org/10.1109/MAES.2016.150162

11. A. Slavinskis, H. Ehrpais, H. Kuuste, **I. Sünter**, J. Viru, E. Kulu, J. Kütt *et al.*, "Flight results of ESTCube-1 attitude determination system," *J. Aerosp. Eng.*, vol. 29, no. 1, p. 04015014:1-7, Apr. 2015. [Online].
Available: https://doi.org/10.1061/(ASCE)AS.1943-5525.0000504

12. A. Slavinskis, M. Pajusalu, H. Kuuste, E. Ilbis, T. Eenmäe, **I. Sünter**, K. Laizāns *et al.*, "ESTCube-1 in-orbit experience and lessons learned," *IEEE Aerosp. Electron. Syst. Mag.*, vol. 30, no. 8, pp. 12–22, Oct. 2015. [Online].
Available: https://doi.org/10.1109/MAES.2015.150034

13. S. Lätt, A. Slavinskis, E. Ilbis, U. Kvell, K. Voormansik, E. Kulu, ... **I. Sünter** *et al.*, "ESTCube nanosatellite for electric solar wind sail in-orbit technology demonstration," *Proc. Estonian Acad. Sci.*, vol. 63(2S), pp. 200–209, May 2014. [Online].
Available: https://doi.org/10.3176/proc.2014.2S.01

14. K. Laizāns, **I. Sünter**, K. Zālīte, H. Kuuste, M. Valgur, K. Tarbe, V. Allik *et al.*, "The design of fault tolerant command and data handling subsystem for ESTCube-1," *Proc. Estonian Acad. Sci.*, vol. 63(2S), pp. 222–231, May 2014. [Online].
Available: https://doi.org/10.3176/proc.2014.2S.03

15. H. Kuuste, T. Eenmäe, V. Allik, A. Agu, R. Vendt, I. Ansko, ... **I. Sünter** *et al.*, "Imaging system for nanosatellite proximity operations," *Proc. Estonian Acad. Sci.*, vol. 63(2S), pp. 250–257, May 2014. [Online].
Available: https://doi.org/10.3176/proc.2014.2S.06

16. A. Slavinskis, E. Kulu, J. Viru, R. Valner, H. Ehrpais, T. Uiboupin, ... **I. Sünter** *et al.*, "Attitude determination and control for centrifugal tether deployment on ESTCube-1 nanosatellite," *Proc. Estonian Acad. Sci.*, vol. 63(2S), pp. 242–249, May 2014. [Online].
Available: https://doi.org/10.3176/proc.2014.2S.05

17. A. Slavinskis, U. Kvell, E. Kulu, **I. Sünter**, H. Kuuste, S. Lätt, K. Voormansik *et al.*, "High spin rate magnetic controller for nanosatellites," *Acta Astronaut.*, vol. 95, pp. 218–226, Feb. 2014. [Online].
Available: https://doi.org/10.1016/j.actaastro.2013.11.014

Juhendatud lõputööd

2019	Rain Eric Haamer, arvutitehnika magistritöö "Pildistamise simulaator ja geomeetriline pilditöötlus maa-lähedase orbiidi ja suure pöördesagedusega satelliidil" (kaasjuhendaja Gholamreza Anbarjafari)
2019	Miroslav Rolko, arvutitehnika magistritöö "Võrguaja protokolli serveri arenduse ja toimivuse analüüs" (kaasjuhendaja Viljo Allik)
2019	Aksel Allas, füüsika bakalaureusetöö "Satelliidipiltidelt põllukultuuride pikselhaaval klassifitseerimine 3D sidumnärvivõrguga" (kaasjuhendaja Kaupo Voormansik)
2018	Ervin Oro, informaatika bakalaureusetöö "Delta uuendused ESTCube-2 pardaarvuti tarkvarale" (kaasjuhendaja Helle Hein)
2017	Hannes Haljaste, arvutitehnika bakalaureusetöö "Elektroonika projekteerimine ja testimine ESTCube-2 pardaarvutile koos asendi määramise sensoritega" (kaasjuhendaja Viljo Allik)
2016	Aivar Lobjakas, informaatika bakalaureusetöö "Riistvara testimismoodul missioonijuhtimissüsteemile" (kaasjuhendajad Kaarel Hanson, Mare Koit)
2016	Laur Joost, füüsika bakalaureusetöö "BPSK demoduleerimine tarkvaralise raadioga" (kaasjuhendaja Viljo Allik)
2016	Miroslav Rolko, arvutitehnika bakalaureusetöö "Universaalne pööraja kontroller satelliidi jaamade jaoks" (kaasjuhendaja Viljo Allik)
2015	Sander Tammesoo, arvutitehnika bakalaureusetöö "Suhtlusprotokoll ESTCube-2 alamsüsteemide vaheliseks suhtluseks" (kaasjuhendaja Mart Noorma)

Õpetamine

2018/2019 kevad	"LTTO.00.005 Kosmosesüsteemid (6 EAP)" vastutav õppejõud
2017/2018 kevad	"LOTI.05.077 Kosmosesüsteemid (6 EAP)" vastutav õppejõud
2016/2017 kevad	"LOTI.05.077 Kosmosesüsteemid (6 EAP)" vastutav õppejõud

DISSERTATIONES PHYSICAE UNIVERSITATIS TARTUENSIS

1. **Andrus Ausmees.** XUV-induced electron emission and electron-phonon interaction in alkali halides. Tartu, 1991.
2. **Heiki Sõnajalg.** Shaping and recalling of light pulses by optical elements based on spectral hole burning. Tartu, 1991.
3. **Sergei Savihhin.** Ultrafast dynamics of F-centers and bound excitons from picosecond spectroscopy data. Tartu, 1991.
4. **Ergo Nõmmiste.** Leelishalogeniidide röntgenelektronemissioon kiiritamisel footonitega energiaga 70–140 eV. Tartu, 1991.
5. **Margus Rätsep.** Spectral gratings and their relaxation in some low-temperature impurity-doped glasses and crystals. Tartu, 1991.
6. **Tõnu Pullerits.** Primary energy transfer in photosynthesis. Model calculations. Tartu, 1991.
7. **Olev Saks.** Attoampri diapasoonis voolude mõõtmise füüsikalised alused. Tartu, 1991.
8. **Andres Virro.** AlGaAsSb/GaSb heterostructure injection lasers. Tartu, 1991.
9. **Hans Korge.** Investigation of negative point discharge in pure nitrogen at atmospheric pressure. Tartu, 1992.
10. **Jüri Maksimov.** Nonlinear generation of laser VUV radiation for high-resolution spectroscopy. Tartu, 1992.
11. **Mark Aizengendler.** Photostimulated transformation of aggregate defects and spectral hole burning in a neutron-irradiated sapphire. Tartu, 1992.
12. **Hele Siimon.** Atomic layer molecular beam epitaxy of A^2B^6 compounds described on the basis of kinetic equations model. Tartu, 1992.
13. **Tõnu Reinot.** The kinetics of polariton luminescence, energy transfer and relaxation in anthracene. Tartu, 1992.
14. **Toomas Rõõm.** Paramagnetic H^{2-} and F^+ centers in CaO crystals: spectra, relaxation and recombination luminescence. Tallinn, 1993.
15. **Erko Jalviste.** Laser spectroscopy of some jet-cooled organic molecules. Tartu, 1993.
16. **Alvo Aabloo.** Studies of crystalline celluloses using potential energy calculations. Tartu, 1994.
17. **Peeter Paris.** Initiation of corona pulses. Tartu, 1994.
18. **Павел Рубин.** Локальные дефектные состояния в CuO_2 плоскостях высокотемпературных сверхпроводников. Тарту, 1994.
19. **Olavi Ollikainen.** Applications of persistent spectral hole burning in ultrafast optical neural networks, time-resolved spectroscopy and holographic interferometry. Tartu, 1996.
20. **Ülo Mets.** Methodological aspects of fluorescence correlation spectroscopy. Tartu, 1996.
21. **Mikhail Danilkin.** Interaction of intrinsic and impurity defects in CaS:Eu luminophors. Tartu, 1997.

22. **Ирина Кудрявцева.** Создание и стабилизация дефектов в кристаллах KBr, KCl, RbCl при облучении ВУФ-радиацией. Тарту, 1997.
23. **Andres Osvet.** Photochromic properties of radiation-induced defects in diamond. Tartu, 1998.
24. **Jüri Örd.** Classical and quantum aspects of geodesic multiplication. Tartu, 1998.
25. **Priit Sarv.** High resolution solid-state NMR studies of zeolites. Tartu, 1998.
26. **Сергей Долгов.** Электронные возбуждения и дефектообразование в некоторых оксидах металлов. Тарту, 1998.
27. **Kaupo Kukli.** Atomic layer deposition of artificially structured dielectric materials. Tartu, 1999.
28. **Ivo Heinmaa.** Nuclear resonance studies of local structure in $RBa_2Cu_3O_{6+x}$ compounds. Tartu, 1999.
29. **Aleksander Shelkan.** Hole states in CuO_2 planes of high temperature superconducting materials. Tartu, 1999.
30. **Dmitri Nevedrov.** Nonlinear effects in quantum lattices. Tartu, 1999.
31. **Rein Ruus.** Collapse of 3d (4f) orbitals in 2p (3d) excited configurations and its effect on the x-ray and electron spectra. Tartu, 1999.
32. **Valter Zazubovich.** Local relaxation in incommensurate and glassy solids studied by Spectral Hole Burning. Tartu, 1999.
33. **Indrek Reimand.** Picosecond dynamics of optical excitations in GaAs and other excitonic systems. Tartu, 2000.
34. **Vladimir Babin.** Spectroscopy of exciton states in some halide macro- and nanocrystals. Tartu, 2001.
35. **Toomas Plank.** Positive corona at combined DC and AC voltage. Tartu, 2001.
36. **Kristjan Leiger.** Pressure-induced effects in inhomogeneous spectra of doped solids. Tartu, 2002.
37. **Helle Kaasik.** Nonperturbative theory of multiphonon vibrational relaxation and nonradiative transitions. Tartu, 2002.
38. **Tõnu Laas.** Propagation of waves in curved spacetimes. Tartu, 2002.
39. **Rünno Lõhmus.** Application of novel hybrid methods in SPM studies of nanostructural materials. Tartu, 2002.
40. **Kaido Reivelt.** Optical implementation of propagation-invariant pulsed free-space wave fields. Tartu, 2003.
41. **Heiki Kasemägi.** The effect of nanoparticle additives on lithium-ion mobility in a polymer electrolyte. Tartu, 2003.
42. **Villu Repän.** Low current mode of negative corona. Tartu, 2004.
43. **Алексей Котлов.** Оксианионные диэлектрические кристаллы: зонная структура и электронные возбуждения. Tartu, 2004.
44. **Jaak Talts.** Continuous non-invasive blood pressure measurement: comparative and methodological studies of the differential servo-oscillometric method. Tartu, 2004.
45. **Margus Saal.** Studies of pre-big bang and braneworld cosmology. Tartu, 2004.

46. **Eduard Gerškevitš.** Dose to bone marrow and leukaemia risk in external beam radiotherapy of prostate cancer. Tartu, 2005.
47. **Sergey Shchemelyov.** Sum-frequency generation and multiphoton ionization in xenon under excitation by conical laser beams. Tartu, 2006.
48. **Valter Kiisk.** Optical investigation of metal-oxide thin films. Tartu, 2006.
49. **Jaan Aarik.** Atomic layer deposition of titanium, zirconium and hafnium dioxides: growth mechanisms and properties of thin films. Tartu, 2007.
50. **Astrid Rekker.** Colored-noise-controlled anomalous transport and phase transitions in complex systems. Tartu, 2007.
51. **Andres Punning.** Electromechanical characterization of ionic polymer-metal composite sensing actuators. Tartu, 2007.
52. **Indrek Jõgi.** Conduction mechanisms in thin atomic layer deposited films containing TiO_2. Tartu, 2007.
53. **Aleksei Krasnikov.** Luminescence and defects creation processes in lead tungstate crystals. Tartu, 2007.
54. **Küllike Rägo.** Superconducting properties of MgB_2 in a scenario with intra- and interband pairing channels. Tartu, 2008.
55. **Els Heinsalu.** Normal and anomalously slow diffusion under external fields. Tartu, 2008.
56. **Kuno Kooser.** Soft x-ray induced radiative and nonradiative core-hole decay processes in thin films and solids. Tartu, 2008.
57. **Vadim Boltrushko.** Theory of vibronic transitions with strong nonlinear vibronic interaction in solids. Tartu, 2008.
58. **Andi Hektor.** Neutrino Physics beyond the Standard Model. Tartu, 2008.
59. **Raavo Josepson.** Photoinduced field-assisted electron emission into gases. Tartu, 2008.
60. **Martti Pärs.** Study of spontaneous and photoinduced processes in molecular solids using high-resolution optical spectroscopy. Tartu, 2008.
61. **Kristjan Kannike.** Implications of neutrino masses. Tartu, 2008.
62. **Vigen Issahhanjan.** Hole and interstitial centres in radiation-resistant MgO single crystals. Tartu, 2008.
63. **Veera Krasnenko.** Computational modeling of fluorescent proteins. Tartu, 2008.
64. **Mait Müntel.** Detection of doubly charged higgs boson in the CMS detector. Tartu, 2008.
65. **Kalle Kepler.** Optimisation of patient doses and image quality in diagnostic radiology. Tartu, 2009.
66. **Jüri Raud.** Study of negative glow and positive column regions of capillary HF discharge. Tartu, 2009.
67. **Sven Lange.** Spectroscopic and phase-stabilisation properties of pure and rare-earth ions activated ZrO_2 and HfO_2. Tartu, 2010.
68. **Aarne Kasikov.** Optical characterization of inhomogeneous thin films. Tartu, 2010.
69. **Heli Valtna-Lukner.** Superluminally propagating localized optical pulses. Tartu, 2010.

70. **Artjom Vargunin.** Stochastic and deterministic features of ordering in the systems with a phase transition. Tartu, 2010.
71. **Hannes Liivat.** Probing new physics in e+e− annihilations into heavy particles via spin orientation effects. Tartu, 2010.
72. **Tanel Mullari.** On the second order relativistic deviation equation and its applications. Tartu, 2010.
73. **Aleksandr Lissovski.** Pulsed high-pressure discharge in argon: spectroscopic diagnostics, modeling and development. Tartu, 2010.
74. **Aile Tamm.** Atomic layer deposition of high-permittivity insulators from cyclopentadienyl-based precursors. Tartu, 2010.
75. **Janek Uin.** Electrical separation for generating standard aerosols in a wide particle size range. Tartu, 2011.
76. **Svetlana Ganina.** Hajusandmetega ülesanded kui üks võimalus füüsikaõppe efektiivsuse tõstmiseks. Tartu, 2011
77. **Joel Kuusk.** Measurement of top-of-canopy spectral reflectance of forests for developing vegetation radiative transfer models. Tartu, 2011.
78. **Raul Rammula**. Atomic layer deposition of HfO_2 – nucleation, growth and structure development of thin films. Tartu, 2011.
79. **Сергей Наконечный.** Исследование электронно-дырочных и интерстициал-вакансионных процессов в монокристаллах MgO и LiF методами термоактивационной спектроскопии. Тарту, 2011.
80. **Niina Voropajeva.** Elementary excitations near the boundary of a strongly correlated crystal. Tartu, 2011.
81. **Martin Timusk.** Development and characterization of hybrid electro-optical materials. Tartu, 2012, 106 p.
82. **Merle Lust.** Assessment of dose components to Estonian population. Tartu, 2012, 84 p.
83. **Karl Kruusamäe.** Deformation-dependent electrode impedance of ionic electromechanically active polymers. Tartu, 2012, 128 p.
84. **Liis Rebane.** Measurement of the $W \to \tau\nu$ cross section and a search for a doubly charged Higgs boson decaying to τ-leptons with the CMS detector. Tartu, 2012, 156 p.
85. **Jevgeni Šablonin.** Processes of structural defect creation in pure and doped MgO and NaCl single crystals under condition of low or super high density of electronic excitations. Tartu, 2013, 145 p.
86. **Riho Vendt**. Combined method for establishment and dissemination of the international temperature scale. Tartu, 2013, 108 p.
87. **Peeter Piksarv.** Spatiotemporal characterization of diffractive and non-diffractive light pulses. Tartu, 2013, 156 p.
88. **Anna Šugai.** Creation of structural defects under superhigh-dense irradiation of wide-gap metal oxides. Tartu, 2013, 108 p.
89. **Ivar Kuusik.** Soft X-ray spectroscopy of insulators. Tartu, 2013, 113 p.
90. **Viktor Vabson**. Measurement uncertainty in Estonian Standard Laboratory for Mass. Tartu, 2013, 134 p.

91. **Kaupo Voormansik.** X-band synthetic aperture radar applications for environmental monitoring. Tartu, 2014, 117 p.
92. **Deivid Pugal.** hp-FEM model of IPMC deformation. Tartu, 2014, 143 p.
93. **Siim Pikker.** Modification in the emission and spectral shape of photostable fluorophores by nanometallic structures. Tartu, 2014, 98 p.
94. **Mihkel Pajusalu**. Localized Photosynthetic Excitons. Tartu, 2014, 183 p.
95. **Taavi Vaikjärv.** Consideration of non-adiabaticity of the Pseudo-Jahn-Teller effect: contribution of phonons. Tartu, 2014, 129 p.
96. **Martin Vilbaste.** Uncertainty sources and analysis methods in realizing SI units of air humidity in Estonia. Tartu, 2014, 111 p.
97. **Mihkel Rähn.** Experimental nanophotonics: single-photon sources- and nanofiber-related studies. Tartu, 2015, 107 p.
98. **Raul Laasner.** Excited state dynamics under high excitation densities in tungstates. Tartu, 2015, 125 p.
99. **Andris Slavinskis.** EST Cube-1 attitude determination. Tartu, 2015, 104 p.
100. **Karlis Zalite**. Radar Remote Sensing for Monitoring Forest Floods and Agricultural Grasslands. Tartu, 2016, 124 p.
101. **Kaarel Piip.** Development of LIBS for *in-situ* study of ITER relevant materials. Tartu, 2016, 93 p.
102. **Kadri Isakar.** ^{210}Pb in Estonian air: long term study of activity concentrations and origin of radioactive lead. Tartu, 2016, 107 p.
103. **Artur Tamm.** High entropy alloys: study of structural properties and irradiation response. Tartu, 2016, 115 p.
104. **Rasmus Talviste.** Atmospheric-pressure He plasma jet: effect of dielectric tube diameter. Tartu, 2016, 107 p.
105. **Andres Tiko.** Measurement of single top quark properties with the CMS detector. Tartu, 2016, 161 p.
106. **Aire Olesk.** Hemiboreal Forest Mapping with Interferometric Synthetic Aperture Radar. Tartu, 2016, 121 p.
107. **Fred Valk.** Nitrogen emission spectrum as a measure of electric field strength in low-temperature gas discharges. Tartu, 2016, 149 p.
108. **Manoop Chenchiliyan.** Nano-structural Constraints for the Picosecond Excitation Energy Migration and Trapping in Photosynthetic Membranes of Bacteria. Tartu, 2016, 115p.
109. **Lauri Kaldamäe.** Fermion mass and spin polarisation effects in top quark pair production and the decay of the higgs boson. Tartu, 2017, 104 p.
110. **Marek Oja.** Investigation of nano-size α- and transition alumina by means of VUV and cathodoluminescence spectroscopy. Tartu, 2017, 89 p.
111. **Viktoriia Levushkina.** Energy transfer processes in the solid solutions of complex oxides. Tartu, 2017, 101 p.
112. **Mikk Antsov.** Tribomechanical properties of individual 1D nanostructures: experimental measurements supported by finite element method simulations. Tartu, 2017, 101 p.
113. **Hardi Veermäe.** Dark matter with long range vector-mediated interactions. Tartu, 2017, 137 p.

114. **Aris Auzans.** Development of computational model for nuclear energy systems analysis: natural resources optimisation and radiological impact minimization. Tartu, 2018, 138 p.
115. **Aleksandr Gurev**. Coherent fluctuating nephelometry application in laboratory practice. Tartu, 2018, 150 p.
116. **Ardi Loot**. Enhanced spontaneous parametric downconversion in plasmonic and dielectric structures. Tartu, 2018, 164 p.
117. **Andreas Valdmann.** Generation and characterization of accelerating light pulses. Tartu, 2019, 85 p.
118. **Mikk Vahtrus.** Structure-dependent mechanical properties of individual one-dimensional metal-oxide nanostructures. Tartu, 2019, 110 p.
119. **Ott Vilson.** Transformation properties and invariants in scalar-tensor theories of gravity. Tartu, 2019, 183 p.